

# **Patterning of Tethered Bilayer Lipid Membranes**

Dissertation zur Erlangung des Grades  
“Doktor der Naturwissenschaften”  
im Promotionsfach Chemie

am Fachbereich Chemie, Pharmazie und Geowissenschaften  
der Johannes Gutenberg – Universität Mainz

Mathieu Jung  
Geboren in Straßburg, Frankreich

Mainz, 2008



“One does not discover new lands without consenting to lose sight of the shore for a very long time.”

André Gide



# Table of contents

<b>1. Introduction .....</b>	<b>1</b>
1.1. Construction and function of biomembranes .....	1
1.2. Model membranes .....	3
1.3. Patterning of bilayers .....	5
1.4. Topochemical reactions.....	6
1.4.1. Definition .....	6
1.4.2. The concept of “reaction cavity” .....	7
1.5. Aim of this work: .....	8
<b>2. Materials &amp; Methods .....</b>	<b>10</b>
2.1. Nuclear Magnetic Resonance (NMR) .....	10
2.2. Mass spectrometry.....	11
2.3. Differential scanning calorimetry.....	11
2.4. Langmuir – Blodgett films .....	12
2.4.1. Isotherms .....	12
2.4.2. Film deposition.....	16
2.5. Membrane Preparation .....	17
2.5.1. Template stripped gold (TSG).....	18
2.5.2. Cleaning of oxide surfaces .....	19
2.5.3. Monolayer formation by self-assembly.....	19
2.5.4. Bilayer formation by vesicle fusion .....	20
2.5.5. Bilayer formation by rapid solvent exchange method.....	21
2.6. Water contact angle (WCA) .....	22
2.7. Ultraviolet-Visible Spectroscopy (UV-Vis).....	23
2.8. Electrical Impedance Spectroscopy (EIS).....	24
2.8.1. Physical basis: definition of impedance .....	24
2.8.2. Measurement setup.....	26

2.8.3.	Evaluation of the impedance data .....	27
2.9.	Optical waveguide spectroscopy .....	28
2.10.	Fluorescence recovery after photobleaching (FRAP) .....	29
2.10.1.	Measurement procedure and evaluation.....	30
2.10.2.	Theory of diffusion.....	32
<b>3.</b>	<b>Ultra flat heterogeneously structured substrates .....</b>	<b>34</b>
3.1.	Photolithographic Structuring .....	34
3.1.1.	Concept.....	34
3.1.2.	Photolithography .....	35
3.1.3.	Success and limits of the method .....	36
3.2.	Direct evaporation through a mask .....	39
3.2.1.	Protection of the TSGs with monolayers .....	39
3.2.2.	Direct evaporation .....	40
3.2.3.	Selective functionalization of the substrates .....	43
<b>4.</b>	<b>Synthesis.....</b>	<b>46</b>
4.1.	General remarks .....	46
4.2.	Ether linked molecules .....	47
4.2.1.	General procedure .....	47
4.2.2.	Synthesis of the spacer part .....	53
4.2.3.	Discussion of the synthesis way .....	54
4.3.	Ester linked molecules .....	57
4.3.1.	Double stranded anchor lipids.....	57
4.3.2.	Single stranded anchor lipids .....	62
<b>5.</b>	<b>Thermotropic behavior of polymerizable tBLM.....</b>	<b>66</b>
5.1.	DSC experiments.....	66
5.2.	Optical waveguide spectroscopy .....	68
<b>6.</b>	<b>Langmuir films .....</b>	<b>70</b>
6.1.	TD2(EO) <sub>4</sub> LA and TD2(EO) <sub>4</sub> TES .....	71
6.2.	HC1(EO) <sub>4</sub> LA and HC1(EO) <sub>4</sub> TES .....	73

6.3.	HC <sub>2</sub> (EO) <sub>4</sub> LA and HC <sub>2</sub> (EO) <sub>4</sub> TES .....	74
<b>7.</b>	<b>UV-Visible spectroscopy .....</b>	<b>76</b>
7.1.	HC <sub>2</sub> (EO) <sub>4</sub> TES on quartz .....	76
7.2.	HC <sub>2</sub> (EO) <sub>4</sub> LA on quartz.....	78
<b>8.</b>	<b>Photolithographic patterning.....</b>	<b>81</b>
8.1.	HC <sub>2</sub> (EO) <sub>4</sub> TES on quartz.....	81
8.2.	HC <sub>2</sub> (EO) <sub>4</sub> LA on quartz.....	85
<b>9.</b>	<b>Electrical impedance spectroscopy .....</b>	<b>88</b>
9.1.	Valinomycin .....	88
9.2.	Building the bilayer .....	89
9.3.	Introduction of Valinomycin in the tBLM .....	90
9.4.	Polymerization of the bilayer .....	92
<b>10.</b>	<b>Fluorescence recovery after photobleaching .....</b>	<b>94</b>
10.1.	Sample preparation.....	95
10.2.	Bilayer formation .....	97
10.3.	FRAP measurements .....	98
10.3.1.	Lipid diffusion in both leaflets .....	98
10.3.2.	Lipid diffusion in the bottom leaflet .....	100
<b>11.</b>	<b>Conclusions and outlook.....</b>	<b>101</b>
<b>12.</b>	<b>Appendix .....</b>	<b>105</b>
12.1.	<sup>1</sup> H-NMR and FD-Mass spectra of the synthesized anchor lipids:.....	105
<b>13.</b>	<b>Literature .....</b>	<b>111</b>
<b>14.</b>	<b>Publications.....</b>	<b>115</b>
<b>15.</b>	<b>Curriculum Vitae .....</b>	<b>116</b>

## Abbreviations

AFM	Atomic force microscopy
Au	Gold
BK7	Borosilicate glass slide
BLM	Bilayer lipid membrane <i>or</i> black lipid membrane
Cr	Chromium
D	Diffusion coefficient
DC <sub>23</sub> PC	1,2-bis(10,12-tricosadiynoyl)-sn-glycero-3-phosphocholine
DCC	N,N'-dicyclohexylcarbodiimide
DCM	Dichloromethane
DMAP	4-Dimethylaminopyridine
DOPE-NBD	1,2-dioleoyl-sn-glycero-3-phosphoethanolamine-N-(7-nitro-2-1,3-benzoxadiazol-4-yl)
DPhyPC	1,2-diphytanoyl-sn-glycero-3-phosphocholine
DSC	Differential scanning calorimetry
EDX	Energy dispersive X-ray spectroscopy
EIS	Electrical impedance spectroscopy
FRAP	Fluorescence recovery after photobleaching
HC1(EO) <sub>4</sub> LA	<i>Heptacosa-10,12-diynoic acid-tetraethylene glycol ester-(D,L-α lipoic acid ester)</i>
HC1(EO) <sub>4</sub> TES	<i>Heptacosa-10,12-diynoic acid-tetraethylene glycol ester-[3-(triethoxysilyl) propylcarbamate]</i>
HC2(EO) <sub>4</sub> LA	<i>Succinic acid-2-(thioglycolic acid-[tetraethylene glycol ester-[D,L-α lipoic acid ester]])-1,4-bis(heptacosa-10,12-diynyl)-ester</i>
HC2(EO) <sub>4</sub> TES	<i>Succinic acid-2-(thioglycolic acid-[tetraethylene glycol ester-[3-(triethoxysilyl) propylcarbamate]])-1,4-bis(heptacosa-10,12-diynyl)-ester</i>
HEPES	4-(2-hydroxyethyl)-1-piperazineethanesulfonic acid
LB	Langmuir – Blodgett
LC	Liquid condensed
LE	Liquid expanded
MMA	Mean molecular area
NMP	N-methylpyrrolidone
NMR	Nuclear magnetic resonance

OTE	n-octadecyltriethoxysilane
OWS	Optical waveguide spectroscopy
ppm	Parts per million
PTFE	Polytetrafluoroethylene
PVD	Physical vapor deposition
QCM	Quartz crystal microbalance
SAM	Self-assembled monolayer
SEM	Scanning electron microscopy
SiO <sub>x</sub>	Silicon oxide
SP	Surface pressure
SPR	Surface plasmon resonance
SSM	Solid supported membranes
tBLM	Tethered bilayer lipid membrane
TD2(EO) <sub>4</sub> LA	<i>1,3-bis(tricosa-10,12-diynyoxy)-glycerol-2-(tetraethylene glycol-[D,L-<math>\alpha</math>-lipoic acid ester])</i>
TD2(EO) <sub>4</sub> TES	<i>1,3-bis(tricosa-10,12-diynyoxy)-glycerol-2-(tetraethylene glycol-[3-(triethoxysilyl) propylcarbamate])</i>
TE	Transverse electric
TEM	Transmission electron microscopy
THP	3,4-dihydro-2H-pyran
TiO <sub>x</sub>	Titanium oxide
TLC	Thin layer chromatography
TM	Transverse magnetic
Tris	2-Amino-2-hydroxymethyl-propane-1,3-diol
TSG	Template stripped gold
UV	Ultraviolet
UV-Vis	Ultraviolet visible



## **Acknowledgements**



# 1. Introduction

## 1.1. Construction and function of biomembranes

Cells are the structural and functional units of all known living organisms. These “building-blocks” of life are self-contained and self-maintaining: they can take up nutriments or expel waste, carry out metabolic reactions and reproduce themselves. A cell membrane confines these complex entities from the external environment, preserving their internal integrity. In addition to the delimitation of the cell as a whole from the extracellular environment, it also maintains the characteristic differences between the content of each organelle (e.g. mitochondria, lysosomes, Golgi apparatus) within the cytoplasm. Furthermore, the membranes are hosting various types of proteins, which are involved in many fundamental processes, e.g. establishing ion gradients over the membrane or acting as sensors to external signals.

Despite the great variety of cells, and functions they exert, the general structure of the membrane remains. They are formed by a thin film of lipids and proteins retaining their organization via non-covalent interactions. *Singer* and *Nicolson*<sup>[1]</sup> proposed a fluid mosaic model of the membrane structure, applicable to most biological membranes, such as plasma membranes and intracellular membranes (see Figure 1.1). The non-covalent interactions between the lipids constituting the matrix of the membrane imply a certain degree of translational and rotational freedom of the lipids and the proteins in the bilayer. *Frye* and *Edidin*<sup>[2]</sup> suggested that the intermixing of membrane components was due to diffusion of components within the membrane.

“The fluid mosaic structure is therefore formally analogous to a two-dimensional oriented solution of integral proteins in the viscous phospholipid bilayer solvent.”<sup>[1]</sup>

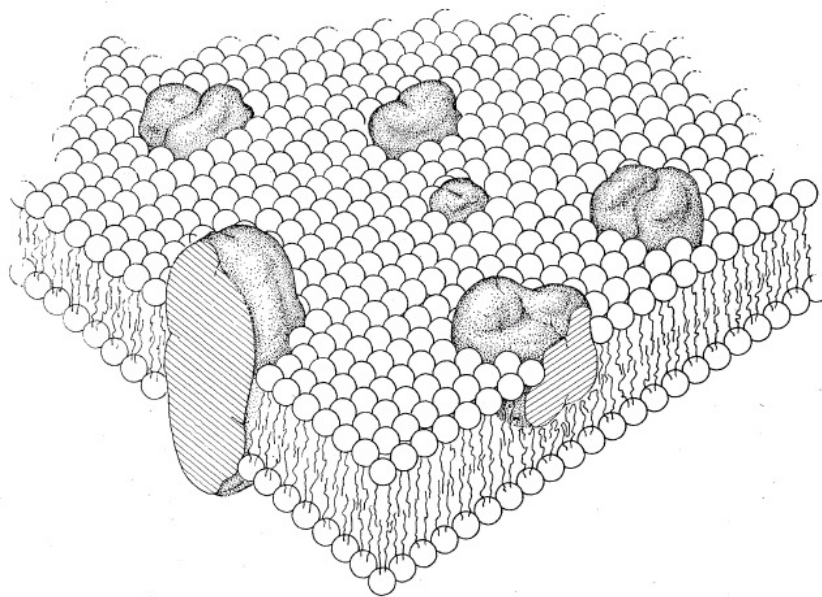


**Figure 1.1:** “The lipid-globular protein mosaic model with a lipid matrix (the fluid mosaic model); schematic three-dimensional and cross-sectional views. The solid bodies with stippled surfaces represent the globular integral proteins, which at long range are randomly distributed in the plane of the membrane.”<sup>[1]</sup>

A protein-free lipid bilayer remains impermeable to most hydrophilic molecules, allowing the formation of gradients over it (see Figure 1.2). Especially high resistance against ion intrusion is shown, independently to their size. This is mainly due to the charge and the solvation shell around them, preventing their entry in the hydrophobic core of the membrane.

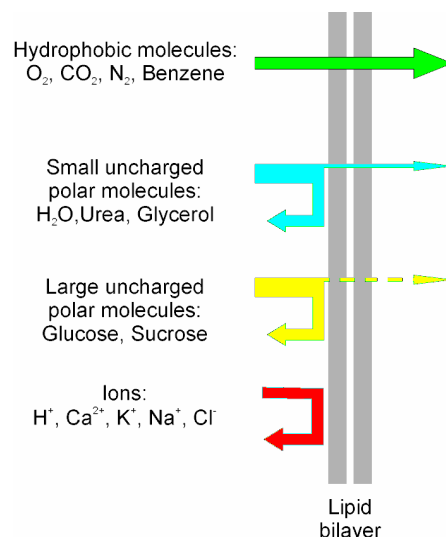


**Figure 1.2:** Relative permeability of a lipid bilayer to different classes of molecules.<sup>[3]</sup>

The controlled transfer of ions or waste across the membrane has therefore to be mediated. Special membrane proteins are responsible for the transfer of particular classes of molecules. They mainly belong to two major groups: carrier proteins and channel proteins. Carrier proteins bind selectively the solute to be transported and over a series of conformational changes release it on the opposite side of the membrane. Channel proteins, in contrary, create a hydrophilic pore across the membrane, hence allowing the transport of the species by diffusion. In addition to these primary regulatory functions, other types of proteins are responsible for the major part of the metabolisms occurring in the cell or at its periphery, including recognition of other cells, signaling, and catalytic processes.

During the last decades, this high selectivity and organization of cell membranes has been attracting increasing scientific interests, especially as an inspiration for the design of biosensor platforms. Unfortunately, biological membranes are composed by hundreds of different components. Due to this complexity, their direct use for sensing purposes is limited.<sup>[4, 5]</sup> Simplified approaches had to be developed in order to obtain selective and reproducible responses to defined stimuli. For this purpose, various types of model membranes have been developed.

## 1.2. Model membranes

Membrane processes can be reconstituted and studied in different types of model membranes. These models, similar to the natural membranes consist of amphiphilic molecules which are able to self-organize in contact with an aqueous medium. The main driving force for this self-organization is the hydrophobic effect, where the hydrophobic parts of the molecules tend avoid interactions with water.<sup>[6, 7]</sup> The amphiphiles used in the vast majority of the examples for the conception of model membranes are lipids or lipid based molecules, in analogy to their natural archetype.

Depending on the preparation process and the desired applications, different types of lipid assemblies can be constructed. In most cases, the structures either lack of accessibility for specific measurements or long term stability. These problems have been overcome by the developments of solid supported membranes (SSMs). First introduced by Sackmann,<sup>[8]</sup> they couple the fragile lipid membrane to a solid substrate and consist of a bilayer membrane

directly spread over a hydrophilic solid support. SSMs can be prepared, either by direct liposome fusion on the surface<sup>[9, 10]</sup> or by a combination of Langmuir film deposition techniques.<sup>[11]</sup> Beyond the mechanical stability introduced by the support, the planar bilayer can be characterized by various surface analytical tools since both sides of the membrane can be accessed. A major drawback of the SSMs is the proximity of the proximal leaflet to the substrate, only separated by a thin water layer (5-10 Å). As a consequence, the incorporation of transmembrane proteins is hindered due to the lack of submembrane spacing itself or to the denaturation of proteins coming in contact with the solid.

To enhance the applicability of such planar membrane systems to the study of embedded proteins, various systems were derived from the SSM approach, producing a decoupling of the bilayer from the substrate. A non exhaustive list of examples is depicted in Figure 1.3.

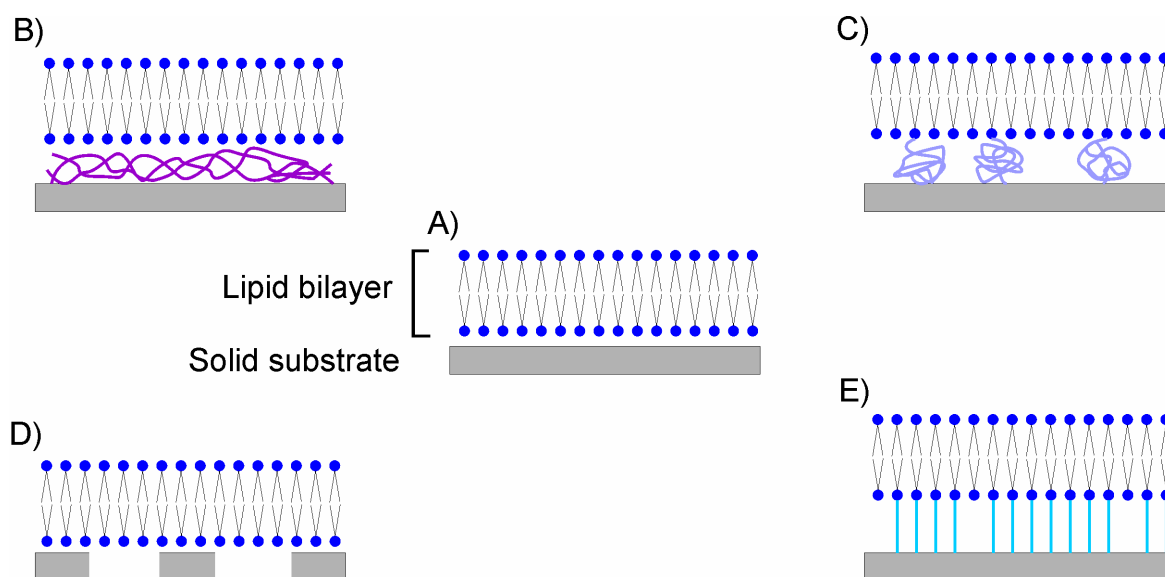


**Figure 1.3: Different types of SSMs; A) original system<sup>[8]</sup>, B) polymer cushioned bilayer<sup>[12, 13]</sup>, long polymer-lipid cushion<sup>[14, 15]</sup>, D) SSM over nanoporous substrates<sup>[16, 17]</sup>, E) tethered bilayer lipid membranes.<sup>[18-20]</sup>**

In this study, the approach of tethered bilayer lipid membranes (tBLMs) was favored. The proximal leaflet of this type of model membrane is covalently bound to the surface by anchor lipids. These lipids consist of hydrophobic chains being inserted in the bilayer, that are directly linked to a short hydrophilic spacer (tetraethylene glycol in our case) to create a submembrane ionic reservoir. The hydrophilic moiety terminates with a surface specific anchor group being responsible for the immobilization of the lipopolymer on the substrate. This system unifies the advantages of being very stable, addressable with different surface

sensitive methods and permitting the study of functionally incorporated proteins.<sup>[18, 20-23]</sup> The major drawback is the distribution of proteins over the complete substrate that prevents the simultaneous and individual addressing of different types of proteins, that is highly desirable for all sensor related applications.

### 1.3. Patterning of bilayers

The lateral fluidity of lipid membranes is essential for the activity of the embedded proteins. On the other hand, this intrinsic feature is responsible for the continuous mixing of all membrane constituents. The patterning of the membrane in compartments is therefore necessary for the creation of integrated devices with spatially separated and addressable fluid membrane patches with different chemical composition.

The selective polymerization of lipids was first introduced to enhance the long term stability of liposomes<sup>[24-28]</sup> or bilayer lipid membranes (BLMs).<sup>[29, 30]</sup> From these efforts, different classes of polymerizable lipids were synthesized, with the reactive unit based on acrylates or diacetylene groups and mainly located in the hydrophobic chains.<sup>[26, 27, 30-32]</sup> A few examples of polymerizable groups are shown in Figure 1.4.

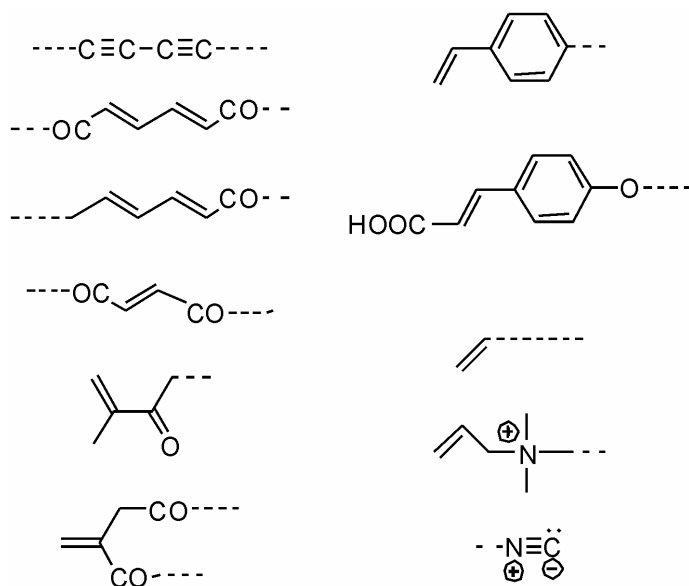


**Figure 1.4: Examples of possible polymerizable groups for lipids.**

Starting from these available monomeric lipids, recent studies demonstrated the possibility to pattern SSMs on quartz surfaces, produced by Langmuir film deposition techniques.<sup>[33, 34]</sup> Briefly, after bilayer formation on the substrate, a photolithographic mask was applied under water over the probe and the sample was UV irradiated. Thus, the structures in the mask could be reproduced in the bilayer as a polymerized film. Subsequently, non polymerized lipids were removed and replaced, demonstrating the versatility of the process. The major drawback of this method, as previously discussed, is the direct vicinity of the substrate below the membrane, posing problems for the incorporation of proteins.

Other ways to pattern the bilayer were followed by the structuring of the substrate<sup>[35, 36]</sup> or by microcontact printing of the bilayer.<sup>[37, 38]</sup> In both cases, the use of polymeric or inorganic barriers on the substrate is discussed. They permit the creation of membrane arrays confining the lipids and impeding their diffusion. As for the previous system, they suffer from the proximity of the substrate in the case of protein incorporation studies. Furthermore, the organization of the lipids at the barriers is not known and could be a source of leakage current if the system would be investigated on its electrical properties.

## 1.4. Topochemical reactions

In the following study, the cross-linking of lipids was done via diacetylene groups. Since diacetylenes do polymerize in a topochemical manner, a brief introduction is presented here.

### 1.4.1. Definition

The term topochemistry is derived from the greek word “topos” meaning “place”. It was introduced by *Cohen* and *Schmidt*,<sup>[39]</sup> and describes chemical reactions in predefined structures. The kinetic of reactions in isotropic media, where the reactants are free to diffuse, is essentially influenced by the electronic and steric effects due to the molecular structures. In contrast, topochemical reactions are taking place in a defined lattice system, where the diffusion is greatly reduced, if not suppressed. The correct disposition of the molecules before start of the reaction is thus crucial. The structure of the monomer crystal determines if the reaction takes place or not and dictates the stereochemistry of the product. Optically active organic products can be selectively achieved if the preferred conformation of the molecule remains “frozen” in the crystal prior to the reaction.<sup>[40, 41]</sup>

In some cases, topochemistry permits the realization of reactions which are not possible in an isotropic media, as shown by the photoinitiated dimerization of trans-cinnamic acid.<sup>[42]</sup> Briefly, within the lifetime of the excited state, the probability for a molecule to find a reaction partner in an isotropic media is very low, hindering the formation of the product.

#### 1.4.2. The concept of “reaction cavity”

Cohen and Schmidt formulated the “principle of topochemistry” and stated that solid-state reactions only occur with minimal motion of the atoms or molecules.<sup>[39]</sup>

If polymerization takes place in a crystal, the reaction path is controlled by the lattice. During the formation of the reaction complex, until the transition state, the reactive center is in close contact to its crystalline environment. The reaction centers -molecules or part of them- occupy a certain volume (“reaction cavity”) in the starting crystal. This cavity is defined by the volume of the reactive groups in contact with the other reacting groups.<sup>[39]</sup> The reaction proceeds with a minimal deformation of the surface of the reaction cavity.

The matrix should also show some flexibility to accommodate the convergence of the reactive centers during the bond formation.<sup>[43]</sup> For diacetylene molecules, a rotation of each molecule is induced in a way that the interactions with rest of the lattice stay minimal (see Figure 1.5).

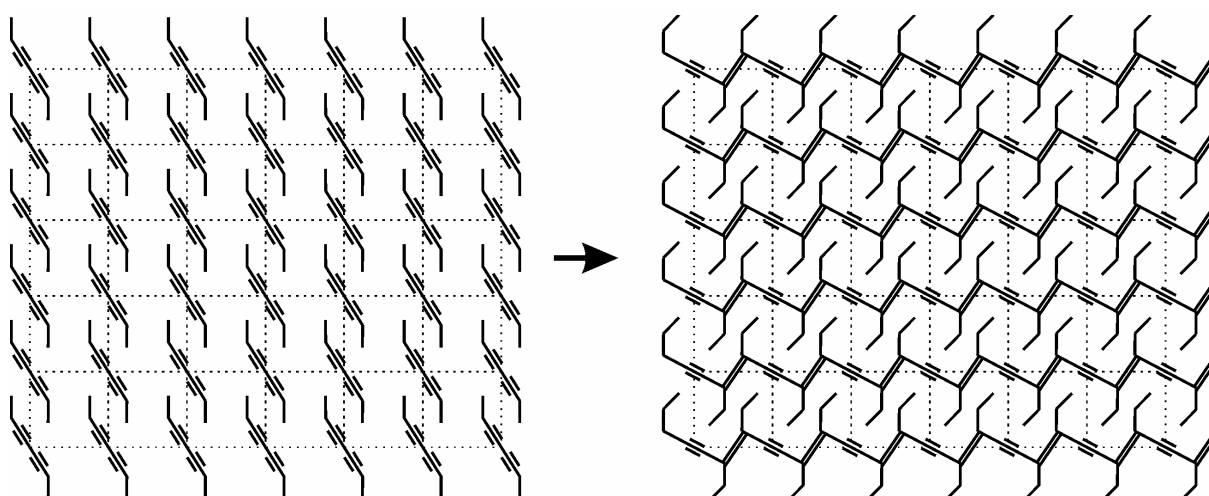


**Figure 1.5: Rearrangement of the diacetylene groups in the lattice upon polymerization.**

As already observed at the end of the 19<sup>th</sup> century, the polymerization of diacetylene molecules forms colored crystals.<sup>[44]</sup> The coloration is due to a repetition of triple and double bonds in the backbone of the formed polymer. The kinetic of the polymerization can easily be followed by an increase in absorption of the diacetylene crystals.

### 1.5. Aim of this work:

The molecular mechanisms of proteins involved in the regulation of the cell metabolism, as for example the creation of protein-complexes during the immunological response, are only partially clarified. Our current knowledge concerning the role of the different actors during the various processes still remains very scattered, despite all the technological progresses of the last decades. This remains so, even if it is assumed that the role and interplay of each constituent of the system is precisely defined, through molecular self-organization and molecular recognition. In this context, the creation of a cell mimicking environment represents a very promising approach for the study of the molecular interactions or the selective usage of naturally occurring mechanisms for sensing purposes.

Some artificial systems have already been conceived, producing protein-friendly environments. Based on tethered bilayer lipid membranes, established as stable and reliable model architecture for biosensing,<sup>[21, 45]</sup> the possibilities to pattern the membranes were investigated during this study. The ability to create membrane corrals would allow the separation of sensing proteins on an electrode array, and probing their response on the same analyte simultaneously.

As suggested by the scheme in Figure 1.6, the designed platform would allow the electrical detection of binding events at the sensing proteins, using separately addressable electrodes. Moreover, a polymerized bilayer surrounding the sensing areas would hinder the proteins to diffuse over the substrate.

Therefore, two questions had to be addressed during this project:

- the design of a structured substrate, meeting the requirements to accommodate a model membrane,
- the synthesis of selectively polymerizable tethered lipids for the formation of effective diffusion barriers.

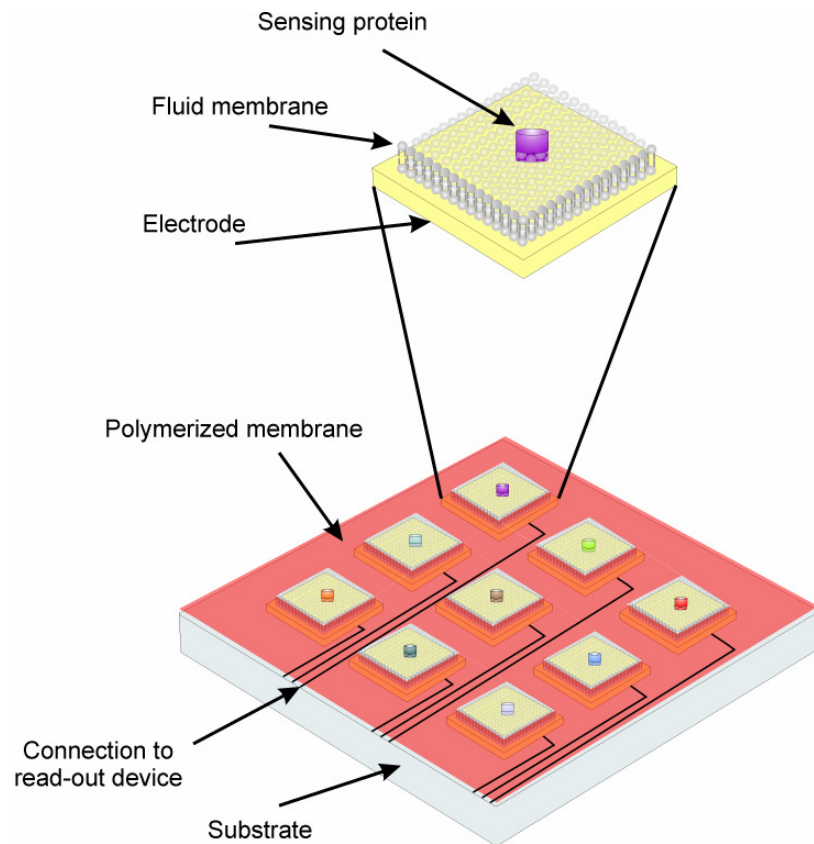


**Figure 1.6:** Schematic representation of a sensing platform.

## 2. Materials & Methods

### 2.1. Nuclear Magnetic Resonance (NMR)

NMR spectroscopy is the most powerful tool for the structural determination of organic compounds. Furthermore, it is a non destructive method and requires only small amounts of material.

This technique is only applicable to those nuclei which possess a spin quantum number ( $I$ ) greater than zero. The most important of such nuclei as far as the characterization of synthesized organic products is concerned are  $^1\text{H}$  and  $^{13}\text{C}$ , both of which have a spin quantum number of  $1/2$ . Other nuclei with non-zero spin quantum numbers are  $^{19}\text{F}$  and  $^{31}\text{P}$ , with  $I = 1/2$ ;  $^{14}\text{N}$  and  $^2\text{D}$ , with  $I = 1$ ,  $^{11}\text{B}$  and  $^{13}\text{Cl}$ , with  $I = 3/2$ , and many more.

Nuclei with non-zero spin quantum numbers can be imagined of as tiny spinning bar magnets. This spinning magnetic field creates a magnetic dipole, the magnitude of which is given by the nuclear magnetic moment  $\mu$ .

In the absence of an applied magnetic field the nuclei are randomly orientated. In a magnetic field they align in respectively to it. The number of orientations which the nucleus can adopt is limited by the spin quantum number and is equal to  $2I + 1$ . Thus, those nuclei with  $I = 1/2$  have two possible orientations in the magnetic field (+  $1/2$  and -  $1/2$ ). The two orientations are associated with different energy levels, orientation against the magnetic field being of higher energy and thus having a lower population. The difference in energy between the two spin states is dependent on the magnitude of the applied magnetic field and the nuclear magnetic moment. The frequency of radiation necessary to effect a transmission between the two energy levels is given by the equation:

$$\nu = \frac{\mu B_0}{hI} \quad (2.1)$$

where  $\nu$  is the frequency of radiation,  $\mu$  is the magnetic moment of the nucleus,  $B_0$  is the strength of the external magnetic field,  $h$  is Planck's constant, and  $I$  the spin quantum number. Thus, the larger the applied magnetic field, the greater the energy difference

between the two levels and the greater the frequency of radiation necessary to effect the transition between the two levels.

The basis of the NMR experiment is to subject the nuclei to radiation which results in a transition from the lower energy state to a higher one. The precise difference in energy levels between the two spin orientations is dependent on the particular location of the atom in the molecule, because each nucleus is subject to the differing effects of the magnetic fields of neighboring nuclei. In NMR spectroscopy these differences in energy are detected and provide information on the chemical environment of the nuclei in the molecule.

In this study, NMR spectra were measured on a Bruker Biospin 250 MHz spectrometer, using an automated software for the recording of the spectrum (Icon NMR 3.1.8). The processing of the spectra was done using MestReC software.

## 2.2. Mass spectrometry

Mass spectrometry is an analytical technique used for the determination of the molecular weight of organic compounds. In a typical mass spectrometer, an organic compound under high vacuum is bombarded with electrons. This induces the loss of one or more electrons from the molecule followed by various fission processes giving rise to ions and neutral fragments. The positive ions are expelled from the ionization chamber and resolved by means of a magnetic or an electrical field. The mass spectrum is a record of the current produced by these ions as they arrive at the detector. The resulting spectra is a plot of the abundance of each species again their mass-to-charge ratio.

The mass spectra presented in this work were performed on a VG ZAB2-SE-FPD spectrometer (Spectrofield). This type of spectrometer can resolve samples with masses in range of 250 – 3500 g/mol.

## 2.3. Differential scanning calorimetry

Differential scanning calorimetry (DSC) is a very well known and easy method to accurately obtain the thermal properties of materials. It measures the energy necessary to establish a nearly zero temperature difference between a substance and an inert reference

material, as the both substances are subjected to identical temperature regimes in an environment heated or cooled at a controlled rate.

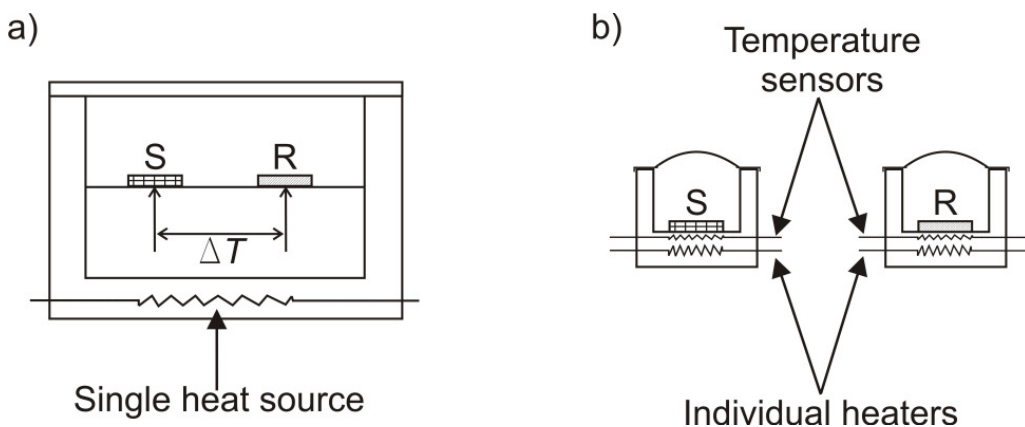


**Figure 2.1: a) Heat flux DSC, b) power compensation DSC**

Two types of systems are commonly used, the heat flux and power compensation DSC (see Figure 2.1). In the heat flux DSC the sample and the reference material are enclosed in the same furnace. The enthalpy or heat capacity changes are registered via a low heat resistance coupling below the samples, measuring temperature differences. In the power-compensation DSC, the temperatures in the sample and reference furnace are kept identical by varying the power input, directly in relation to the enthalpy or heat capacity differences between the sample and the reference.

With this method, we can precisely determine phase transitions or reactions occurring in the sample material. It is mostly used to measure melting or crystallization processes and glass transition temperature.

In this study, a heat flux DSC model 822 from Mettler Toledo (Greifensee, Swiss) was used.

## 2.4. Langmuir – Blodgett films

### 2.4.1. Isotherms

“Today (...) I plan to tell you about the behavior of molecules and atoms that are held at the surface of solids and liquids. The chemist has long described molecules that are held in this way on surfaces as adsorbed molecules. I will show you that we can have adsorbed films

which really constitute two-dimensional gases, two-dimensional liquids and two-dimensional solid."

– Irvin Langmuir, Science **1936**, 84, 379.

In the bulk of a liquid, molecules experience the same attractive forces in all direction (see Figure 2.2), whereas at the liquid/gas interface these forces cannot be compensated. As a result, a force applies to the molecules at the surface directed towards the bulk. The liquid tends therefore to reduce its surface and takes a spherical shape. The line force acting on the surface molecules is the surface tension  $\gamma$ .

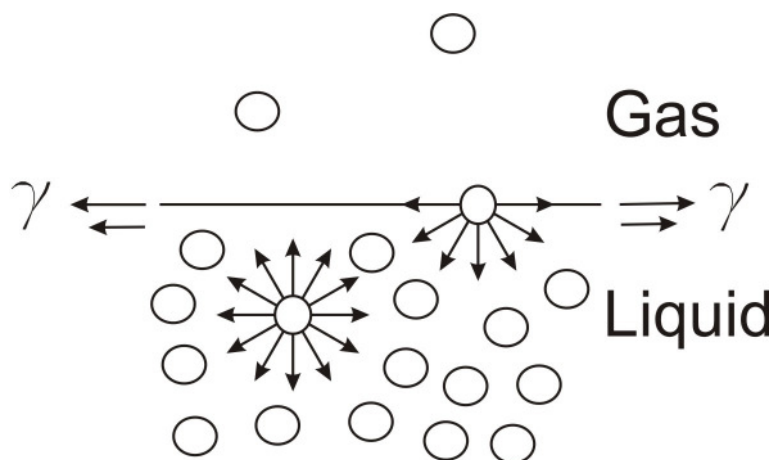


**Figure 2.2: Forces experienced by molecules in the bulk of a liquid and at the liquid/air interface.**

When applied at the air-water interface, amphiphilic molecules having both hydrophilic and hydrophobic part will spread and orient themselves on the surface in order to minimize their free energy. The resulting surface film is one molecule in thickness and is commonly called a monomolecular layer or a monolayer. When the area available for the monolayer is large, the distance between adjacent molecules are large and their interactions are weak. In this case, the monolayer can be regarded as a two-dimensional gas; it has little effect on the water surface tension. If the available surface area is reduced by a barrier system (see Figure 2.3), the molecules start to exert repulsive forces on each other. This two-dimensional analogue of a pressure is called surface pressure,  $\Pi$  and is equal to the reduction of the pure liquid surface tension by the film, i.e.:

$$\Pi = \gamma_0 - \gamma \quad (2.2)$$

where  $\gamma_0$  is the surface tension of the pure liquid and  $\gamma$  is the surface tension of the film covered surface. The surface pressure can be measured by the Wilhelmy plate-method. The forces resulting from the surface tension are measured on a partially immersed platinum plate. These forces are then converted into surface pressure (in [mN/m]) with the help of the plate dimensions.

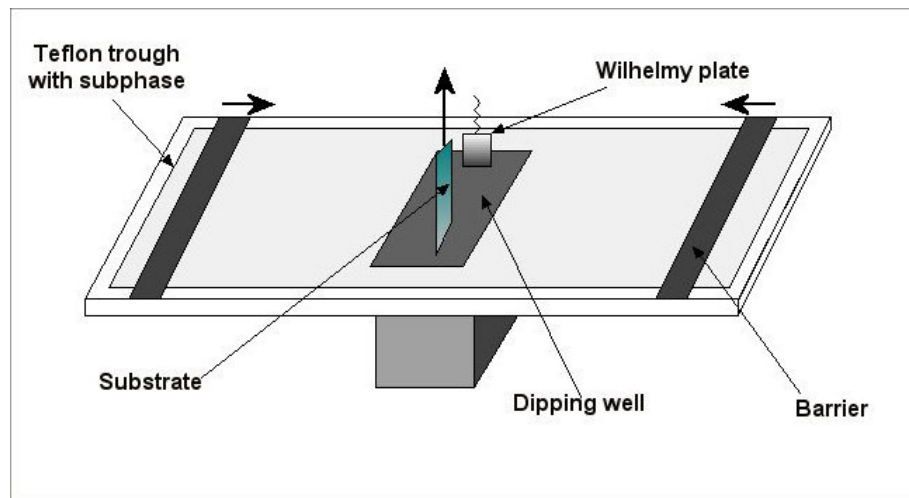


**Figure 2.3: Schematic drawing of a Langmuir – Blodgett – Kuhn film transfer apparatus.**

By spreading a defined amount of amphiphilic molecules on the air-water interface, it is possible to determine the mean molecular area ( $A$  in [ $\text{\AA}^2/\text{molecule}$ ]), i.e. the mean space occupied by each molecule. A surface pressure/area isotherm is measured by moving the barriers to compress the film and simultaneous recording of the change in the surface pressure.

The thermodynamic variable  $\Pi$  is the derivative of the surface free energy with respect to the intrinsic variable  $A$ . Therefore changes in the slope of the  $\Pi$ - $A$  isotherms at constant temperature can be used to identify and characterize phase transitions.<sup>[46, 47]</sup>

A typical isotherm for phospholipids is shown in Figure 2.4.

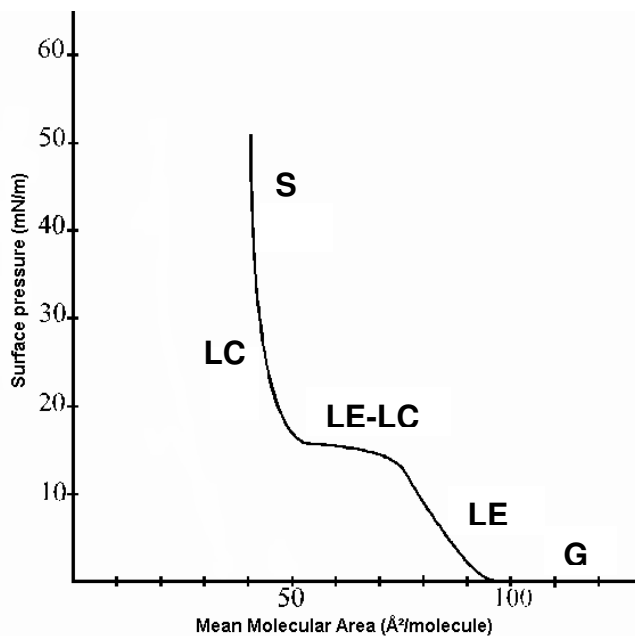


**Figure 2.4: Typical  $\Pi$ - $A$  isotherm of phospholipids.**

One can distinguish five different phases, characterized by a change in the slope of the isotherm.

- G: the gas phase, the interactions between the molecules are too weak to be noticed,
- LE: the liquid expanded state,
- LE-LC: transition plateau,
- LC: the liquid ordered state,
- S: the solid state.

After reaching the solid state, the monolayer attains a point where it can not be compressed any further and the pressure falls with decreasing area. This is referred to as collapse. When collapse occurs, molecules are forced out of the monolayer, as illustrated in Figure 2.5.<sup>[48]</sup>

Other collapsed structures are also possible for amphiphilic molecules. If they possess a highly polar head group with respect to the non-polar tails, micelles can be formed. In this case, the molecules are arranged in spheres, with the polar head groups on the outside and the hydrocarbon chains toward the centre. If the head group is not strong enough, spherical vesicles can form, in which the double layer shapes a shell with water both outside and inside.

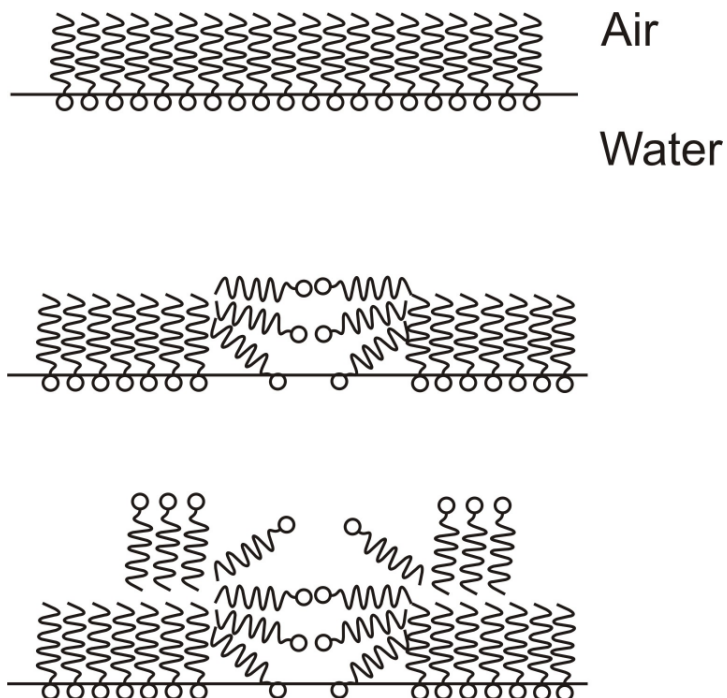


**Figure 2.5: Possible stages of a monolayer collapse, going from the top to the bottom diagram.**

#### 2.4.2. Film deposition

The Langmuir-Blodgett (LB) film deposition technique<sup>[49, 50]</sup> involves the vertical movement of a solid substrate through the monolayer/air interface. The surface pressure and the temperature of the film are controlled to first bring the monolayer in the desired phase followed by the transfer. The resulting molecular organization in the LB film will depend on these initial conditions.

In this study, the lipid monolayer will always be formed via a Y-type deposition if prepared with the LB method (see Figure 2.6), namely a hydrophilic substrate is pulled out of the water subphase entraining the compressed monolayer of lipopolymers.

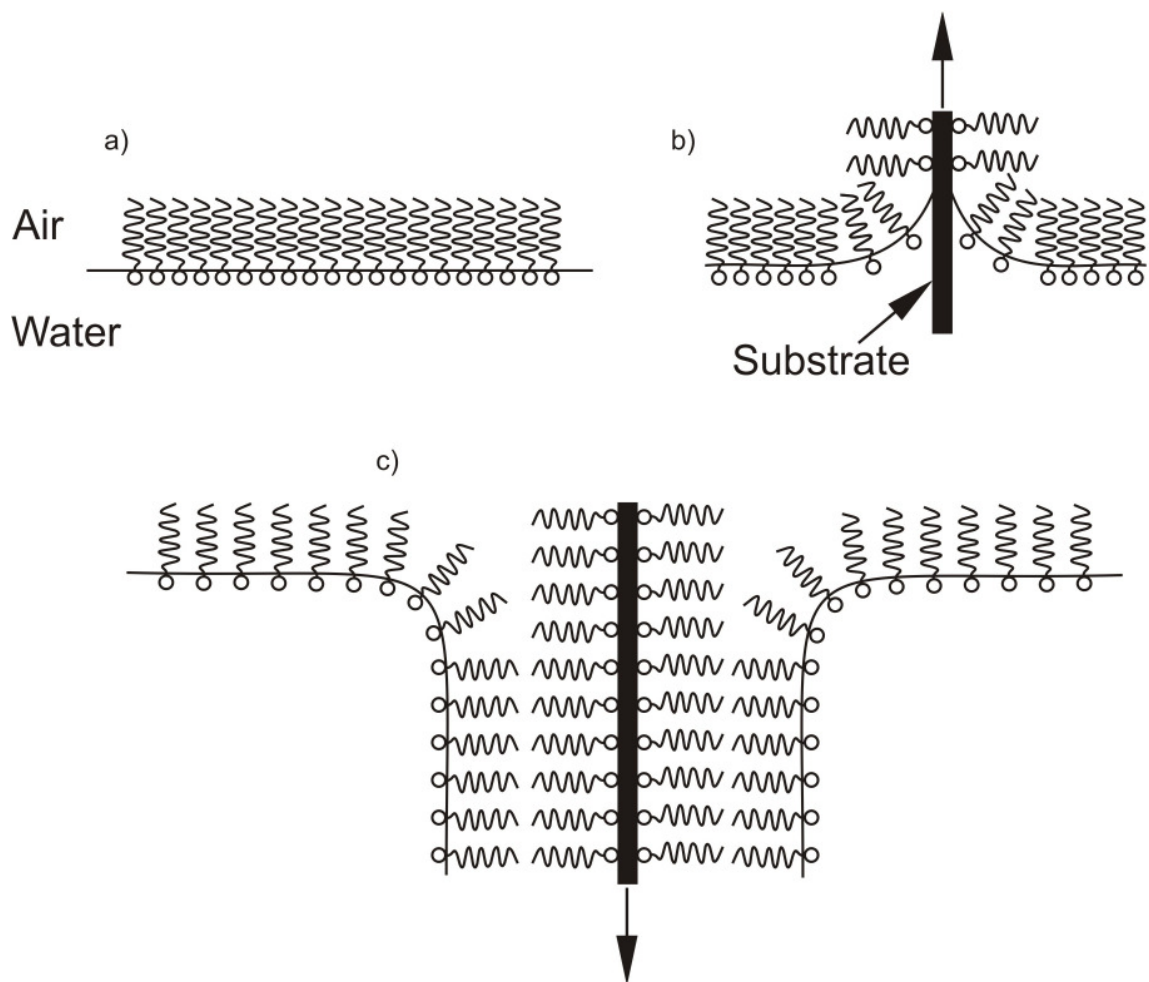


**Figure 2.6: Y-type Langmuir-Blodgett film deposition; a) monolayer before deposition, b) transfer of the first layer by pulling up the substrate, c) transfer of the second layer by pulling down the substrate.**

## 2.5. Membrane Preparation

The assembly of tBLMs on solid substrates involves different preparation steps, starting from the creation of an ultra-flat substrate, reducing the defects setting up during the membrane formation until the vesicle fusion on a monolayer, to achieve a complete bilayer. We present here the different cleaning and preparation routines used along this study.

### 2.5.1. Template stripped gold (TSG)

As described in the introductory part, the tBLMs are very thin films build up by amphiphilic molecules which cohesion rely on intermolecular forces, such as the hydrophobic effect and van der Waals forces. The very small length scale of the lipids and their interactions in the Z-direction, impose a very low surface roughness of the substrate in order to reduce the defects, as can be schematically seen in Figure 2.7.

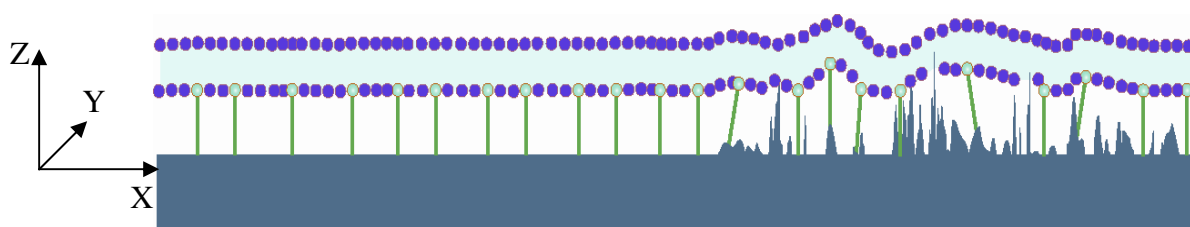


**Figure 2.7:** Schematic representation of the effect of surface roughness on tBLMs.

The most versatile substrate for solid supported membranes is gold, due to the possibility to apply a broad spectrum of surface analytical methods, e.g. electrical impedance spectroscopy (EIS), Surface Plasmon Resonance spectroscopy (SPR) or Quartz Crystal Microbalance (QCM), directly on the membrane. The following approach described by Hegner et al.<sup>[51]</sup> for creating ultra-flat surfaces relies on the fact that evaporated gold does not properly adhere to oxide surfaces and can be “stripped” down by gluing a support on the back. With this method, samples with root mean square roughness of approximately 0,3nm can be prepared.

Briefly, gold is evaporated by physical vapor deposition (PVD) (Edwards vacuum Ltd., UK) on freshly cleaved mica sheets or cleaned polished silicon wafers (Crystec, Germany). The fresh gold surface is glued (EPO-TEK 353ND4, Epoxy Technology, USA) to a glass slide (BK7, Menzel GmbH, Germany) and cured at 150°C for 60min. The mica or silicon wafer is mechanically stripped down, revealing a gold surface templating the mica or silicon wafer. Since the latter are atomically flat, very smooth gold surfaces can be obtained with this procedure. The procedure is summarized in Figure 2.8.

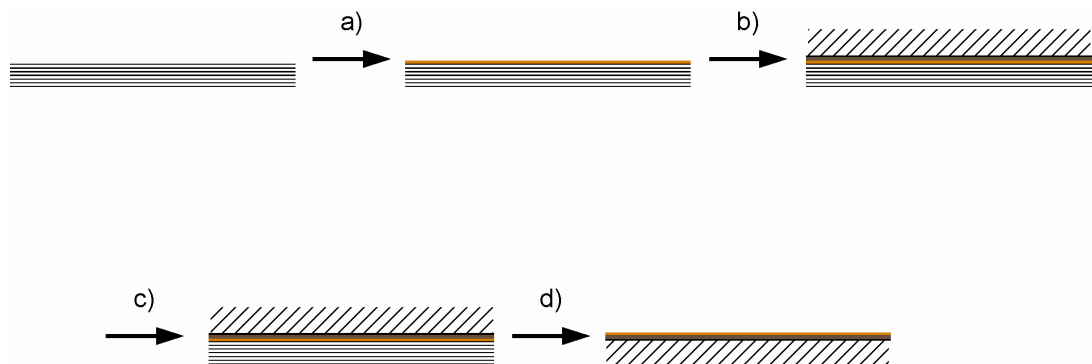


**Figure 2.8: Preparation steps of TSG; a) evaporation of gold, b) gluing of the glass substrate, c) curing of the epoxy glue, d) stripping.**

### 2.5.2. Cleaning of oxide surfaces

Different non-gold substrates have been used during this study, e.g. polished silicon wafers, BK7 glass or quartz. To ensure the cleanliness of those substrates, they were always subjected to the following treatment:

- 10min ultrasonic treatment (US) in a 2w% Hellmanex solution (Hellma, Germany)
- thorough rinsing with ultra pure water (MilliQ, Millipore, France), followed by 10min US in MilliQ
- 10min US in ethanol
- 60min at 65°C in a H<sub>2</sub>O<sub>2</sub>/NH<sub>3</sub>/H<sub>2</sub>O (10/10/50) solution
- thorough rinsing with MilliQ
- storage in ethanol

The substrates cleaned with this procedure showed a very low contact angle (WCA<10°) revealing their high cleanliness and hydrophilicity.

### 2.5.3. Monolayer formation by self-assembly

The self-assembling of molecules on a substrate to an oriented organic monomolecular layer from a solution is nowadays a quite known and widespread technique. It relies on the high affinity of a functional group of the molecule to the surface material.

The most prominent examples are alkane thiols, which spontaneously bind to gold, silver, platinum, palladium and other transition metals. In the early 1980, R.G. Nuzzo and D.L. Allara started to characterize organic disulfide films on gold substrates,<sup>[52, 53]</sup> and revealed their tremendous potential for the covering of large surfaces. The disulfide molecules were found to be very closely packed, having nearly the density of a bulk, with almost vertically stretched chains (tilt angle of approximately 30°). Thus, the properties of the covered interfaces were not influenced by the underlying gold substrate anymore but directly dependant on the chain length of the assembled molecules. Furthermore, the strong specific interaction between sulfur and gold (binding energy of ~150kJ/mol<sup>[52]</sup>) allows the formation of monolayers even in the presence of other functional groups.

Moreover, the same type of mechanisms could be observed by the binding of silanes<sup>[54]</sup> to oxide or nitride substrates and carboxylic acids on metal oxide<sup>[55]</sup>.

This preparation method has been also used for the formation of thiolipid monolayers during this study. Solutions of approximately 0,2mg/ml thiolipids in ethanol were prepared, where freshly stripped TSG slides were immersed for 24 hours. Afterwards, the gold slides rinsed with ethanol and dried under a nitrogen stream were ready-to-use.

#### *2.5.4. Bilayer formation by vesicle fusion*

The formation of bilayers by the fusion of lipid vesicles on hydrophobic substrates is not fully understood. Kalb et al.<sup>[56]</sup> tried to explain this mechanism by a three steps pathway: first the docking of a vesicle to hydrophobic surface, then the opening and the spreading of the outer leaflet of the vesicle, and finally the spreading of the inner leaflet as the original picture from the publication shows it (Figure 2.9).

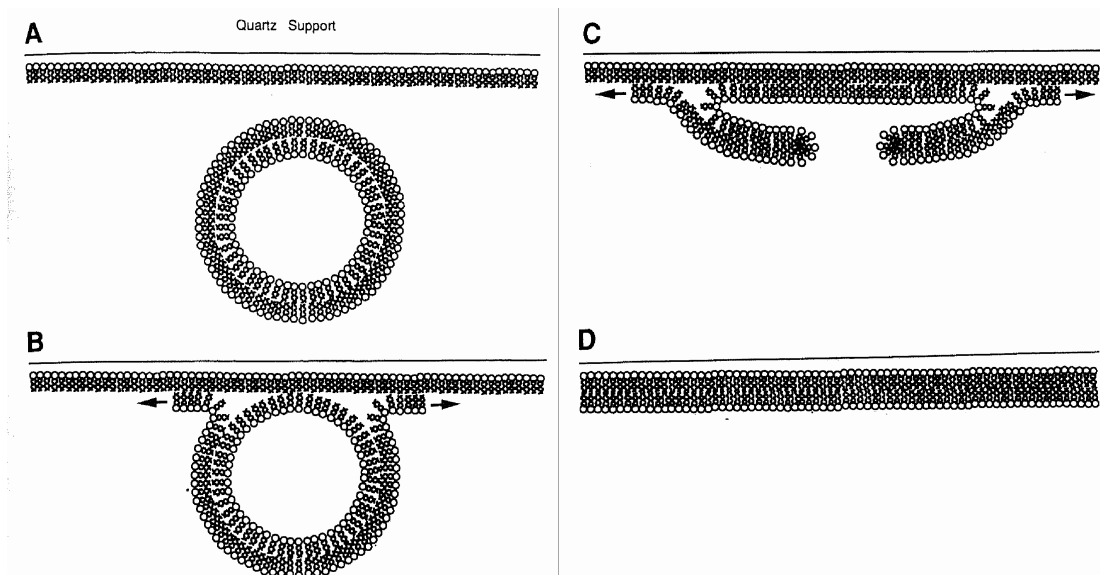


**Figure 2.9: Possible pathway for vesicle disintegration and fusion with a supported phospholipid monolayer<sup>[56]</sup>.**

In this study, the hydrophobic monolayers of diacetylene lipids were prepared either by LB transfer or self-assembly.

Vesicles of 50nm diameter were produced by extrusion of a 2mg/ml phospholipid solution in MilliQ. These vesicles were added to the monolayer, immersed in buffer solution (20μl vesicles/1ml buffer), typically 100mM NaCl. The fusion was usually done overnight.

#### 2.5.5. Bilayer formation by rapid solvent exchange method

Another way to create bilayers on top of a hydrophobic monolayer is to so-called rapid solvent exchange. In this method, a small amount of a lipid solution of higher concentration (7 to 10mg/ml) is prepared in a water miscible solvent, such as ethanol, and spread over the monolayer. After 10min incubation time, the rest of lipids is vigorously flushed away, first with an ethanol/water (25/75) mixture, second with water (or buffer solution) in large excess. To reduce the surface energy arising from the interactions of the hydrophobic monolayer in contact with water, the free lipids assemble into an upper leaflet, exposing the hydrophilic groups to water. The prime advantages of this method are the possibility to create bilayers very simply and rapidly and also to be able to flush the rests of adhering lipids or agglomerates from the surface of the bilayer by intensive rinsing.<sup>[57, 58]</sup>

## 2.6. Water contact angle (WCA)

The study of the interactions of a solid with liquids at its interface can give an idea of the attraction/repulsion forces acting between the two elements. By measuring the contact angle of a liquid droplet (in our case degassed water) deposited on a substrate, we get a numerical value directly proportional to the interfacial energies. The relation between the interfacial energies  $\gamma$  (same as in 1.4.1), respectively the solid and the liquid,  $\gamma_{SL}$  the liquid and the vapors,  $\gamma_{LV}$  the solid and the vapors,  $\gamma_{SV}$  and the contact angle is described by Young's equation:<sup>[59]</sup>

$$\gamma_{LV} \cos \theta = \gamma_{SV^0} - \gamma_{SL} \quad (2.3)$$

An implementation to Young's equation has been performed by *Bartell* and *Bartell* introducing the *adhesion tension A*, defined as:<sup>[60]</sup>

$$A = \gamma_{SV^0} - \gamma_{SL} = \gamma_{LV} \cos \theta \quad (2.4)$$

They showed the linear relationship between the cosine of the contact angle and the adhesion tension which increases with the hydrophilicity of the substrate. Following their definition, the substrate is hydrophilic for  $0^\circ < \text{WCA} < 90^\circ$  and hydrophobic for  $90^\circ < \text{WCA} < 180^\circ$ . We would rather start to consider a substrate as hydrophobic from a  $\text{WCA} > 75^\circ$ .

By probing the substrate with a water droplet, we can measure its hydrophilicity. Table 1 gives some examples of WCA for different substrates.

Substrate	Contact Angle [°]	Substrate	Contact Angle [°]
PTFE	112	Silicon Wafer (clean)	<10
Polyethylene	103	Glass (clean)	<10
Human Skin	90	Gold (clean)	0

**Table 1: Examples of WCA for different substrates.**

The question of the wettability of gold has been greatly assessed in the past, due to the fact that gold surfaces have been found as well hydrophilic ( $<10^\circ$ ) as hydrophobic ( $\sim 50^\circ\text{-}65^\circ$ ). *Smith* reviewed these works and showed that ultra pure gold surfaces are water wetting, but since gold is very rapidly contaminated by the environment (carbon dioxide, oxygen, alkanes) it becomes hydrophobic.<sup>[61]</sup> In our study, we used template stripped gold (see 1.5.1), where the clean gold substrate is stripped free directly prior use, reducing drastically possible contaminations.

The modification of a substrate with anchor lipids transforms a hydrophilic glass, silicon or gold substrate into hydrophobic, since the ordered alkyl chains are pointing away from the substrate. The degree of water repulsion of a surface depends greatly on the quality of the monolayer formed on top of it. WCA measurements become therefore a very easy way to roughly estimate the quality of the prepared film.

In this work, the WCA measurements were done following the sessile drop method, using a DSA 10 apparatus (Krüss CA, Germany) with the software Drop Shape analysis v1.5.

## 2.7. Ultraviolet-Visible Spectroscopy (UV-Vis)

Ultraviolet-visible spectroscopy (UV-Vis), as the simplest type of absorption spectroscopy is among the oldest of the fields of scientific specialization. First limited to visible light, then consecutively extended to the UV and infrared spectra. Intensive studies in the early 1800 recognized the presence of “characteristic frequencies” for the absorption by functional groups in molecules.

UV-Vis spectroscopy is based on the absorption of photons in the UV-visible spectrum of light by molecules, undergoing electronic transition. The electrons of the highest occupied orbitals are excited to unoccupied orbitals; this is the so-called HOMO-LUMO transfer. Most of the transfers occur between  $\pi$ - or  $n$ -orbitals and the  $\pi^*$ -orbital (see Figure 2.10).

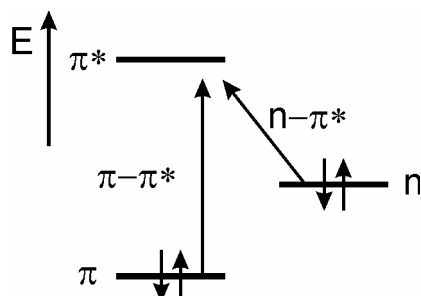


**Figure 2.10:** Schematic representation of the electron transfer in a molecule.

The groups of atoms absorbing energy in the molecules, known as chromophores, are often unsaturated functional groups, but also heteroatoms with free electrons. In conjugated  $\pi$  systems, the orbitals overlap and the energy necessary for the excitation is reduced, causing a red shift in the absorption spectra.

The positions of the absorption peaks depend on the substance and except for minor changes are not influenced by their environment. Furthermore the laws of absorption, introduced by *Bouguer, Lambert* and *Beer*, commonly known as the Lambert-Beer law<sup>[62]</sup> draw a quantitative relation between the absorbed light and the concentration of the absorbing material.

The highly conjugated polymer backbones, obtained by the polymerization of the diacetylene monomers possess a strong absorption in the UV-Vis region that can be used to determine the kinetic of the reaction.<sup>[26, 43, 63, 64]</sup>

All the experiments were performed on a Perkin-Elmer Lambda 9 UV-Vis spectroscope.

## 2.8. Electrical Impedance Spectroscopy (EIS)

Electrical Impedance Spectroscopy (EIS) is a widespread technique in material science for the understanding of processes occurring at the interfaces of conducting materials and their environment. This method has acquired a place of choice in biophysics, for the monitoring of processes occurring across membranes. It takes direct advantage from the fact that membranes build an impermeable barrier to ions and that protein activity often involves translocation of ions from the cytoplasm to the extracellular fluid (or vice versa), directly measurable as a current. On this basis, numerous studies have been performed to examine the properties of the bilayer first, then progressively tending to the creation of a biosensor.<sup>[8, 21, 65, 66]</sup>

### 2.8.1. Physical basis: definition of impedance

In an ideal electrical circuit, the relation between voltage (E in [V]) and the current (I in [A]) going through a circuit element describing his resistance to the flow of electrical current is described by Ohm's law:

$$R = \frac{E}{I} \quad (2.5)$$

where  $R$  (in  $[\Omega]$ ) represents the resistance.

However the response of complex systems cannot be described by Ohm's law since it is limited to ideal cases and is therefore independent from the voltage levels or frequency. For a more detailed description, the concept of impedance ( $Z$  in  $[\Omega]$ ) has been introduced.

Electrical impedance spectroscopy is performed by applying a sinusoidal potential to the system and measuring the resulting current. The resulting current has the same frequency than the applied potential, but phase shifted (see Figure 2.11).<sup>[67]</sup>

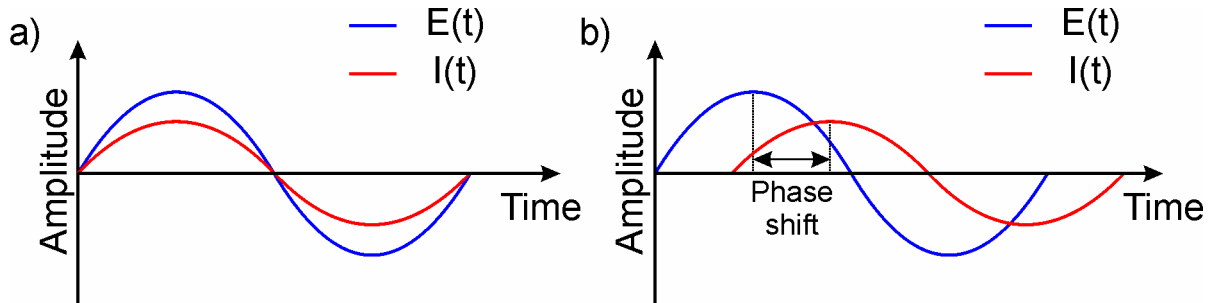


**Figure 2.11: Potential – current relation versus time; a) pure resistance, b) resistance and capacitance.**

In order to take the phase shift into account, the resistance  $R$  is replaced by the impedance  $Z$  as follow:

$$\begin{aligned} Z(\omega) &= \frac{E(\omega)}{I(\omega)} = \frac{E_0 \exp(i\omega t)}{I_0 \exp(i(\omega t - \varphi(\omega)))} \\ &= \frac{E_0}{I_0} \exp(i\varphi(\omega)) \\ &= |Z(\omega)| \exp(i\varphi(\omega)) \end{aligned} \quad (2.6)$$

where  $E_0$  and  $I_0$  are respectively the maximal amplitude of the potential and the current,  $i$  is the imaginary number ( $i = \sqrt{-1}$ ),  $\varphi$  the phase shift and  $\omega$  the radial frequency ( $\omega = 2\pi f$ ).

For this reason, the electrical impedance contains two parts, the real ( $Z'$ ) and the imaginary ( $Z''$ ) one:

$$Z(\omega) = Z'(\omega) + iZ''(\omega) \quad (2.7)$$

Measurements were performed in the frequency domain, i.e. sinusoidal potentials of defined frequencies were applied over the membrane and the resulting current responses were measured.

The obtained impedance spectra are plotted in the so-called Bode plot (see Figure 2.12), with log frequency on the X-axis and both absolute values of the impedance ( $|Z(\omega)|$ ) and the phase-shift ( $\varphi(\omega)$ ) on the Y-axis.

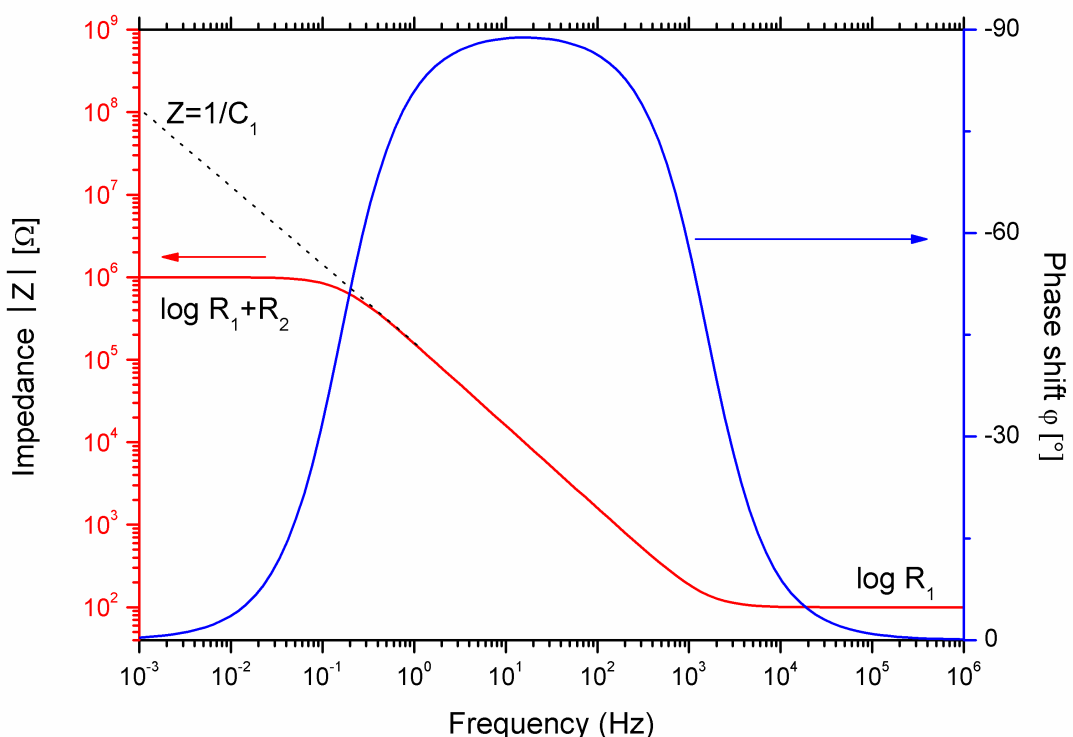


**Figure 2.12: Simulated Bode Plot of a simple electrochemical RC system.**

### 2.8.2. Measurement setup

The impedance spectra were recorded with a commercially available  $\mu$ Autolab impedance spectrometer with a Frequency Response Analysis (FRA) module from Metrohm (Filderstadt, Germany). Sine wave potentials were applied to the system and the corresponding currents were recorded. Amplitudes of 10mV were used, over a frequency range from 2mHz to 1MHz.

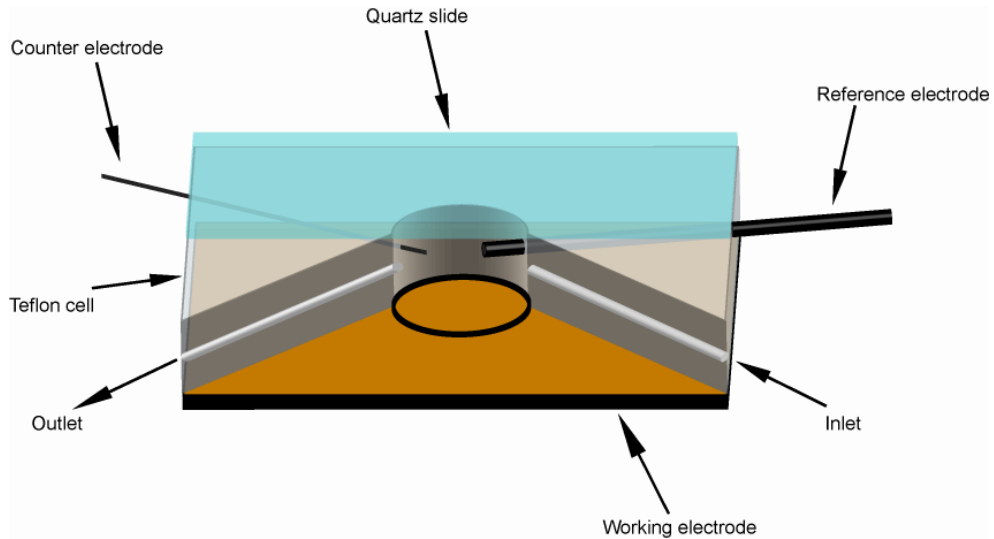


**Figure 2.13: Design of the used EIS cell.**

The home-made measurement cell used is depicted in Figure 2.13. The gold substrate was acting as a support for the membrane and as working electrode of the system, closing the measurement cell on one side. A quartz slide closed the cell from the other side permitting the UV illumination of the substrate during the measurements. As reference, a Dri Ref 2 electrode (World Precision Instruments, Berlin, Germany) was employed and a coiled platinum wire acted as counter electrode (0,8mm diameter, 99,9%, Mateck, Jülich, Germany). Liquid inlet and outlet were used to flush the cell. The cell had a buffer volume of 1ml and an electrode area of 0,385cm<sup>2</sup>. The results obtained by fitting the spectra with equivalent circuits were normalized to a 1cm<sup>2</sup> electrode size.

#### 2.8.3. Evaluation of the impedance data

The membrane response can be described in terms of a network consisting of several resistances and capacitances. The aim is to understand their physical origin, i.e. attribute them to a specific part of the system consisting of working electrode, membrane and electrolytes (sometimes defects can also be taken in account).

The simplest model used here to fit the tethered membrane system is presented below (see Figure 2.14). This is a four parameter network consisting of electrolyte resistance  $R_{elec}$ , membrane resistance  $R_m$ , membrane capacitance  $C_m$  and a capacitance due to the Gouy-Chapman-Stern layer at the membrane/electrolyte interface  $C_{GCS}$ .

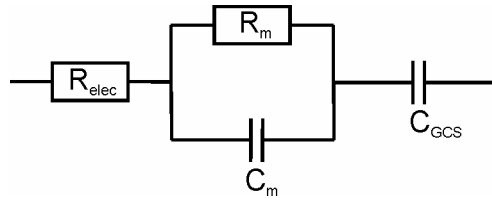


**Figure 2.14: Equivalent circuit used to simulate tethered bilayer membranes.**

## 2.9. Optical waveguide spectroscopy

A waveguide is a thin layer of dielectric material with a refractive index larger than 1. Light can propagate through the material due to the total internal reflection at the interfaces of the dielectric when the angle of the incident light is above the critical angle of total internal reflection:

$$\sin \theta_{critical} = \frac{n_{surrounding}}{n_{waveguide}} \quad (2.8)$$

Under specific reflection angles, constructive interferences occur when the light is reflected at the waveguide/surrounding interface. These specific angles of enhanced intensity are called modes. During light propagation in the waveguide, the total reflection happens partially outside of the dielectric material, creating a standing wave of light, decaying in intensity exponentially away from the interface. The theoretical description of this electromagnetic phenomenon is provided by the Maxwell equation, predicting two wave equations, one for each polarization direction (s- and p-polarized, leading respectively to TE and TM modes) with their solutions describing standing waves across the waveguide.

The solutions of these equations and therefore the resulting modes vary if the surrounding media changes in refractive index, thickness or density as showed in Figure 2.15.

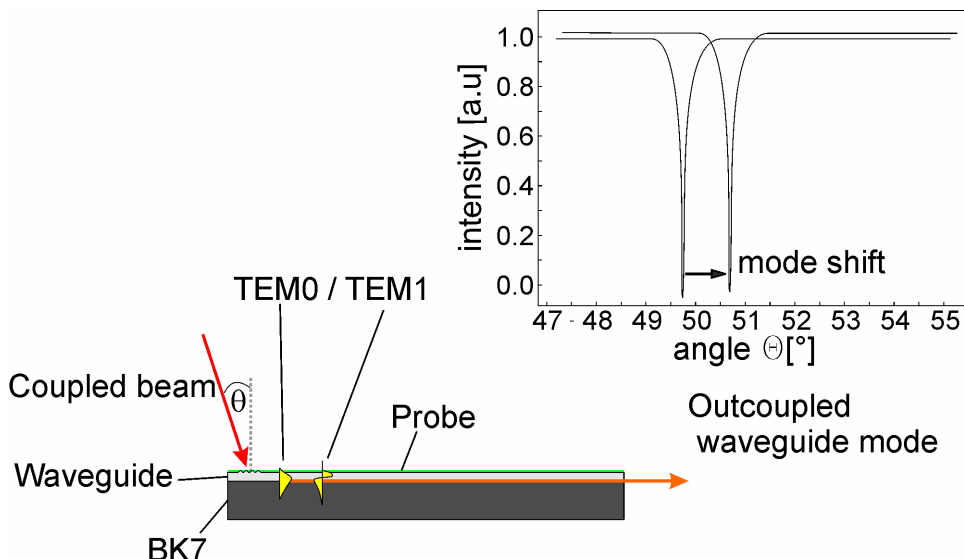


**Figure 2.15: Waveguide carrying an additional probe layer, resulting in an angle shift of the mode.**

In this study, optical waveguide spectroscopy was used to determine the transition temperatures of the monolayer on a substrate.<sup>[68]</sup> The membranes were transferred in a compressed state on a SiO<sub>x</sub>/TiO<sub>x</sub> waveguide, using LB film transfer technique. The waveguide was then subjected to a temperature ramp (0,1°C/min), using a Pelletier element and the resonance angle of the different modes was recorded each two degrees. A melting or glass transition temperature in the film appears as a kink in the temperature-waveguide mode angles, due to a change in the thermal expansion coefficient  $\beta$  as well as in the thermal refractive index coefficient  $k$ .<sup>[69]</sup>

## 2.10. Fluorescence recovery after photobleaching (FRAP)

Fluorescence recovery after photobleaching (FRAP) is a useful method to determine the molecular mobility of diffusing species in two dimensional architectures.<sup>[70, 71]</sup> From the analysis of the experimental results, diffusion coefficients and percentage of recovery after bleaching can be calculated.

Several experimental methods have been used in the past to determine the lateral diffusion in membranes. Methods based on bimolecular reaction such as Heisenberg spin exchange<sup>[72]</sup>, fluorescence quenching<sup>[73]</sup> or neutron scattering<sup>[74]</sup> measure diffusion over short distances. Whereas FRAP<sup>[70]</sup>, single particle tracking (SPT)<sup>[75, 76]</sup>, nuclear magnetic

resonance (NMR)<sup>[77, 78]</sup> or dissipation of electron spin resonance (ESR)<sup>[79]</sup> signal gradients measure diffusion over larger distances.

### 2.10.1. Measurement procedure and evaluation

The main steps for the FRAP method are as follows. First, the membrane is fluorescently labeled with  $\approx 1\text{ mol\%}$  1,2-dioleoyl-*sn*-glycero-3-phosphoethanolamine-N-(7-nitro-2-1,3-benzoxadiazol-4-yl) (DOPE-NBD) in 1,2-diphytanoyl-*sn*-glycero-3-phosphocholine (DPhyPC) (see Figure 2.16). The ability to bleach the fluorophores irreversibly with an intense light pulse is a prerequisite for lateral diffusion measurements. The sample is mounted in a water cell on top of a fluorescence microscope and an area of the membrane is focused. A small spot of the membrane ( $4.2\mu\text{m}$  in diameter) is illuminated with low intensity laser light with the appropriate wavelength (488nm) to excite the fluorophores. The fluorescence intensity is from now on continuously registered via a photomultiplier. Then, the light intensity is briefly elevated about  $10^6$ -fold (reaching an intensity of approximately 2W) over 60ms. This induces a rapid and irreversible photolysis of the fluorophores (more than 90% are bleached). After the bleaching period the light is attenuated to the previous level. If no lateral diffusion of the investigated membrane component takes place, the fluorescence signal evoked by the measuring beam remains constant. However, if lateral diffusion occurs, an increase of the fluorescence signal is observed due to the non-photolysed fluorophores entering into the illuminated area from the surrounding (see Figure 2.18). The time dependence of the fluorescence recovery is proportional to the lateral diffusion constant.

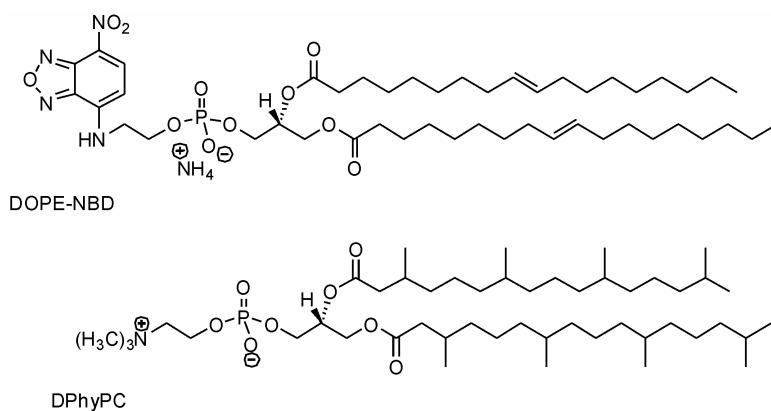


**Figure 2.16: Chemical structure of DOPE-NBD and DPhyPC.**

The measurements were performed on a home-build FRAP set-up, using an Olympus IX70 microscope and an Innova 90 laser (Coherent Inc., Santa Clara, USA), as shown in Figure 2.17.

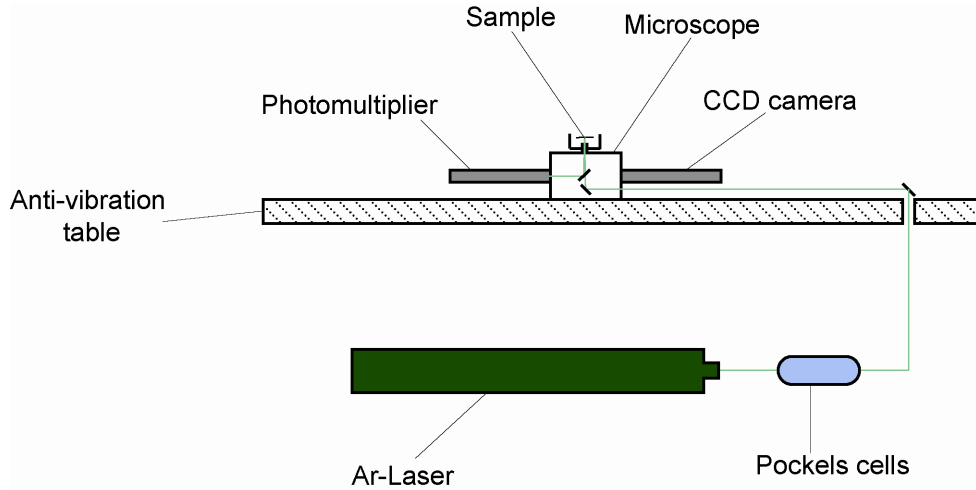


**Figure 2.17: Scheme of the FRAP setup.**

The following simplifying assumptions were made: the laser light intensity used for the measurement is low, so that photolysis is negligible during the record of the fluorescence signal. Second, the fluorophores can be irreversibly bleached within a time period that is brief compared to the diffusion time. The range of diffusion constants measurable with this technique ranges from some  $\mu\text{m}^2.\text{s}^{-1}$  to  $10^{-6}\mu\text{m}^2.\text{s}^{-1}$ .

From the obtained recovery curve, the diffusion coefficient was fitted, using the Simplex method.<sup>[70]</sup>

$$f(t) = F_\infty - [F_\infty - F_0] * \left\{ 1 - \exp^{-\frac{2\tau_D}{t}} * \left[ I_0\left(\frac{2\tau_D}{t}\right) + I_1\left(\frac{2\tau_D}{t}\right) \right] \right\} \quad (2.9)$$

$$\tau_D = \frac{\langle r^2 \rangle}{4D}$$

where  $I_0$  and  $I_1$  are the Bessel functions 0. and 1. order, and  $\tau_D$  the characteristic diffusion time.

Another parameter that can be extracted from the measurement is the percentage of recovery, defined by:

$$\text{Relative recovery} = \frac{F_\infty - F_0}{F_- - F_0} * 100\% \quad (2.10)$$

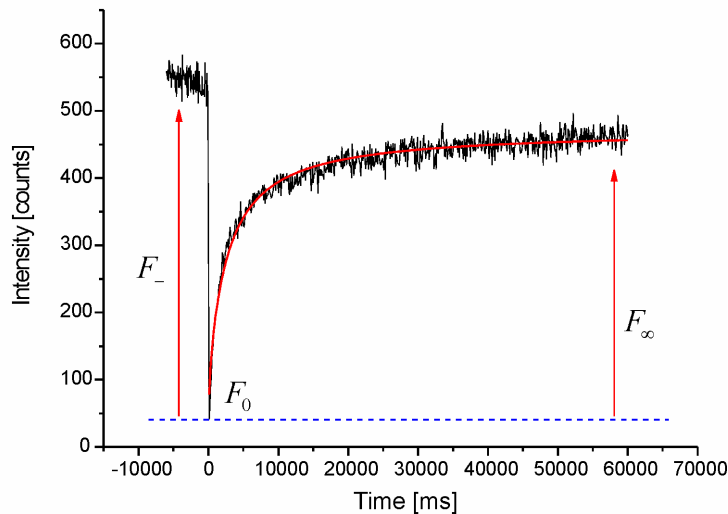


**Figure 2.18: Typical FRAP measurement, where  $F_-$  is the fluorescence intensity before bleaching,  $F_0$  the intensity directly after bleaching and  $F_\infty$  the recovered fluorescence; in red the fit curve.**

### 2.10.2. Theory of diffusion

Two theories for the diffusion in homogeneous bilayers have been formulated. The first is a continuum hydrodynamic model for diffusion of particles the size of which is much larger than that of the solvent. This model describes well the diffusion of integral membrane proteins in lipid bilayer.<sup>[80, 81]</sup> The second is a free-volume model, which takes in account the discreteness of the lipid bilayer and is therefore best suited for the description of lipid diffusion.<sup>[39, 82]</sup>

Basically, in a homogeneous, two-dimensional system the diffusion coefficient  $D$  can be defined through the relation:

$$\langle r^2 \rangle = 4Dt \quad (2.11)$$

where  $\langle r^2 \rangle$  is the mean square displacement of a randomly moving tracer, and  $t$  is time. This mean square displacement is the second moment of the Gaussian probability distribution of displacements.

$$C(r,t) = \frac{1}{4\pi Dt} \exp\left(-\frac{r^2}{4Dt}\right) \quad (2.12)$$

which is the solution of the diffusion equation,

$$\frac{\partial C(r,t)}{\partial t} = D\nabla^2 C(r,t) \quad (2.13)$$

$C(r,t)$  is the concentration of the fluorescent material,  $r$  the spot radius,  $t$  the time and  $\nabla^2$  the Laplace operator.

Hence,

$$\langle r^2 \rangle = \int_0^\infty r^2 C(r,t) d\sigma = 4Dt \quad (2.14)$$

where  $d\sigma = 2\pi r dr$ .

Whenever the probability density  $C(r,t)$  is a Gaussian distribution at long times (large distances) the diffusion coefficient is a well-defined quantity.

Even if the diffusion in two dimensions is for the most part understood from a theoretical point of view, confusion raised from divergences on experimental results. There are some discrepancies between long range and short range diffusion coefficients. To resolve the differences, theories have been formulated that go well beyond the scope of this study.

Anyhow, FRAP as a long range diffusion measurement method, is valid for the type of question we want to solve.

### 3. Ultra flat heterogeneously structured substrates

The aim of this study was to develop a new method for the patterning of membranes, based on the anchored lipids model. Previous attempts to create membrane corrals were reported by polymerizing solid supported membranes (SSM)<sup>[33]</sup> or spreading vesicles over substrates structured into an array of wells.<sup>[35, 37, 38]</sup> As discussed in the introduction, SSMs were not of direct interest because of the lack of submembrane spacing, inhibiting the incorporation or even causing denaturation of transmembrane proteins due to contacts with the substrate. Also the utilization of macroscopic polymeric barriers, patterned on top of the substrate would not fulfill the expectations, since the arrangement of the lipids in direct vicinity with these separators is not known and can be the source of leakage current. The synthesis of anchor lipids with polymerizable groups was therefore preferred.

In parallel, a bottom up approach for the membranes patterning was also followed by engineering the platform. The construction of a flat, laterally structured substrate was undertaken, combining gold pads embedded in a silicon dioxide matrix. This would permit the straightforward and selective assembly of the monolayer onto these patterns using thiol or silane anchors.

#### 3.1. Photolithographic Structuring

##### 3.1.1. Concept

Studies of tBLMs on microelectrodes have recently shown the advantage of size reduction of the working electrode.<sup>[83]</sup> The specific resistance per cm<sup>2</sup> of the bilayer remained the same as on larger electrodes, but due to the small size of the substrates the overall resistance is dramatically increased and the capacitance decreased.

In order to reach a micrometric structuring of the substrates, photolithographic patterning and lift-off technique were combined in a process including different evaporation steps as shown in Figure 3.1.

This procedure was based on a reversed TSG approach, where the ultra-flat gold acts as templating substrate. The selective evaporation of silicon oxide (SiO<sub>x</sub>) followed by chromium (Cr) on the open free gold (Au) spots (the rest of the substrate being covered by

the photoresist), created wells for the evaporation of the gold electrodes. Chromium plays a role of adhesion promoter between silicon oxide and gold. Silicon oxide was achieved by the thermal evaporation of a silicon monoxide precursor with a partial pressure of  $2.10^{-4}$ mbar oxygen in the chamber.

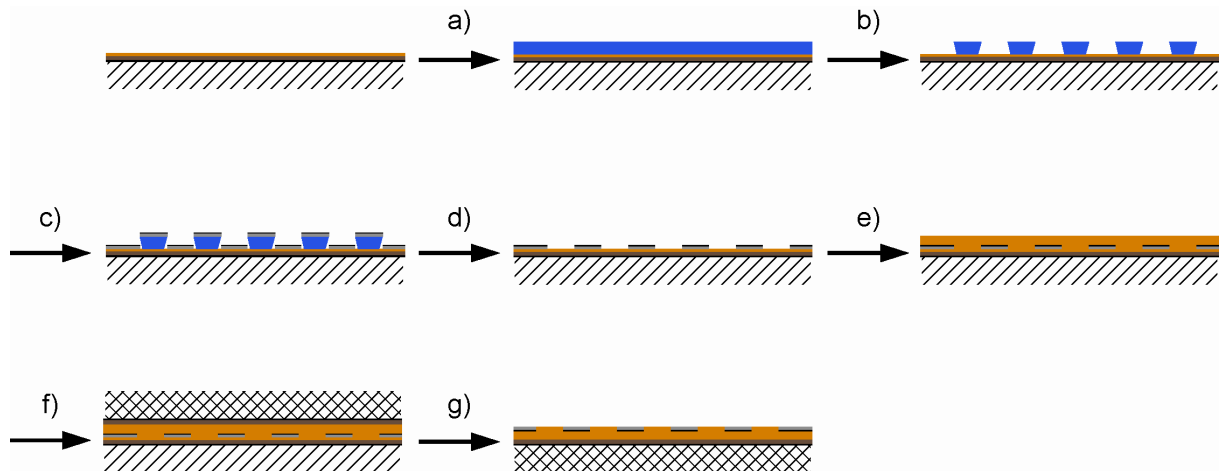


**Figure 3.1: Scheme of preparation of microelectrodes; a) spin coating of photoresist on TSG, b) structuring of the resist with photolithography, c) evaporation of  $\text{SiO}_x$  and Cr on the photoresist, d) lift off of the resist, e) evaporation of gold, f) gluing of a glass slide on top of the gold and curing, g) stripping.**

### 3.1.2. Photolithography

This technique, well known from the semi-conductor industry, imprints patterns into a photosensitive resin by high energy illumination (UV-light) through a chromium mask.

The photoresist used was a negative type AZ nLof 2070 (MicroChemicals, Ulm, Germany), where the exposed resist remains after development. The resist is made out of novolak, a cresol polymer synthesized from phenol and formaldehyde (see Figure 3.2).

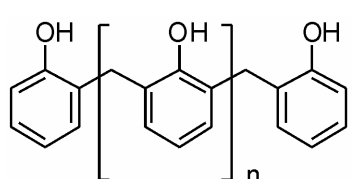


**Figure 3.2: Novolak resin**

To mixtures of novolak oligomers, typically 8 to 20 monomers, photoinitiators belonging to the group of diazonaphthoquinones are added, reducing the alkaline solubility of the resins upon UV-illumination. After completion of the photolithographic process, the polymeric film can be removed without remnants by an overnight

immersion in N-methyl pyrrolidone (NMP).

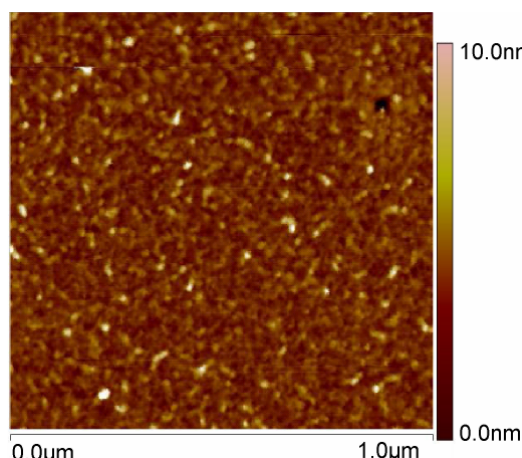
The lithographic process:

- Drying of the substrates on a hot plate at 110°C for 2 minutes

- Spin coating of the photoresist at 4000rpm for 20sec, producing a film thickness of 5,5 $\mu$ m
- Soft backing of the film at 110°C for 60sec
- UV illumination with a mask-aligner (MA-25, Karl Süss GmbH, Deutschland) for 2sec
- Hard backing of the film at 110°C for 50sec
- Development in AZ 726 developer for 50sec
- Evaporation steps
- Removal of the photoresist by overnight treatment with NMP

### 3.1.3. Success and limits of the method

The described procedure was based on the possibility to peel off a structured SiO<sub>x</sub> film evaporated on a TSG substrate. As prerequisite to the successful construction of an ultra-flat gold / SiO<sub>x</sub> array, the stripped oxide film had to be as flat as the TSG template. For this purpose, probes without photoresist have first been prepared by the successive evaporation of SiO<sub>x</sub> (50nm), Cr (5nm), Au (100nm) on TSG substrates and glued on freshly cleaned glass. The roughness of the obtained films was determined by Atomic Force Microscopy (AFM, measurements done by H. Burg, AK. Butt, MPIP). The chemical composition of the film in cross-section has been obtained with Energy-Dispersive X-Ray spectroscopy (EDX, measurements done by Dr. I. Lieberwirth, AK. Wegner, MPIP).



From the AFM picture (Figure 3.3) a RMS roughness of 0,76nm has been calculated. This value is higher than for a typical TSG but still flat enough to properly accommodate a tBLM. Some major defects are nevertheless present on the surface, taking the forms of larger peaks with a typical base width between 25 and 50nm and a height ranging between 1,5 and 3nm.

**Figure 3.3: AFM height image of the stripped SiO<sub>x</sub> surface.**

For EDX measurements, a part of the thin film has been mechanically removed from the glass slide and embedded in a polymer matrix. In this way, a transverse cut of the film could be performed and so expose all the components of the film. On the scanning electron microscope (SEM) pictures in Figure 3.4, the successively evaporated films can be clearly seen due to the difference in electron density of the materials.

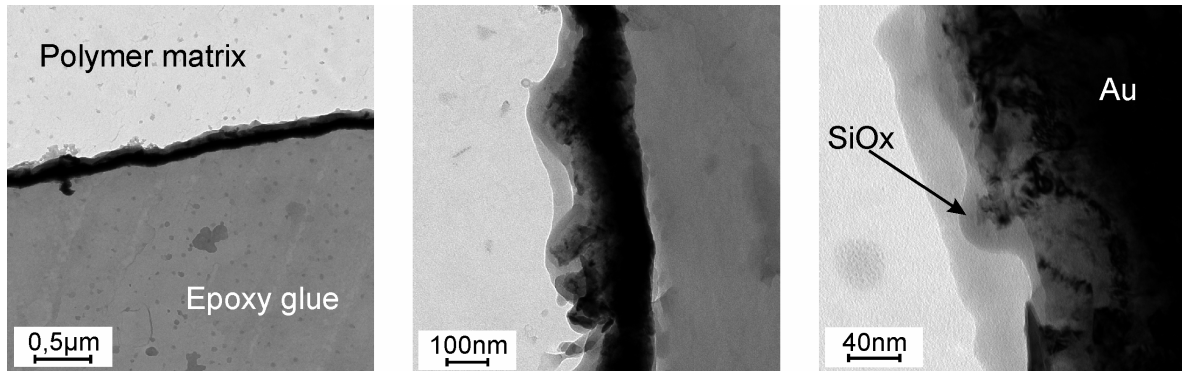


**Figure 3.4:** SEM pictures of a transversal cut of a thin  $\text{SiO}_x/\text{Cr}/\text{Au}$  film.

The EDX analysis done simultaneously with the SEM images (see Figure 3.5), confirmed the assumption, predicting the detachment of the  $\text{SiO}_x$  from the Au of the TSG. The buckling of the film was due to the mechanical stress applied to remove the glued film from the glass slide. For this reason, the parts of the  $\text{SiO}_x$  appearing in lighter gray are simply in the background.

The material analysis was done following the white line in the inset of the picture. The great advantage of this method is the quantitative determination of the elements with respect to the position on the sample. On each side of the film, a high signal of carbon, coming from the epoxy glue and the polymer matrix, was recorded. The composition of the film was as expected, with gold on the left hand side and a chromium-silicon oxide combination on the other side. As a side effect of the EDX study, the ratio of oxygen to silicon could also be determined and is approximately 2:1, as for silicon dioxide.

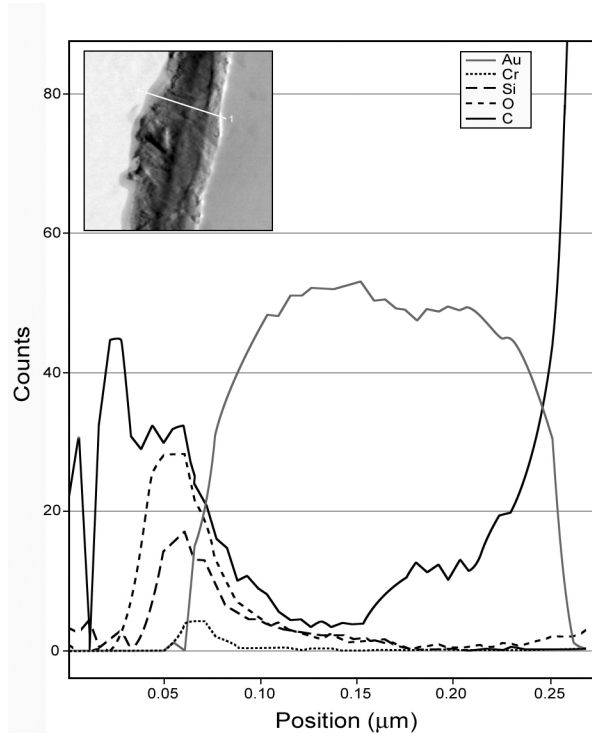


**Figure 3.5:** EDX analysis of the  $\text{SiO}_x/\text{Cr}/\text{Au}$  film.

In a second step, photolithographically structured substrates were prepared, accordingly to the preparation method described before (see 3.1.1). Figure 3.6 shows the AFM pictures of a 25 $\mu$ m gold square pattern in a SiO<sub>x</sub> matrix.

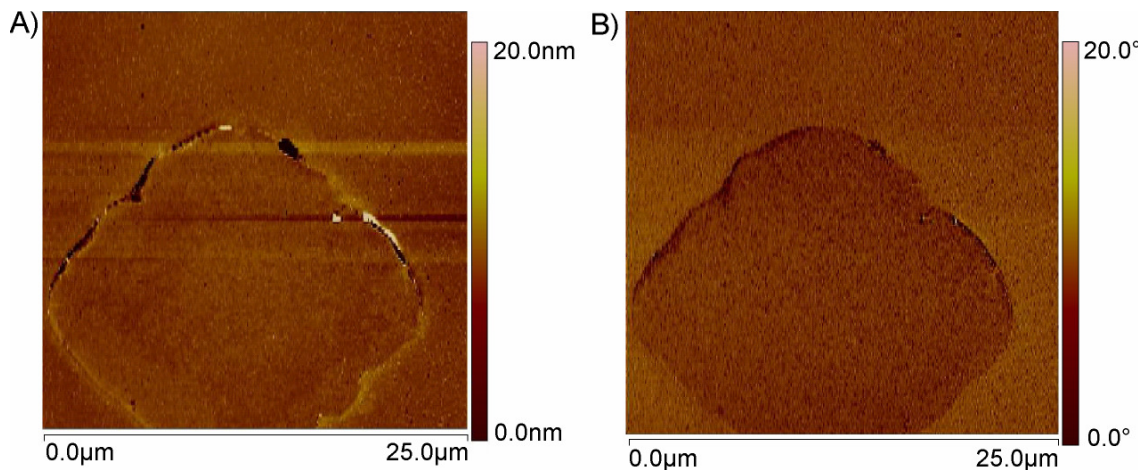


**Figure 3.6: AFM pictures of an embedded gold electrode; A) height image, B) phase image.**

On the height image, clear traces of a step between the two areas can be distinguished, whereas the phase image reveals the difference of hardness between the both materials. The calculated RMS roughness of the gold pad was 1,21nm, which is already to high for tBLMs.

The following line scan over the gold pad underlines the existing step at the edge of the electrode (see Figure 3.7).

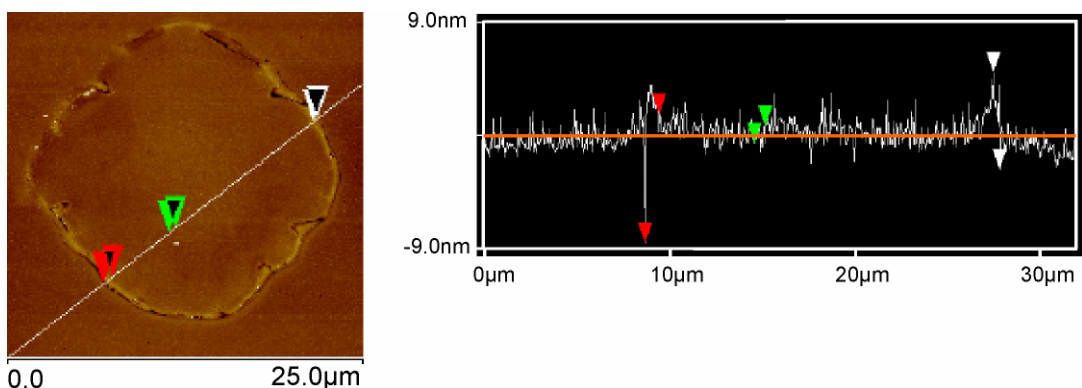


**Figure 3.7: Line scan over the gold electrode.**

Markers	Red	Green	White
Vertical distance between markers	10,23 nm	1,36 nm	7,64 nm

**Table 3.1: Vertical distances between the markers on the line scan.**

The reasons for the step at the edge of the gold electrode could not be precisely addressed, but were presumed to be directly related to the photoresist process. Also the surface roughness of the gold was too high and a surface passivation by self-assembly of a protective monolayer had to be considered.

### 3.2. Direct evaporation through a mask

The rest of the work related to the creation of heterogeneous ultra-flat substrates has been done by Nicolas Vogel during his diploma thesis, realized at the MPI-P and filed at the Institute of Organic Chemistry, University of Mainz. The results presented here with his permission only summarize his work.

#### 3.2.1. Protection of the TSGs with monolayers

The TSGs were functionalized with SAMs of different thiol-molecules before application of the photoresist. The tested molecules were in a range from C<sub>3</sub> to C<sub>18</sub>, with different end groups rendering the surface either hydrophilic or hydrophobic. The chemical structure of the used molecules can be seen in Figure 3.8.

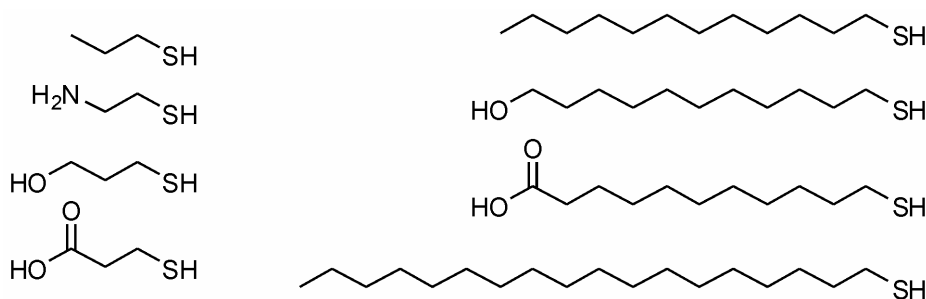


**Figure 3.8: Thiol molecules used for the surface modification of the TSGs.**

The complete covering of the TSGs with thiol-monolayers did not lead to significant successes. The stripped substrates showed numerous defects, e.g. gold pads sticking to the TSGs producing three dimensional cubes or holes in the probe.

Afterwards, an attempt was done to only functionalize the cavities on the TSGs, after the first evaporation step and lift-off of the photoresist. Two thiols, namely 3-

mercaptopropionic acid and 11-mercaptoundecanoic acid, induced breaking in the predetermined plane of the probe.

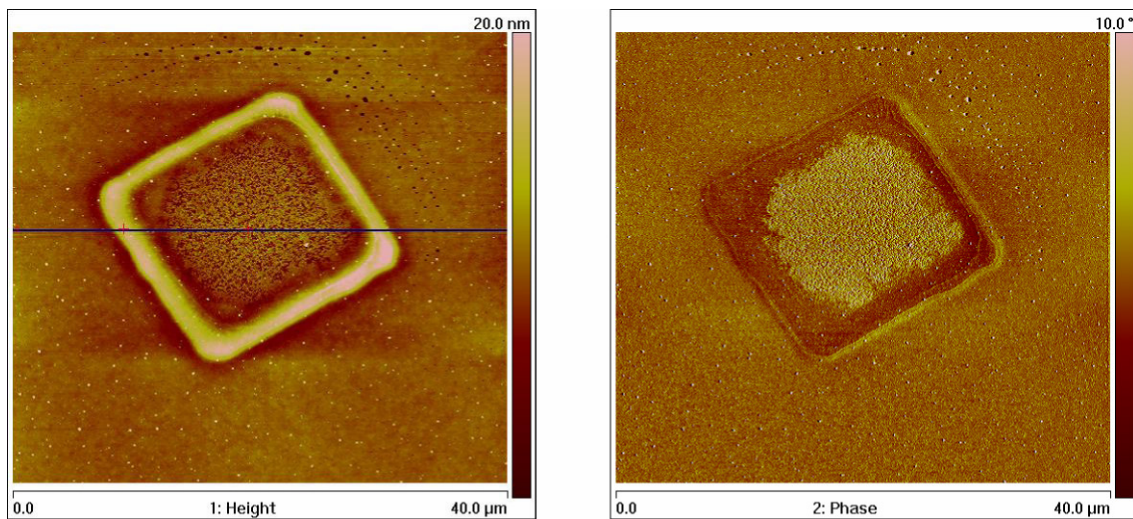


**Figure 3.9: AFM pictures of the stripped probe modified with mercaptoundecanoic acid after lift-off.**

The resulting probes were analyzed with AFM (see Figure 3.9). A ring appeared at the edges of the gold pad with a height of approximately 10nm. Moreover the RMS roughness of the stripped gold was again in the order of 1,5 to 2,0nm.

### 3.2.2. Direct evaporation

The use of TSG as templating substrate was abandoned in favor of silicon wafers. Therefore, trials were done to passivate these with silane-monolayers in order to reduce the adhesion of the evaporated  $\text{SiO}_x$  to the substrate. The silanes used for this purpose are presented in Figure 3.10.

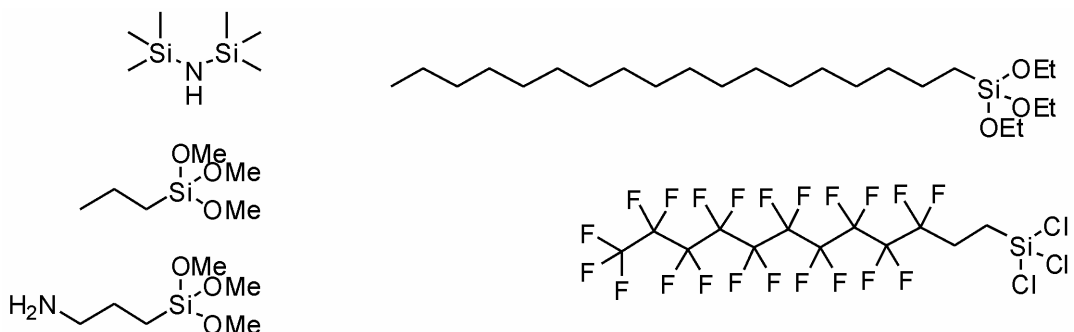


**Figure 3.10: Silanes used for the passivation of the silicon wafers.**

Hexamethyldisilazane, n-octadecyltriethoxysilane and heptadecafluoro-1,1-2,2-tetrahydrododecyltrichlorosilane induced successful separation in the predefined plane.

The principle of the preparation method is depicted in Figure 3.11.

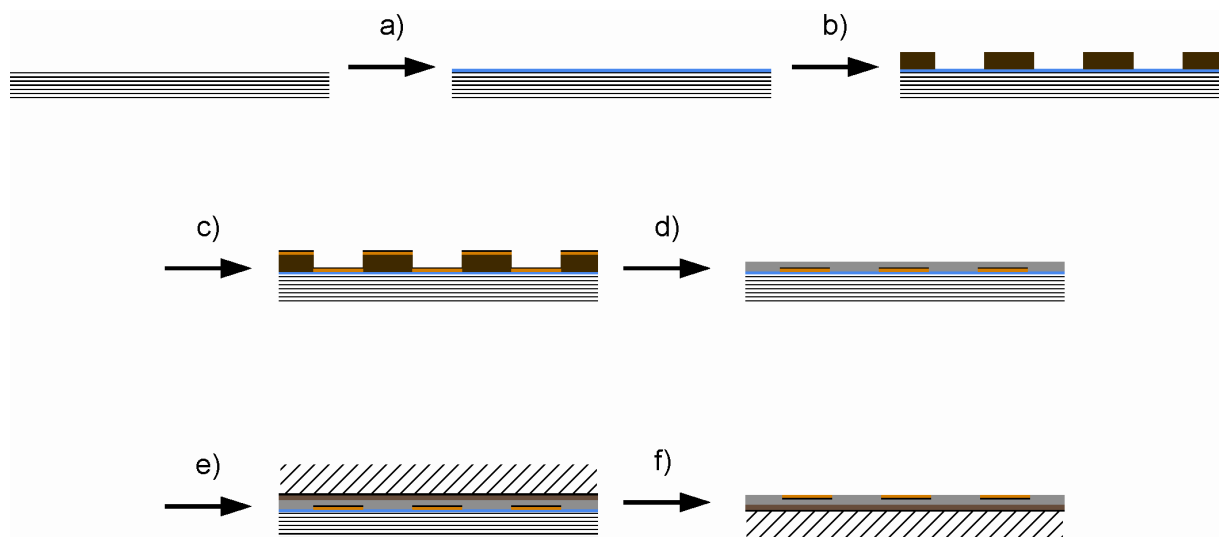


**Figure 3.11:** Scheme of preparation of microelectrodes via direct evaporation; a) passivation of the silicon wafer with silanes, b) fixation of the mask on the wafer, c) evaporation of Au and Cr on the wafer, d) removal of the mask and evaporation of  $\text{SiO}_x$ , e) gluing of a glass slide on top of the gold and curing, f) stripping.

The advantage of this method compared to the previous one using photoresist is the absence of organic residues that could stick to the surface after lift off, leading to an enhanced adhesion of evaporated material (Au or  $\text{SiO}_x$ ) to the template.

The Au/Cr evaporation was carried out through a micrometer meshed mask. In this study, transmission electron microscope (TEM) grids with mesh sizes between  $5\mu\text{m}$  and  $50\mu\text{m}$  were used. Additionally, colloidal monolayers were employed as masks to produce patterns with nanometer dimensions. Extremely smooth substrates were obtained without any step between the two materials, as can be seen in Figure 3.12 and Figure 3.13.

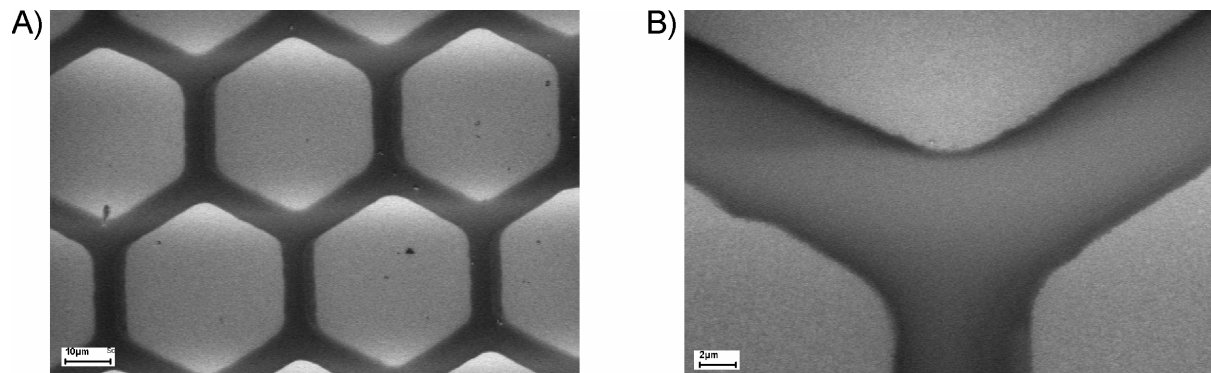


**Figure 3.12: SEM pictures of the hexagonally structured substrate after stripping.**

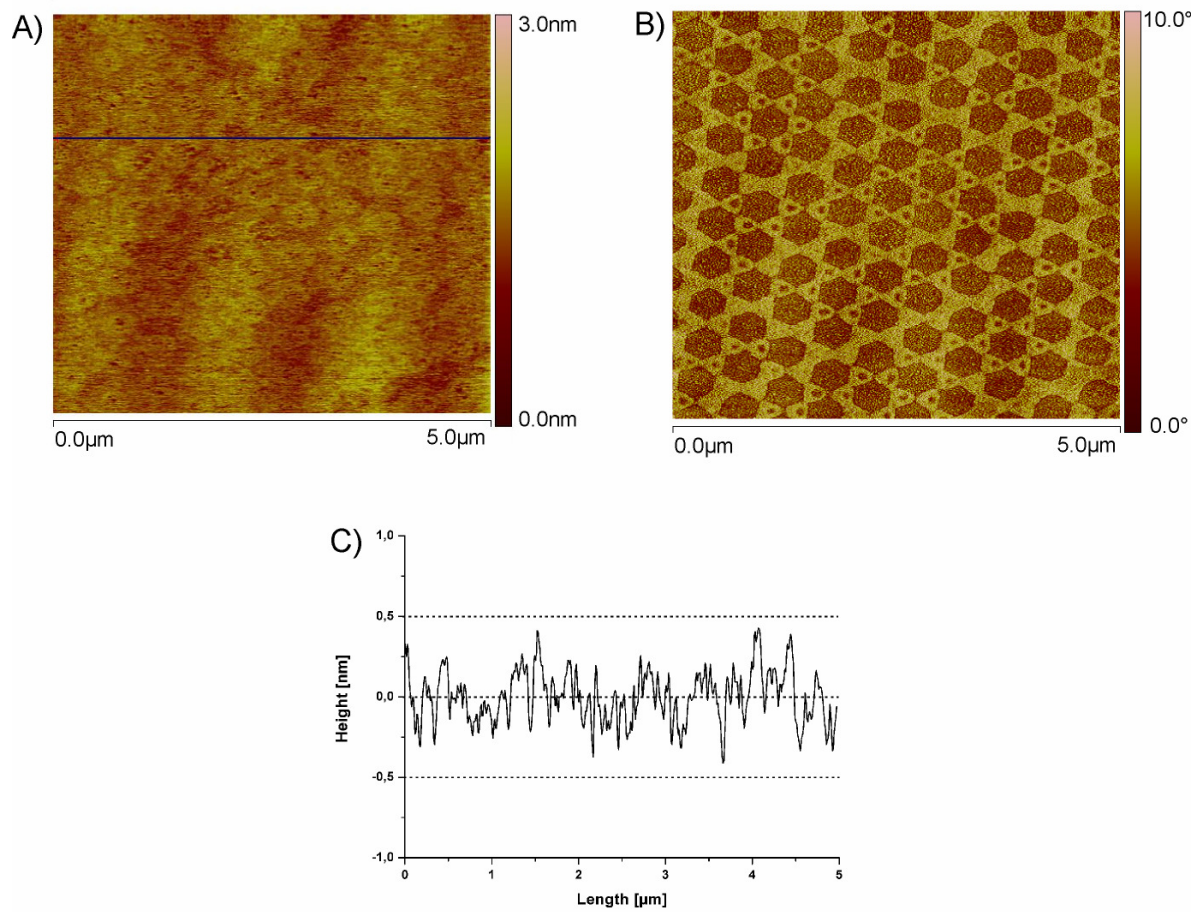


**Figure 3.13: AFM pictures and line scan over junctions between two materials obtained by nanosphere lithography (550nm colloids); A) height image, B) phase image, C) line scan.**

### *3.2.3. Selective functionalization of the substrates*

After the construction of these ultra-flat, heterogeneously patterned substrates, the selective functionalization of each part had to be shown. For this purpose, SAMs were selectively deposited on each material, rendering them hydrophobic, since both Au (clean) and SiO<sub>x</sub> are of hydrophilic nature. To reveal the hydrophilicity, or hydrophobicity, the samples were cooled with dry ice, inducing condensation of water droplet on the surface. Through the changing of illumination on the optical microscope, either from the top or from the bottom, the two different surfaces could be seen independently.

On the first sample, the gold pads were functionalized with perfluoro-1,1-2,2-tetrahydrodecanthiol, turning them hydrophobic and keeping the SiO<sub>x</sub> parts hydrophilic; whereas the second sample on the contrary was silanized with n-octadecyltriethoxysilane. The optical microscope pictures in Figure 3.14 show the samples before and after functionalization.

The pictures clearly reveal the change of wettability of the gold pads or the SiO<sub>x</sub> matrix with respect to the type of monolayer employed. This demonstrates the possibility to selectively deposit a monolayer on each surface independently.

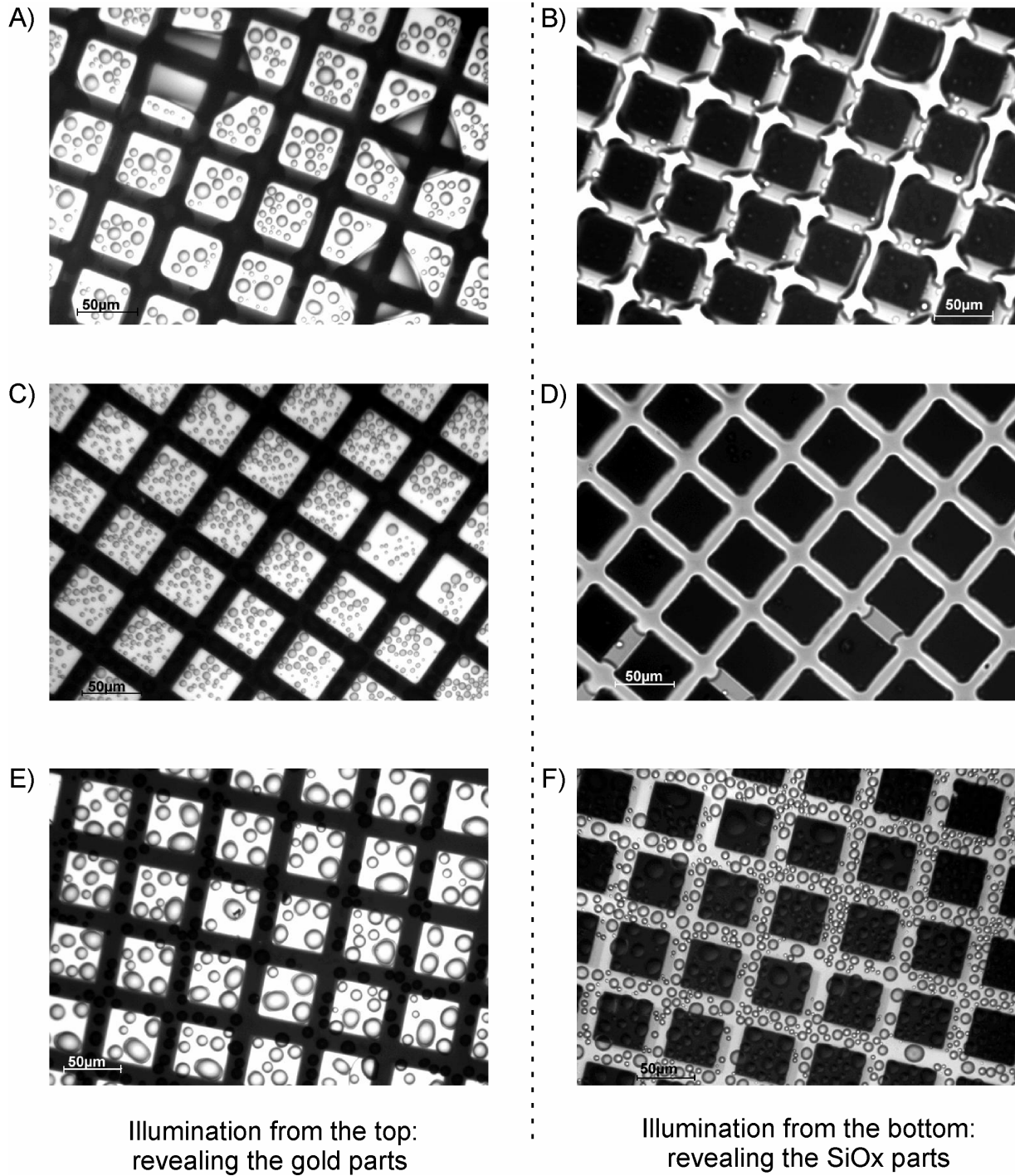


**Figure 3.14: Functionalization of the substrate:** A) and B) reference sample, without functionalization, C) and D) sample functionalized with perfluoro-1,1-2,2-tetrahydrodecanthiol, E) and F) sample functionalized with n-octadecyltriethoxysilane.

In order to determine how sharp the transition of a monolayer between two materials was, AFM pictures were taken at the SiO<sub>x</sub> – Au interfaces, on samples modified with n-octadecyltriethoxysilane.

Figure 3.15A shows the AFM height image of an originally flat substrate, partially covered by a monolayer on the  $\text{SiO}_x$  areas. A clear sharp transition at the edge of both materials can be seen. The monolayer formed over the  $\text{SiO}_x$  part (right side of the picture) does not show any defects while the Au area (left side) is not affected by the silane-monolayer formation. This proves the possibility to independently form monolayers on the respective area without affecting the other part.

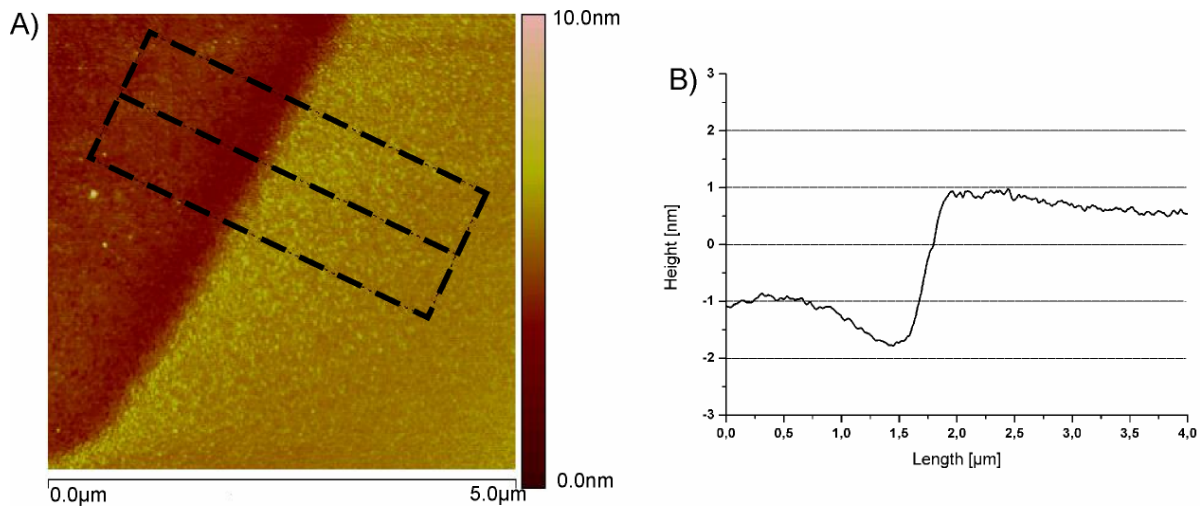


**Figure 3.15: AFM height image (A) and line scan (B) of a structured substrate at the Au -  $\text{SiO}_x$  interface, after modification with n-octadecyltriethoxysilane.**

Figure 3.15B shows the step analysis, performed within the dashed box on Figure 3.15A. As previously noted from the AFM height image, there is a step-like transition due to the presence of the monolayer on the sample. The overshoot of the line scan on the lower side is most probably an artifact. Depending on where the step height is measured, a monolayer thickness ranging from 1,8nm to 2,4nm is determined. This value agrees well with the one calculated in the literature of 2,1nm<sup>[84]</sup>, with the assumption of fully stretched molecules, tilted with an angle of 30° with respect to the normal.

## 4. Synthesis

### 4.1. General remarks

With exception of heptacosa-10,12-diyn-1-ol and heptacosa-10,12-diynoic acid, kindly provided by Prof. Ringsdorf, all the reagents were purchased from commercial sources, mostly from Sigma-Aldrich (Schnelldorf, Germany) and used without further purification. The solvents were purchased from Fischer Scientific (Niderau, Germany) in HPLC grade and the dry solvents from Across Organics (affiliated Fischer Scientific, Niderau, Germany).

The purification after each reaction was done by column chromatography, using Acros Organics (Geel, Belgium) silica gel 60A with a positive nitrogen pressure. All reactions were followed by thin layer chromatography (TLC) on Alugram Sil G/UV form Macherey-Nagel (Düren, Germany). The developer used to reveal the presence of molecules on the TLC was a mixture of resorcinol monomethyl ester and sulfuric acid (1:1) in ethanol.

The purity of the obtained products was checked with NMR and mass spectrometry.

## 4.2. Ether linked molecules

### 4.2.1. General procedure

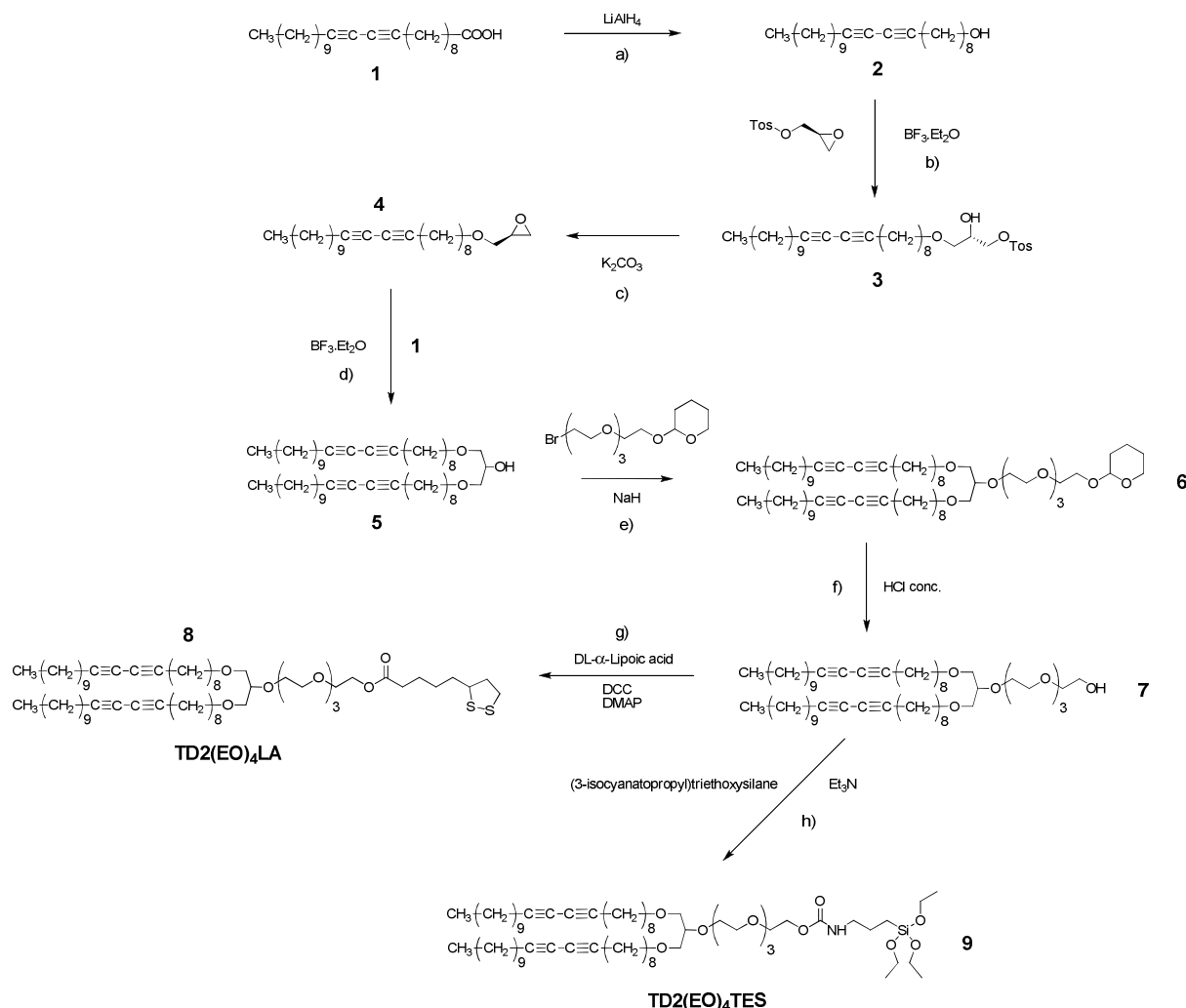
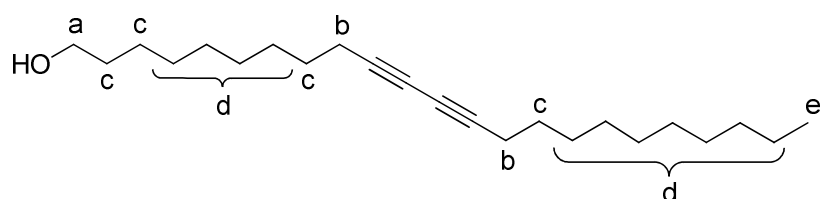


**Figure 4.1:** Synthesis scheme for TD2(EO)<sub>4</sub>LA (**8**) and TD2(EO)<sub>4</sub>TES (**9**)

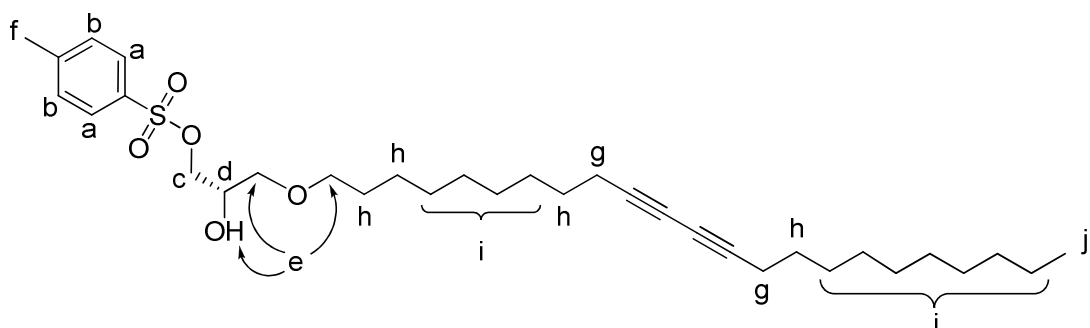
a. Tricoso-10,12-diyne-1-ol (**2**) <sup>[85]</sup>:



3,5g (10,1mmol) tricosa-10,12-diynoic acid in 25ml dry diethyl ether were added to a solution of 0,77g (20,2mmol) LiAlH<sub>4</sub> in 30ml dry diethyl ether. The mixture was heated to reflux for one hour. The reaction mixture was then poured into a separatory funnel, containing 100ml of an ice-water mixture, acidified with a 5% HCl solution (pH ~ 1-1,5). The ether layer was dried over Na<sub>2</sub>SO<sub>4</sub>, then filtered through a silica gel packed column to give 3,22g (yield: 96%) of tricosa-10,12-diyn-1-ol (**2**) in form of white crystals.

**<sup>1</sup>H NMR** (250 MHz, CDCl<sub>3</sub>) δ [ppm] 3.62 (t, 2Ha), 2.22 (t, 4Hb), 1.61 – 1.38 (m, 8Hc), 1.33 – 1.18 (m, 22Hd), 0.86 (t, 3He). The alcohol proton form –CH<sub>2</sub>–OH could not be seen.

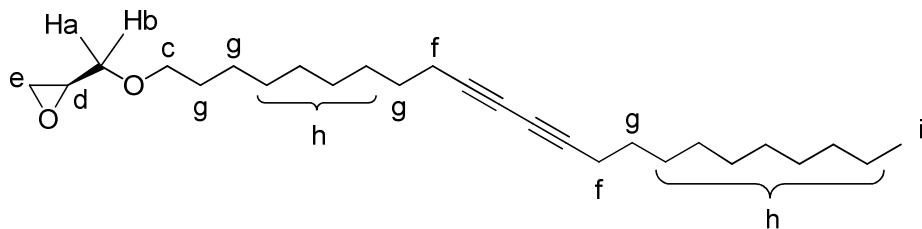
b. *2-hydroxy-3-(tricosa-10,12-diynyoxy)propyl p-methylbenzenesulfonate (3)* <sup>[86]</sup>:



0,81g (3,55mmol) (2S)-(+)-glycidyl tosylate were introduced under argon in a 250ml three-necked flask and diluted in 50ml dry dichloromethane. Then 1,30g (3,91mmol) of **2** was added to the mixture and stirred until complete dissolution. Approximately 30μl (5-7mol%) boron trifluoride diethyl etherate were added dropwise. The reaction mixture was stirred overnight at room temperature and monitored via TLC. After completion of the reaction, 20ml of water were slowly dropped to the reaction to neutralize the remaining boron trifluoride. The aqueous phase was extracted three times with dichloromethane and the combined organic phases were then dried over MgSO<sub>4</sub>. After filtration and concentration, the reaction mixture was purified via flash chromatography. Eluents: hexane/ethyl acetate (1:1); R<sub>f</sub> ≈ 0,60.

Yield: 1,50g (75%)

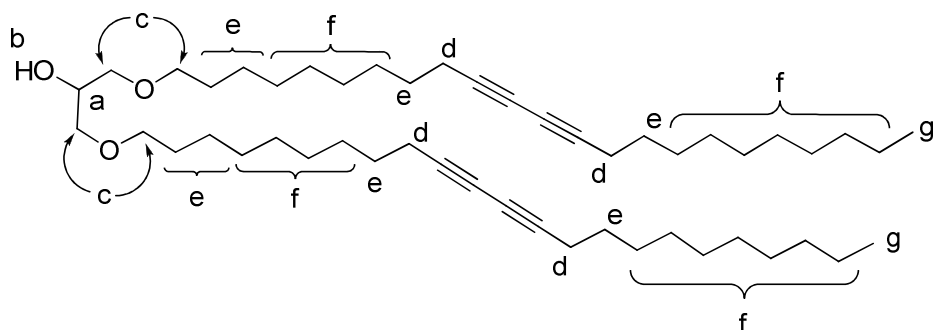
**<sup>1</sup>H NMR** (250 MHz, CDCl<sub>3</sub>) δ [ppm] 7.78 (d, 2Ha), 7.33 (d, 2Hb), 4.14 – 3.91 (m, 2Hc), 3.62 (t, 1Hd), 3.50 – 3.29 (m, 5He), 2.43 (s, 3Hf), 2.22 (t, 4Hg), 1.56 – 1.41 (m, 8Hh), 1.30 – 1.17 (m, 22Hi), 0.86 (t, 3Hj).

c. *2((tricosa-10,12-diynyoxy)methyl)oxirane (4):*

In a three necked round bottomed flask, a solution of 1,77g (3,16mmol) of **3** in 100ml dry methanol was prepared under argon. The solution was cooled down to 0°C and 0,87g (6,32mmol) K<sub>2</sub>CO<sub>3</sub> were added step-wise. The mixture was left stirring for 3 hours at 0°C. The reaction was monitored via TLC. Eluents: hexane/ethyl acetate (3:1); R<sub>f</sub> ≈ 0,40. After completion of the reaction, the reaction mixture was poured in sat. NH<sub>4</sub>Cl, then Et<sub>2</sub>O was added. The phases were separated and the aqueous phase extracted three times with Et<sub>2</sub>O. The organic layer was washed with brine until the aqueous phase reached pH ~ 7. The combined organic phase was dried over MgSO<sub>4</sub>, concentrated and used without further purification.

Yield: 1,23g (98%)

**<sup>1</sup>H NMR** (250 MHz, CDCl<sub>3</sub>) δ [ppm] 3.77 – 3.64 (m, 1H<sub>a</sub>), 3.61 – 3.44 (m, 1H<sub>b</sub>), 3.17 – 3.07 (m, 2H<sub>c</sub>), 2.78 (t, 1H<sub>d</sub>), 2.62 – 2.55 (m, 2H<sub>e</sub>), 2.22 (t, 4H<sub>f</sub>), 1.57 – 1.41 (m, 8H<sub>g</sub>), 1.29 – 1.16 (m, 22H<sub>h</sub>), 0.85 (t, 3H<sub>i</sub>).

d. *1,3-bis(tricosa-10,12-diynyoxy)propan-2-ol (5):*

The coupling of the second tricosa-10,12-diyn-1-ol strand to the molecule was preformed with the similar procedure as for b).

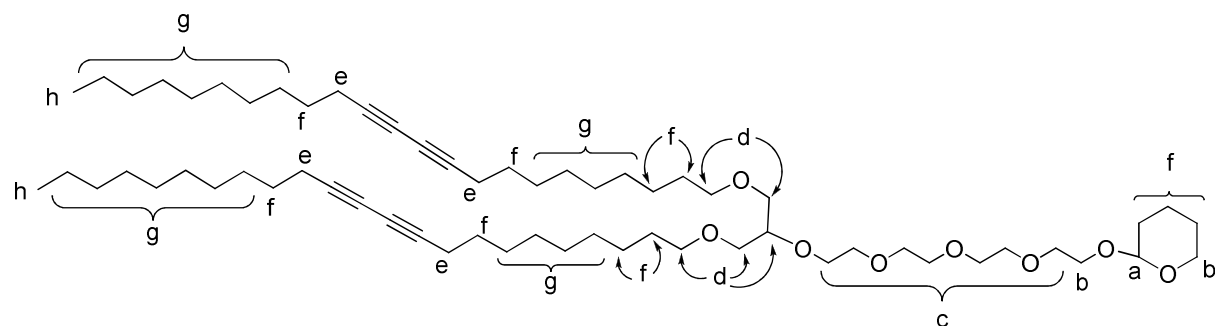
Materials: 1,23g (3,16mmol) of **1**  
 1,16g (3,48mmol) of **4**  
 ~ 30 $\mu$ l (0,22mmol) of boron trifluoride diethyl etherate  
 in 40ml dry dichloromethane.

Purification via column chromatography. Eluents: hexane/ethyl acetate (1:1);  $R_f \approx 0,65$ .

Yield: 1,21g (55%)

**<sup>1</sup>H NMR** (250 MHz, CDCl<sub>3</sub>)  $\delta$  [ppm] 3.87 (m, 1H<sub>a</sub>), 3.65 (s, 1H<sub>b</sub>), 3.52 – 3.34 (m, 8H<sub>c</sub>), 2.22 (t, 8H<sub>d</sub>), 1.57 – 1.41 (m, 16H<sub>e</sub>), 1.29 – 1.16 (m, 44H<sub>f</sub>), 0.85 (t, 6H<sub>g</sub>).

e. *1,3-bis(tricosa-10,12-diynyloxy)-glycerol-2-tetraethylene glycol, THP protected (**6**):*



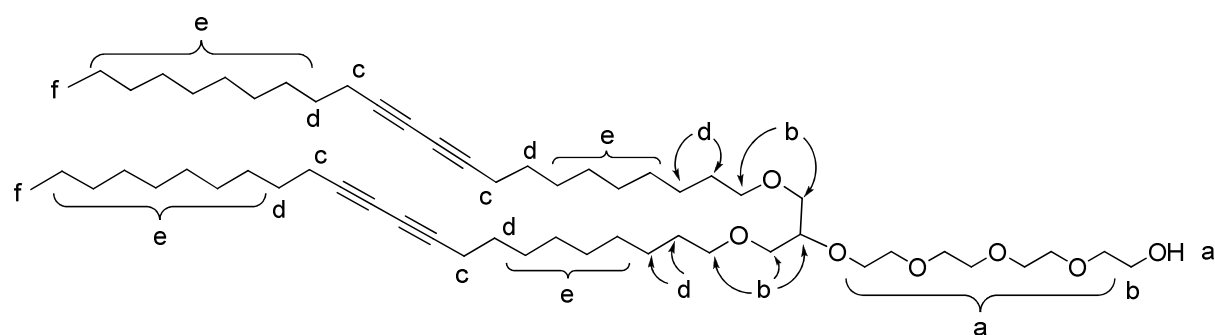
In a 100ml three necked round bottomed flask, a solution of 0,50g (0,70mmol) of **5** in 20ml dry THF was prepared under argon. 17mg (0,71mmol) sodium hydride were added to the mixture and allowed to react for one hour under stirring at room temperature. A solution of 0,83g (2,4mmol) of 1-bromo-tetraethylene glycol, THP protected (**12**) (see following synthesis procedures) in 20ml dry THF was added dropwise by a dropping funnel to the mixture and was left stirring overnight. The reaction was monitored via TLC. Eluents: hexane/ethyl acetate (1:1);  $R_f \approx 0,65$ . As a side product of the reaction, a small fraction of unprotected 1,3-bis(tricosa-10,12-diynyloxy)-glycerol-2-tetraethylene glycol was also fund, and kept with the main fraction for the further deprotection in the next step. After completion of the reaction, some drops of water were carefully added to the reaction mixture to neutralize the non-reacted NaH. The NaBr in solution was separated from the mixture by a concentration – dilution (with THF) – centrifugation (9000rpm, 20min) procedure repeated at least three times, until no sedimentation of salt could be found after centrifugation. After the last centrifugation the samples were merged and dried over

$\text{MgSO}_4$ . The solution was concentrated and the product purified with flash chromatography.

Yield: 270mg (40%)

**$^1\text{H NMR}$**  (250 MHz,  $\text{CDCl}_3$ )  $\delta$  [ppm] 4.61 (t, 1H $a$ ), 3.91 – 3.78 (m, 4H $b$ ), 3.76 – 3.61 (m, 14H $c$ ), 3.54 – 3.35 (m, 9H $d$ ), 2.22 (t, 8H $e$ ), 1.90 – 1.43 (m, 22H $f$ ), 1.42 – 1.14 (m, 44H $g$ ), 0.86 (t, 6H $h$ ).

f. *1,3-bis(tricosa-10,12-diynyloxy)-glycerol-2-tetraethylene glycol (7):*

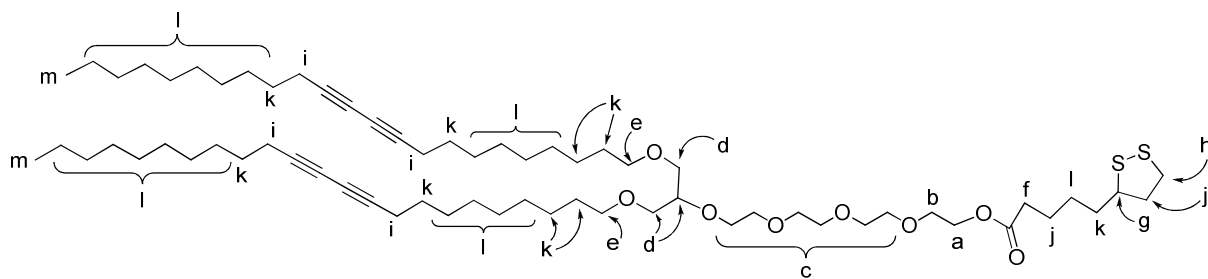


270mg (0,27mmol) of **6** was introduced in a 50ml round bottomed flask and dissolved in DCM. 0,6ml of HCl 37% were added and the reaction mixture was left stirring overnight. Small amounts of  $\text{NaHCO}_3$  were added to the mixture in order to neutralize the excess HCl. The solution was filtered over a frit and the solvent evaporated. The product was used without further purifications.

Yield: 240mg (99%)

**$^1\text{H NMR}$**  (250 MHz,  $\text{CDCl}_3$ )  $\delta$  [ppm] 3.78 – 3.54 (m, 15H $a$ ), 3.51 – 3.33 (m, 11H $b$ ), 2.22 (t, 8H $c$ ), 1.67 – 1.41 (m, 16H $d$ ), 1.41 – 1.11 (m, 44H $e$ ), 0.86 (t, 6H $f$ ).

g. *1,3-bis(tricosa-10,12-diynyloxy)-glycerol-2-(tetraethylene glycol-[D,L- $\alpha$  lipoic acid ester]) (8)* [87]:



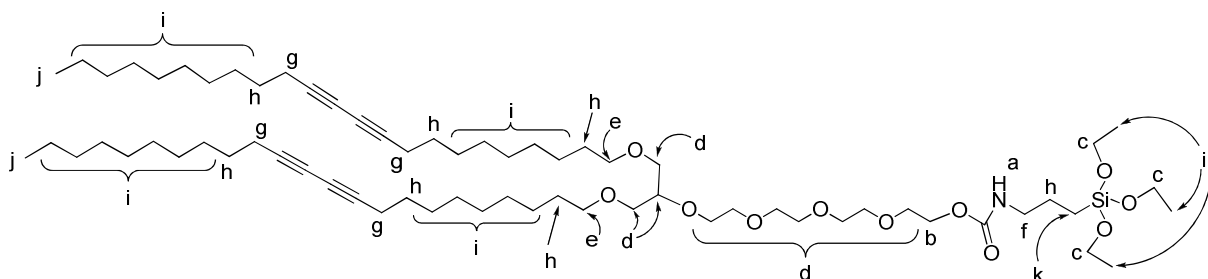
In a 250ml one neck round bottomed flask, 276mg (1,34mmol) D,L- $\alpha$  lipoic acid and 272mg (1,34mmol) N,N'-dicyclohexylcarbodiimide (DCC) were dissolved in 70ml dry DCM under argon atmosphere. The mixture was stirred at room temperature for 30 minutes before the step-wise addition of 240mg (0,26mmol) of 7. After another 30 minutes stirring, 30mg (0,26mmol) of 4-(dimethylamino) pyridine (DMAP) were added and the reaction left stirring overnight. The reaction was monitored via TLC. Eluents: hexane/ethyl acetate (1:2);  $R_f \approx 0,85$ . After completion of the reaction, the mixture was diluted with 150ml DCM and successively washed with a solution of Na<sub>2</sub>CO<sub>3</sub> and water. The organic phase was then dried over MgSO<sub>4</sub> and the solvent evaporated. The purification was done with flash chromatography.

Yield: 120mg (45%)

**<sup>1</sup>H NMR** (250 MHz, CDCl<sub>3</sub>)  $\delta$  [ppm] 4.19 (t, 2H<sub>a</sub>), 3.72 (t, 2H<sub>b</sub>), 3.68 – 3.57 (m, 12H<sub>c</sub>), 3.54 – 3.42 (m, 5H<sub>d</sub>), 3.39 (t, 4H<sub>e</sub>), 3.22 – 3.00 (m, 2H<sub>f</sub>), 2.43 (m, 1H<sub>g</sub>), 2.32 (t, 2H<sub>h</sub>), 2.20 (t, 8H<sub>i</sub>), 2.00 – 1.79 (m, 4H<sub>j</sub>), 1.72 – 1.42 (m, 18H<sub>k</sub>), 1.22 (m, 46H<sub>l</sub>), 0.83 (t, 6H<sub>m</sub>).

See NMR and Mass spectra in appendix.

h. *1,3-bis(tricosa-10,12-diynyloxy)-glycerol-2-(tetraethylene glycol-[3-(triethoxysilyl) propylcarbamate]) (9)* [88]:



In a 50ml three necked round bottomed flask equipped with an argon inlet and a reflux condenser, 100mg (0,11mmol) of **7**, 33mg (0,13mmol) of (3-isocyanatopropyl) triethoxysilane, 5 drops of triethylamine were introduced in 25ml dry THF. The mixture was heated to reflux for 48 hours under argon atmosphere. After completion of the reaction, the mixture was concentrated and purified with flash chromatography. The silica gel used for the chromatography was first passivated 10 minutes with a 5% solution of hexamethyldisilazane in the eluent. Eluents: hexane/ethyl acetate (1:2);  $R_f \cong 0,75$ .

Yield: 80mg (63%)

**<sup>1</sup>H NMR** (250 MHz, CDCl<sub>3</sub>) δ [ppm] 4.95 (s, 1H<sub>a</sub>), 4.12 (dt, 2H<sub>b</sub>), 3.80 (qd, 6H<sub>c</sub>), 3.69 – 3.44 (m, 19H<sub>d</sub>), 3.40 (t, 4H<sub>e</sub>), 3.15 (dt, 2H<sub>f</sub>), 2.22 (t, 8H<sub>g</sub>), 1.64 – 1.41 (m, 14H<sub>h</sub>), 1.41 – 1.11 (m, 57H<sub>i</sub>), 0.86 (t, 6H<sub>j</sub>), 0.65 – 0.56 (m, 2H<sub>k</sub>).

See NMR and Mass spectra in appendix.

#### *4.2.2. Synthesis of the spacer part*

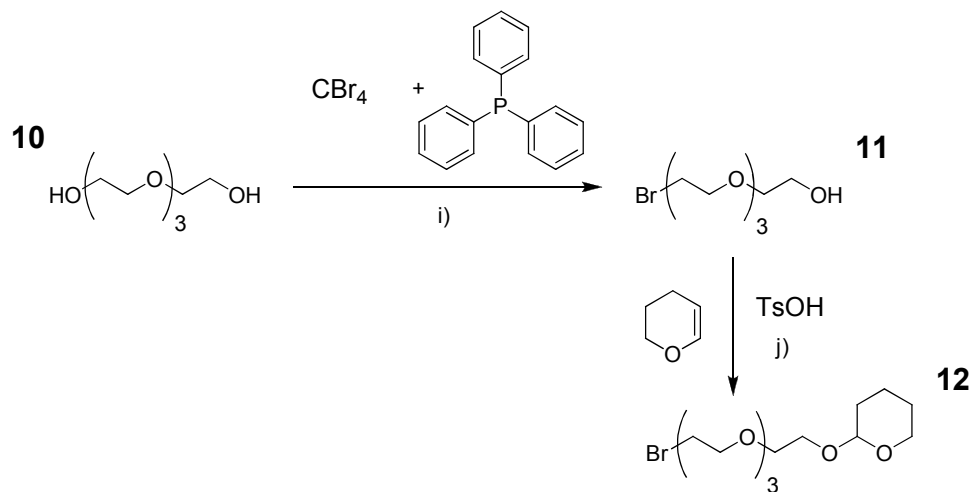
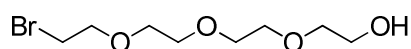


**Figure 4.2:** Synthesis scheme for the spacer part of the lipid

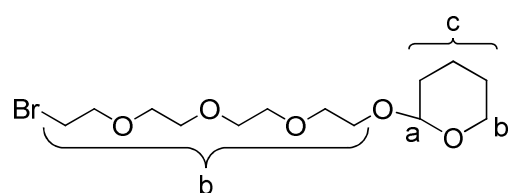
i. *1-bromotetraethylene glycol (11)* [89]:



*Appel Reaction:*

A solution of 10g (51mmol) tetraethylene glycol and 18,8g (56,6mmol) tetrabromomethane in 50ml DCM was prepared in a 250ml three necked round bottomed flask, equipped with a mechanical stirrer and cooled down to 0°C. 14,9g (57mmol) triphenyl phosphine were added stepwise over 30 minutes. The mixture was allowed to warm up to room temperature and stirred overnight. The DCM was then removed under vacuum and the remaining oil taken up in hexane. The hexane extracts were collected and concentrated to oil, used in the further step without purification.

Yield: 12,50g (95%)

j. *1-bromo-12-tetrahydro-2H-pyran tetraethylene glycol (12)*<sup>[90]</sup>:

370mg (1,9mmol) *p*-toluenesulfonic acid monohydrate was added to a solution of 12,5g (48mmol) of **11** and 7,37g (87mmol) of 3,4-dihydro-2*H*-pyran in 200ml THF at room temperature. The mixture was stirred for 2 hours and the solvent was removed under reduced pressure. The residue was separated by flash chromatography. Eluents: hexane/ethyl acetate (1:2);  $R_f \cong 0,47$ .

Yield: 12,54g (76%)

**<sup>1</sup>H NMR** (250 MHz, CDCl<sub>3</sub>) δ [ppm] 4.61 (s, 1H<sub>a</sub>), 3.91 – 3.39 (m, 18H<sub>b</sub>), 1.90 – 1.38 (m, 6H<sub>c</sub>).

*4.2.3. Discussion of the synthesis way*

Different ways of synthesis have been tried, mostly concerning the coupling of the hydrophobic chains to the glycerol part. Various reports in the literature<sup>[74, 85]</sup> cite the possibility to couple at the same time both alkyl chains to a mono-protected glycerol. Although the method presented by Pfeiffer et al.<sup>[74]</sup> was designated to produce 2,3-diacyl-

*sn*-glycerols it has been modified by Lee et al.<sup>[85]</sup> to end up with the ether-linked lipid. The preparation of the triphenyl-protected glycerol is described in Figure 4.3.

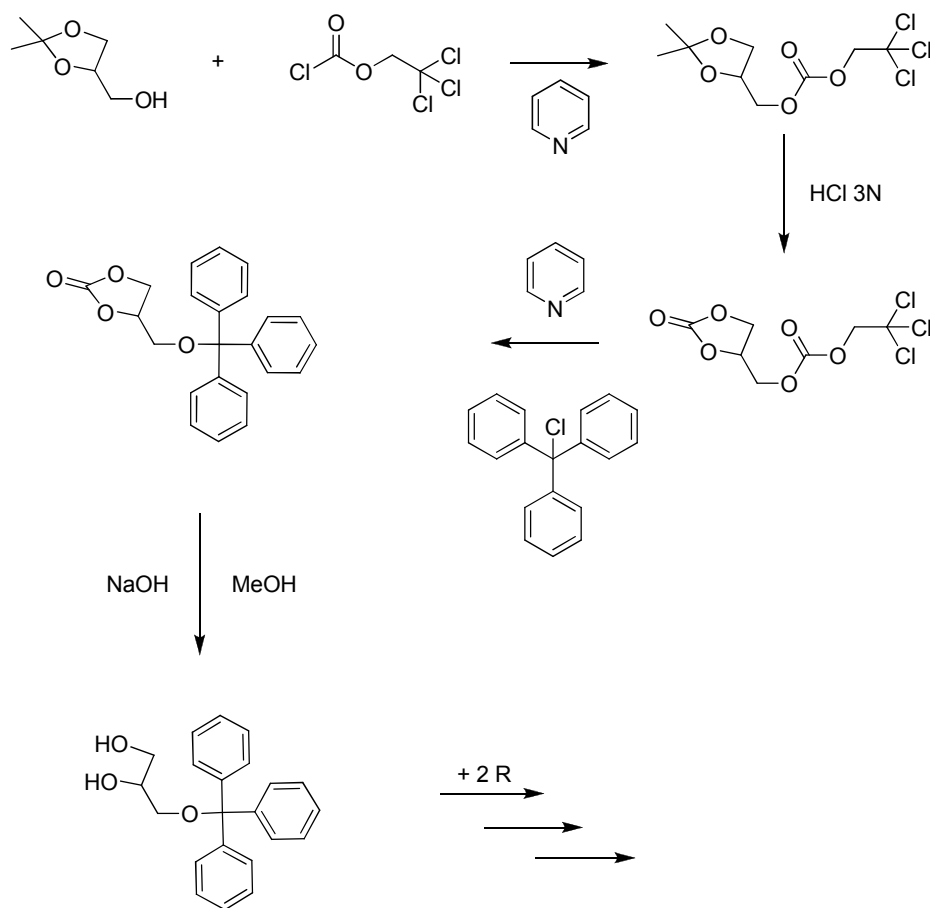


**Figure 4.3: Preparation of 3-*O*-tritylglycerol from 1,2-isopropylideneglycerol<sup>[74]</sup>.**

The intensive preparation steps of the 3-*O*-tritylglycerol are not the only reason why this approach has not been used. We experienced in other synthesis for different studies that the simultaneous ether coupling of two alkyl chains on vicinal diols has very low yields. This is due to the apparition of side-products, the most common would be the mono-ether, resulting from the loss of reactivity induced by the sterical hindrance of the side groups after the first addition.

Another route, also known as the *Sharpless asymmetric epoxidation*, quite similar to the one used in this study should be preferred if the product is thought to be produced in larger quantities. The expensive but “convenient” glycidyl tosylate can be replaced by allyl alcohol, where the double bond is selectively oxidized to an epoxide intermediate which is directly reacted with the prepared alcoholate as shown in Figure 4.4. After closing the

epoxide ring a second time, the alcoholate can be added another time, from the other side, producing the 1,3-O-bis alkyl glycerol.<sup>[91]</sup> The mechanism of the Sharpless epoxidation is believed to involve attack on the substrate by a compound formed from the titanium – tartrate complex that also contains the substrate and the peroxide.<sup>[92, 93]</sup> Furthermore, by using optically active tartrate, the reaction is stereospecific and either enantiomer can be prepared, if the second alcoholate attached differs from the first. This route is a reliable way to produce bigger amounts of products at lower costs.

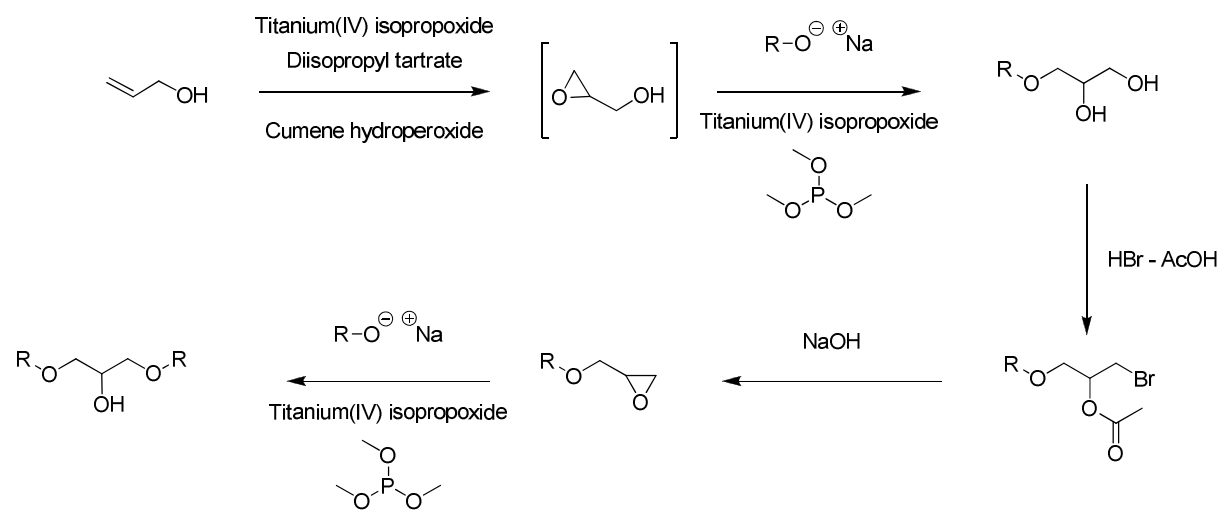


**Figure 4.4: Preparation of 1,3-O-bis alkyl glycerol from allyl alcohol**

### 4.3. Ester linked molecules

#### 4.3.1. Double stranded anchor lipids

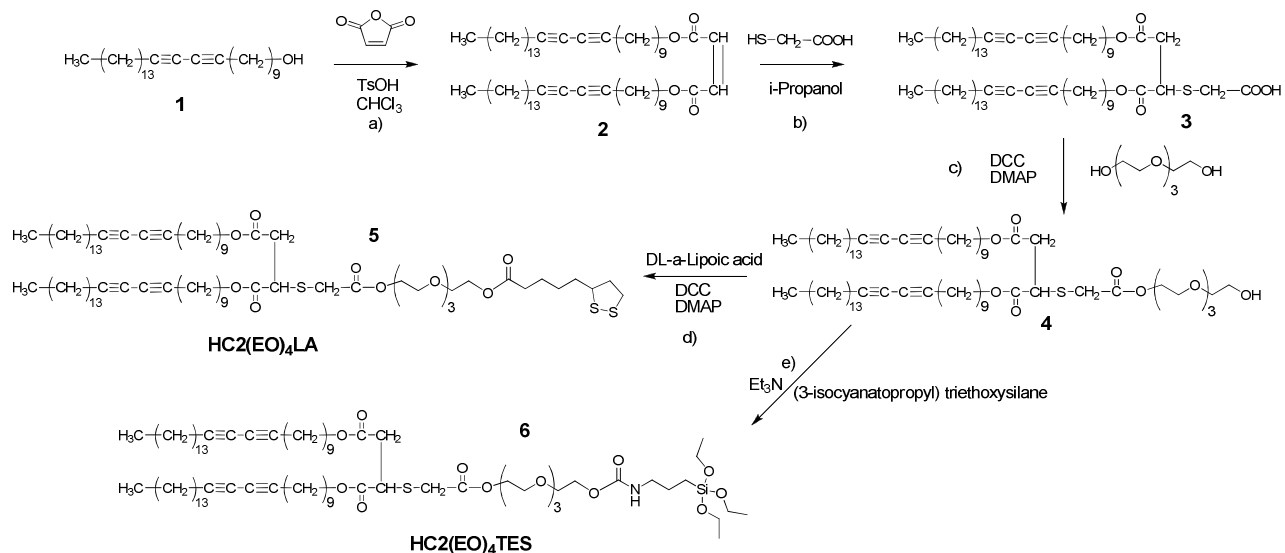
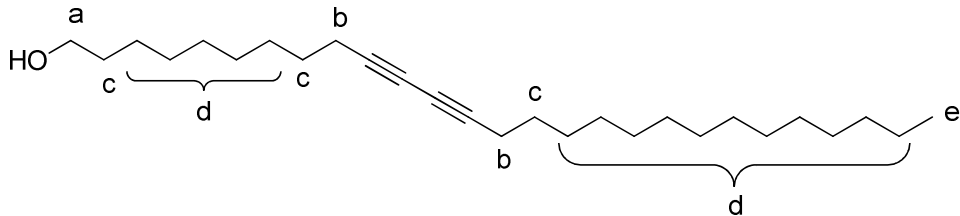


**Figure 4.5:** Synthesis scheme for HC(EO)<sub>4</sub>LA (**5**) and HC(EO)<sub>4</sub>TES (**6**)

*Heptacosa-10,12-diyn-1-ol (**13**):*



Heptacosa-10,12-diyn-1-ol used in this part has been kindly provided by Prof. Ringsdorf, but can be prepared by following procedure (see Figure 4.6).<sup>[94]</sup>

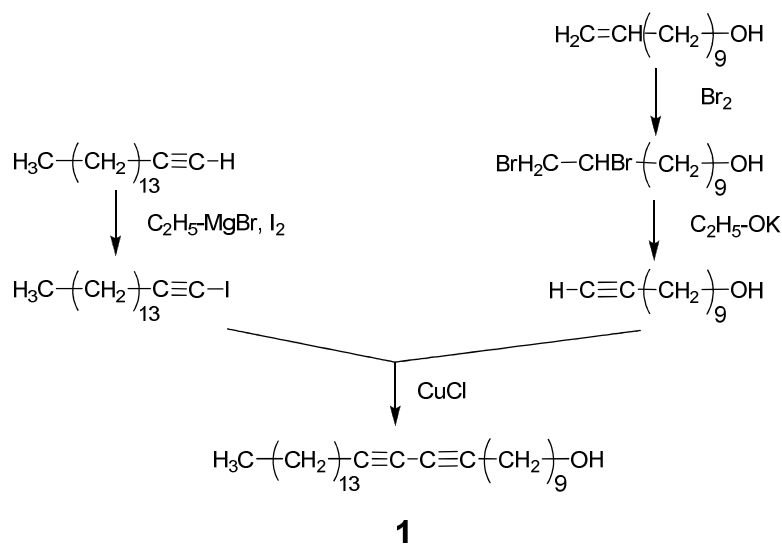
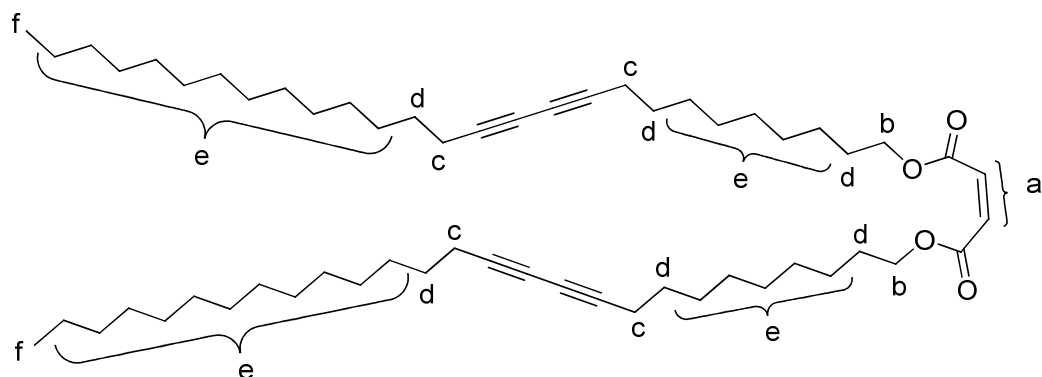


**Figure 4.6: Synthesis scheme for Heptacosa-10,12-diyn-1-ol (1)**

Starting from hexadec-1-yne, reacting with ethylmagnesium bromide in diethyl ether, followed by the addition of iodine, 1-iodo-hexadec-1-yne can be obtained. Undec-10-ene-1-ol is obtained by the bromination of undec-10-ene-1-ol followed by the elimination with potassium ethanolate in ethanol. The both components were coupled via the Cadiot-Chodkiewiecz coupling reaction involving copper (I) ions.

**<sup>1</sup>H NMR** (250 MHz,  $\text{CDCl}_3$ )  $\delta$  [ppm] 3.62 (t, 2H $a$ ), 2.22 (t, 4H $b$ ), 1.61 – 1.38 (m, 6H $c$ ), 1.33 – 1.18 (m, 32H $d$ ), 0.86 (t, 3H $e$ ). The alcohol proton form  $-\text{CH}_2-\text{OH}$  could not be seen.

a) *Maleic acid-bis(heptacosa-10,12-diynyl)-ester (14):*



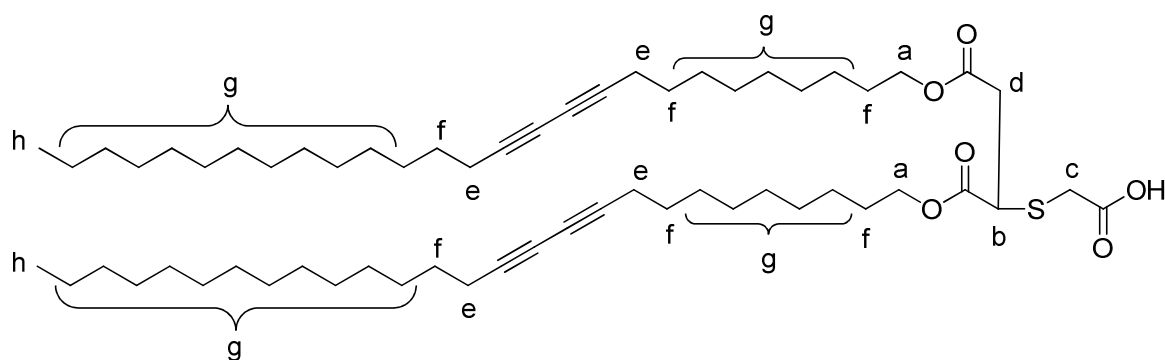
20g (51,5mmol) heptacosa-10,12-diyn-1-ol (**13**) were added to a solution of 2,4g (25,8mmol) maleic anhydride and 1,3g (7,5mmol) p-toluenesulfonic acid in 150ml dry

chloroform. The reaction mixture was heated to reflux 24 hours with a water separator. After completion of the reaction, the mixture was washed once with water, dried over  $\text{Na}_2\text{SO}_4$  and concentrated. The product was purified through recrystallisation in acetone and flash chromatography. Eluents: petrol ether/ethyl acetate (95:5).

Yield: 14g (58%)

**$^1\text{H NMR}$**  (250 MHz,  $\text{CDCl}_3$ )  $\delta$  [ppm] 6.23 (s, 2Ha), 4.18 (t, 4Hb), 2.22 (t, 8Hc), 1.61 – 1.38 (m, 12Hd), 1.33 – 1.18 (m, 64He), 0.86 (t, 6Hf).

b) *Succinic acid-2-thioglycolic acid-1,4-bis(heptacosa-10,12-diynyl)-ester (15)*<sup>[95]</sup>:



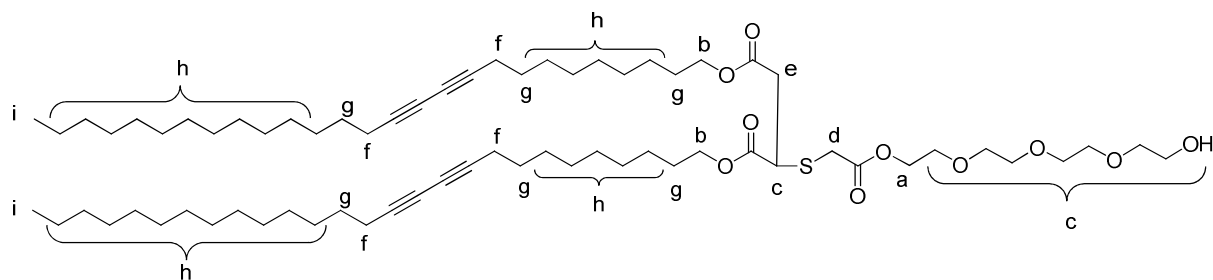
0,65g (7,06mmol) thioglycolic acid and 13ml tetramethylethylenediamine were added to a solution of 3g (6,44mmol) of **14** in 50ml dry THF. The reaction mixture was then shortly heated to reflux and consequently left stirring for two days at room temperature. After completion of the reaction, the solvent was evaporated, the remaining solid dissolved in ethyl acetate and acidified with 2N  $\text{H}_2\text{SO}_4$ . The mixture was consequently washed three times with water, the organic phase dried over  $\text{Na}_2\text{SO}_4$  and concentrated. The product was purified with flash chromatography.

Eluents: chloroform/methanol (20:1).

Yield: 2g (56%)

**$^1\text{H NMR}$**  (250 MHz,  $\text{CDCl}_3$ )  $\delta$  [ppm] 4.18 – 3.92 (m, 4Ha), 3.90 – 3.75 (dt, 1Hb), 3.54 – 3.33 (m, 2Hc), 3.03 – 2.65 (m, 2Hd), 2.22 (t, 8He), 1.64 – 1.42 (m, 12Hf), 1.41 – 1.12 (m, 64Hg), 0.86 (t, 6Hh).

c) Succinic acid-2-(thioglycolic acid-[tetraethylene glycol ester])-1,4-bis(heptacosa-10,12-diynyl)-ester (**16**) :

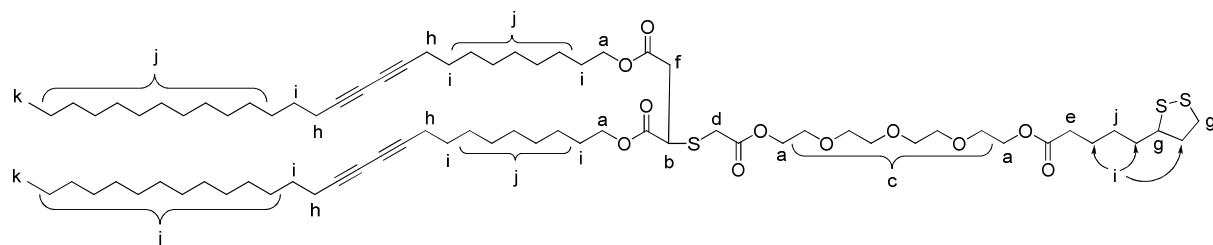


In a 100ml one neck round bottomed flask, 0,50g (0,52mmol) of **15** and 110mg (0,52mmol) DCC were dissolved in 25ml dry DCM. The mixture was stirred at room temperature for 30 minutes before the step-wise addition of 1,0g (5,2mmol) of tetraethylene glycol. After another half an hour stirring, ~10mg (0,01mmol) of DMAP was added and the reaction left stirring overnight. The reaction was monitored via TLC. Eluents: hexane/ethyl acetate (1:2);  $R_f \approx 0,40$ . After completion of the reaction, the mixture was diluted with 150ml DCM and successively washed with a solution of  $\text{Na}_2\text{CO}_3$  and water. The organic phase was then dried over  $\text{MgSO}_4$  and the solvent evaporated. The purification was done with flash chromatography.

Yield: 230mg (40%)

**<sup>1</sup>H NMR** (250 MHz,  $\text{CDCl}_3$ )  $\delta$  [ppm] 4.33 – 4.22 (m, 2H*a*), 4.17 – 3.92 (m, 4H*b*), 3.85 – 3.54 (m, 16H*c*), 3.54 – 3.33 (m, 2H*d*), 3.03 – 2.65 (m, 2H*e*), 2.22 (t, 8H*f*), 1.64 – 1.42 (m, 12H*g*), 1.41 – 1.12 (m, 64H*h*), 0.86 (t, 6H*i*).

d) Succinic acid-2-(thioglycolic acid-[tetraethylene glycol ester]-[D,L- $\alpha$ -lipoic acid ester])-1,4-bis(heptacosa-10,12-diynyl)-ester (**17**) :



The ester coupling of the D,L- $\alpha$  lipoic acid to the molecule was preformed with the similar procedure as in c).

Materials: 115mg (0,10mmol) of **16**

105mg (0,50mmol) of D,L- $\alpha$  lipoic acid

105mg (0,50mmol) of DCC

$\sim$  10mg (0,01mmol) of DMAP

in 20ml dry DCM.

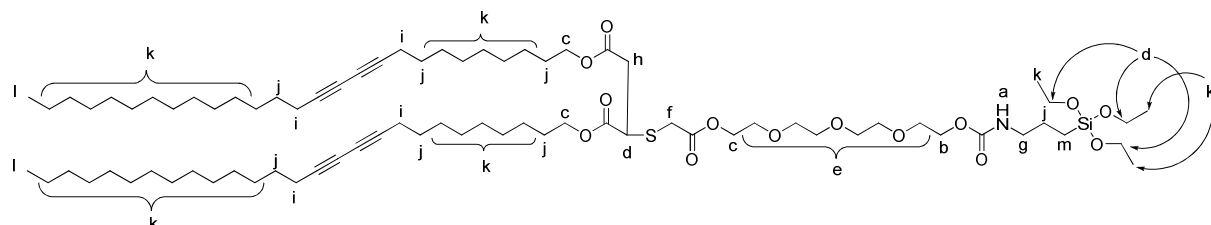
Purification via column chromatography. Eluents: hexane/ethyl acetate (1:2);  $R_f \cong 0,80$ .

Yield: 190mg (80%)

**<sup>1</sup>H NMR** (250 MHz, CDCl<sub>3</sub>)  $\delta$  [ppm] 4.32 – 3.99 (m, 8H<sub>a</sub>), 3.84 – 3.76 (dd, 1H<sub>b</sub>), 3.74 – 3.50 (m, 12H<sub>c</sub>), 3.38 (d, 2H<sub>d</sub>), 3.13 (dd, 2H<sub>e</sub>), 2.97 – 2.64 (m, 2H<sub>f</sub>), 2.53 – 2.26 (m, 3H<sub>g</sub>), 2.22 (t, 8H<sub>h</sub>), 1.98 – 1.53 (m, 18H<sub>i</sub>), 1.54 – 1.09 (m, 6H<sub>j</sub>), 0.84 (t, 6H<sub>k</sub>).

See NMR and Mass spectra in appendix.

e) Succinic acid-2-(thioglycolic acid-[tetraethylene glycol ester-[3-(triethoxysilyl)propylcarbamate]]-1,4-bis(heptacosa-10,12-diynyl)-ester (**18**) :



The functionalization of **16** with (3-isocyanatopropyl) triethoxysilane has been realized with the same procedure as the one described under h) for the ether linked molecules.

Materials: 115mg (0,10mmol) of **16**

29mg (0,50mmol) of (3-isocyanatopropyl) triethoxysilane

3 drops of triethylamine

in 20ml dry THF.

The purification was done via a passivated column chromatography as for h).

Eluents: hexane/ethyl acetate (1:2);  $R_f \cong 0,75$ .

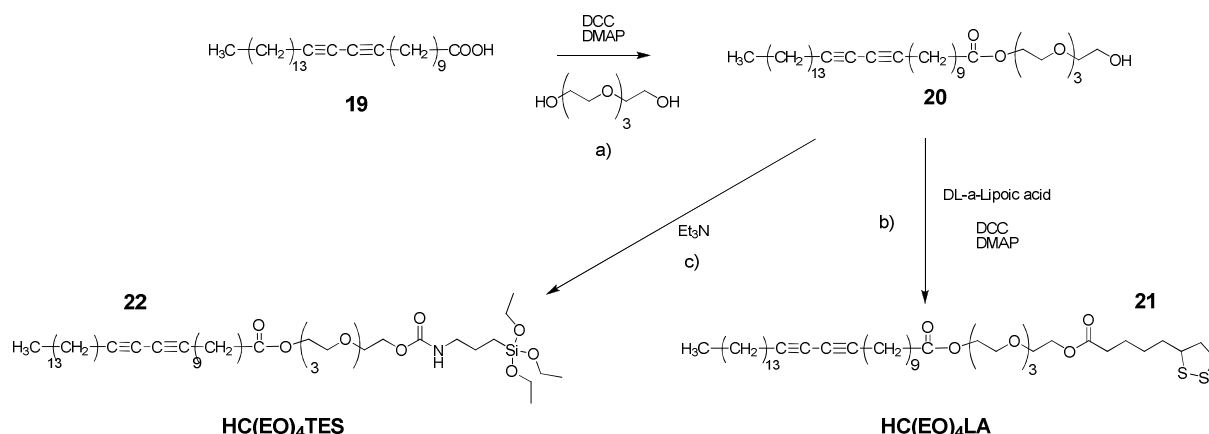
Yield: 40g (30%)

**<sup>1</sup>H NMR** (250 MHz, CDCl<sub>3</sub>) δ [ppm] 4.85 (s, 1H<sub>a</sub>), 4.30 – 4.15 (m, 2H<sub>b</sub>), 4.15 – 4.00 (m, 6H<sub>c</sub>), 3.80 (m, 7H<sub>d</sub>), 3.73 – 3.59 (m, 12H<sub>e</sub>), 3.59 – 3.33 (m, 2H<sub>f</sub>), 3.15 (dd, 2H<sub>g</sub>), 3.02 – 2.64 (m, 2H<sub>h</sub>), 2.22 (t, 8H<sub>i</sub>), 1.71 – 1.38 (m, 14H<sub>j</sub>), 1.32 – 1.13 (m, 66H<sub>k</sub>), 0.85 (t, 6H<sub>l</sub>), 0.67 – 0.54 (m, 2H<sub>m</sub>).

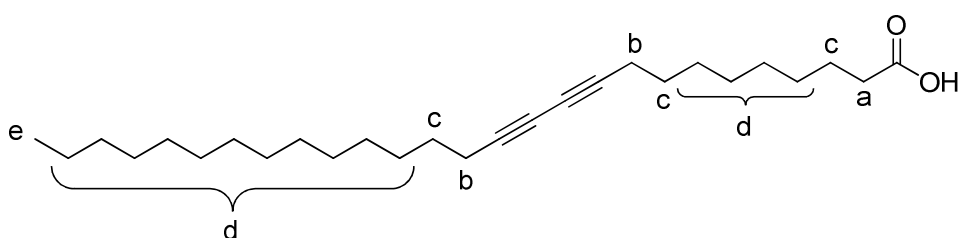
See NMR and Mass spectra in appendix.

The NMR spectrum of **18** shows rests of (3-isocyanatopropyl) triethoxysilane with the target molecule. Due to the delicate cleaning procedure, in order to avoid the hydrolysis of the triethoxysilane group during chromatography, we chose to use the product as presented. Furthermore, the LB method of deposition reduced also the amount of impurities in the film, since (3-isocyanatopropyl) triethoxysilane does not remain at the air-water interface.

#### 4.3.2. Single stranded anchor lipids



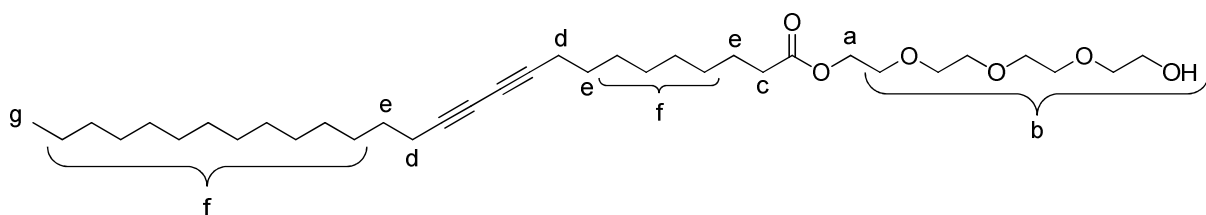
*Heptacosa-10,12-diynoic acid (**19**)<sup>[94]</sup>:*



As in the previous part, the heptacosa-10,12-diynoic acid used has been kindly provided by Prof. Ringsdorf, and can be prepared with the same procedure as in part 4.3.1, by replacing undec-10-ene-1ol with undec-10-eneoic acid.

**<sup>1</sup>H NMR** (250 MHz, CDCl<sub>3</sub>) δ [ppm] 2.33 (t, 2H<sub>a</sub>), 2.22 (t, 4H<sub>b</sub>), 1.49 (s, 6H<sub>c</sub>), 1.26 (d, 30H<sub>d</sub>), 0.84 (t, 3H<sub>e</sub>). The acid proton form –COOH could not be seen.

a) *Heptacosa-10,12-diynoic acid-tetraethylene glycol ester (20):*

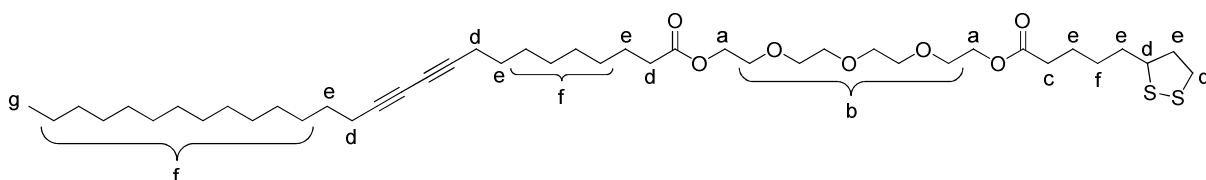


In a 50ml one neck round bottomed flask, 1,50g (3,7mmol) of **19** and 0,78g (3,70mmol) DCC were dissolved in 20ml dry DCM. The mixture was stirred at room temperature for about half an hour before the step-wise addition of 7,18g (48mmol) of tetraethylene glycol. After another half an hour stirring, ~80mg (0,70mmol) of DMAP was added and the reaction left stirring overnight. The reaction was monitored via TLC. Eluents: hexane/ethyl acetate (1:2); R<sub>f</sub> ≈ 0,27. After completion of the reaction, the mixture was diluted with 50ml DCM and successively washed with a solution of Na<sub>2</sub>CO<sub>3</sub> and water. The organic phase was then dried over MgSO<sub>4</sub> and the solvent evaporated. The purification was done with flash chromatography.

Yield: 1,10g (51%)

**<sup>1</sup>H NMR** (250 MHz, CDCl<sub>3</sub>) δ [ppm] 4.21 (t, 2H<sub>a</sub>), 3.77 – 3.37 (m, 15H<sub>b</sub>), 2.30 (t, 2H<sub>c</sub>), 2.22 (t, 4H<sub>d</sub>), 1.75 – 1.42 (m, 6H<sub>e</sub>), 1.40 – 1.17 (m, 30H<sub>f</sub>), 0.85 (t, 3H<sub>g</sub>).

b) *Heptacosa-10,12-diynoic acid-tetraethylene glycol ester-(D,L-α lipoic acid ester) (21):*



The ester coupling of the D,L- $\alpha$  lipoic acid with **20** was preformed with the similar procedure as in a).

Materials: 350mg (0,60mmol) of **2**  
630mg (3,0 mmol) of D,L- $\alpha$  lipoic acid  
630mg (3,0mmol) of DCC  
~ 60mg (0,50mmol) of DMAP  
in 20ml dry DCM.

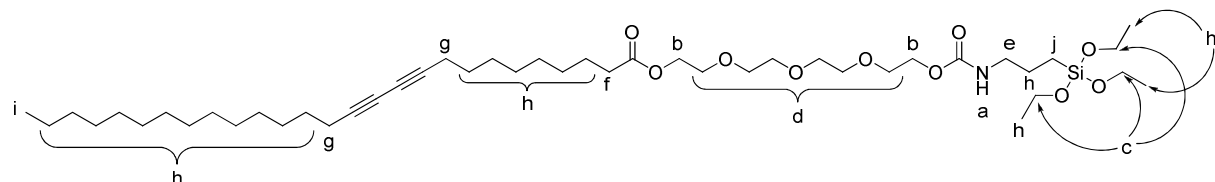
Purification via column chromatography. Eluents: hexane/ethyl acetate (1:1);  $R_f \approx 0,50$ .

Yield: 350mg (76%)

**<sup>1</sup>H NMR** (250 MHz, CDCl<sub>3</sub>) δ [ppm] 4.26 – 4.14 (m, 4H<sub>a</sub>), 3.85 – 3.49 (m, 12H<sub>b</sub>), 3.13 (dd, 2H<sub>c</sub>), 2.53 – 2.16 (m, 9H<sub>d</sub>), 2.08 – 1.41 (m, 12H<sub>e</sub>), 1.41 – 1.07 (m, 30H<sub>f</sub>), 0.84 (t, 3H<sub>g</sub>).

See NMR and Mass spectra in appendix.

c) *Heptacosa-10,12-diynoic acid-tetraethylene glycol ester-[3-(triethoxysilyl)propylcarbamate]* (**22**):



The functionalization of **20** with (3-isocyanatopropyl) triethoxysilane has been realized with the same procedure as h) for the ether linked molecules.

Materials: 350mg (0,60mmol) of **20**  
178mg (0,74mmol) of (3-isocyanatopropyl) triethoxysilane  
3 drops of triethylamine  
in 30ml dry THF.

The purification was done via a passivated column chromatography as for h).

Eluents: hexane/ethyl acetate (1:2);  $R_f \cong 0,75$ .

Yield: 370mg (75%)

**<sup>1</sup>H NMR** (250 MHz, CDCl<sub>3</sub>) δ [ppm] 4.95 (s, 1H<sub>a</sub>), 4.28 – 4.11 (m, 4H<sub>b</sub>), 3.79 (dd, 6H<sub>c</sub>), 3.72 – 3.57 (m, 12H<sub>d</sub>), 3.15 (dd, 2H<sub>e</sub>), 2.30 (t, 2H<sub>f</sub>), 2.22 (t, 4H<sub>g</sub>), 1.70 – 1.08 (m, 47H<sub>h</sub>), 0.86 (t, 3H<sub>i</sub>), 0.60 (t, 2H<sub>j</sub>).

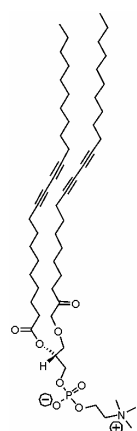
See NMR and Mass spectra in appendix.

## 5. Thermotropic behavior of polymerizable tBLM

Diacetylenic lipids have to assemble in a crystalline lattice in order to polymerize. Upon heating, they undergo a phase transition from a liquid ordered to a fluid phase, disturbing the diacetylene organization between the lipids and thus inhibiting the topochemical reaction. The thermotropic properties of the synthesized anchor lipids were therefore investigated with DSC as bulk product and as a monolayer film with optical waveguide spectroscopy.

### 5.1. DSC experiments

Calorimetric studies of the polymerizable diacetylene lipid 1,2-bis(10,12-tricosadiynoyl)-*sn*-glycero-3-phosphocholine (DC<sub>23</sub>PC, see Figure 5.1) were reported in the literature.<sup>[96-98]</sup>



The main aim of these studies was to determine the effects of phase transitions on the bilayer structure. Depending on the type of aggregates DC<sub>23</sub>PC forms in water, i.e. multilamellar (MLV) or small unilamellar vesicles (SUV) suspensions, conversion to either gel phase or tubular structures by cooling under the phase transition temperature was observed. DSC measurements of the phospholipid showed transition temperatures ranging from 36°C – 40°C for the hydrated MLVs or SUVs to 43,1°C for the dry lipids.

**Figure 5.1: Chemical structure of DC<sub>23</sub>PC**

The synthesized TD2(EO)<sub>4</sub>TES and TD2(EO)<sub>4</sub>LA, which have similar diacetylene chain length as the DC<sub>23</sub>PC model compound, were investigated by DSC. The thermal spectra obtained are depicted in Figure 5.2. Table 5.1 gives the peak temperatures in each sample.

The probes were first cooled down to -140°C after been introduced in the furnace. Afterwards, a linear temperature ramp of +10°C/min was applied on the samples until 220°C. The enthalpy changes in the probe during these heating phases were recorded and are depicted by the red curves. Once the samples achieved the upper temperature range, they were cooled down with a rate of 10°C/min to -140°C. The enthalpy changes in the

probes are represented by the blue curves. Figure 5.2B shows a third curve in green, coming from a second heating phase with the same parameters as the first.

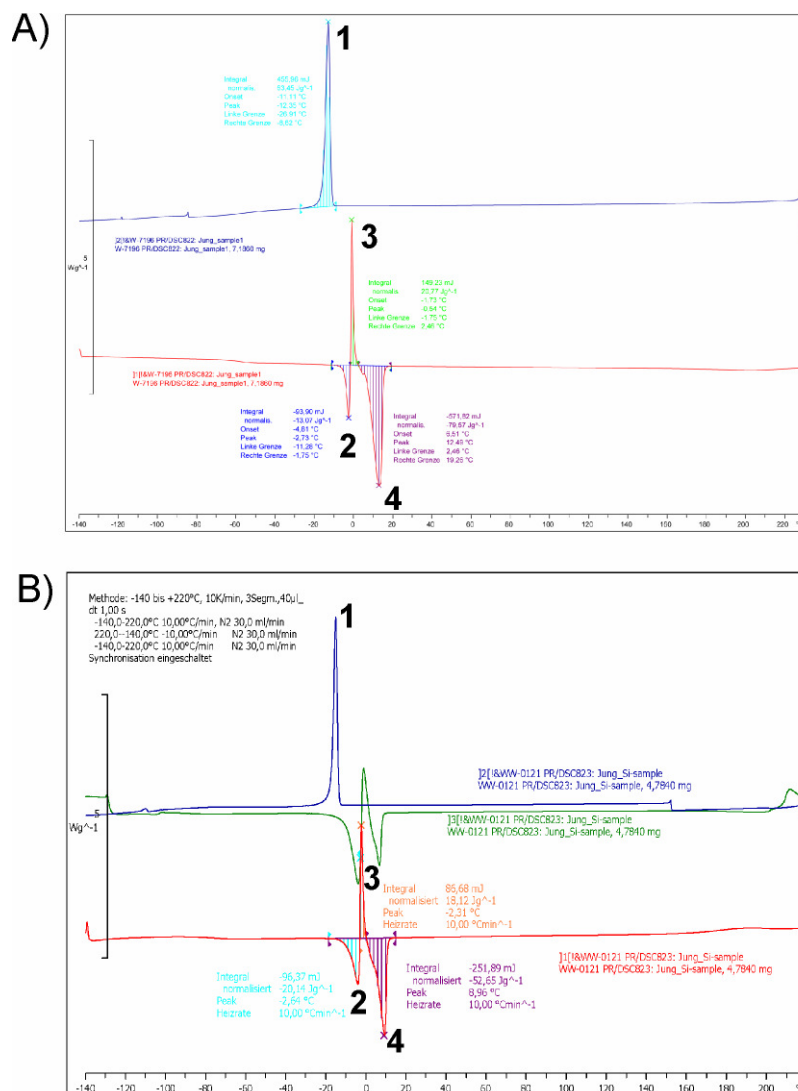


**Figure 5.2:** A) DSC of TD2(EO)<sub>4</sub>LA, B) DSC of TD2(EO)<sub>4</sub>TES.

Peaks	1	2	3	4
TD2(EO) <sub>4</sub> LA	-11,11°C	-2,73°C	-0,54°C	12,49°C
TD2(EO) <sub>4</sub> TES	-15,00°C	-4,09°C	-2,31°C	8,96°C

**Table 5.1:** Extracted peak temperature from the DSCs in Figure 5.2.

Each heating curve of the DSCs showed two endothermic peaks and one exothermic located between both. The first endothermic events, respectively at -2,73°C for TD2(EO)<sub>4</sub>LA and -4,09°C for TD2(EO)<sub>4</sub>TES were attributed to the melting of the tetraethylene oxide chains of the molecules. Pure tetraethylene oxide is melting at

temperatures between -5°C and -2°C. The following exothermic peak could not be directly addressed but is believed to be due to rearrangements of parts of the molecule after the ethylene oxide chains regained in mobility. The last endothermic peaks at 12,49°C and 8,96°C were assigned to the melting of the diacetylene chains.

The cooling curves of the DSC thermograms, only exhibit one exothermic peak, corresponding to a crystallization, although at least two were expected. It is known from literature that the freezing point of tetraethylene glycol is located around -9,4°C.<sup>[99]</sup> The crystallization temperatures of -11,11°C and -15,00°C for respectively TD2(EO)<sub>4</sub>LA and TD2(EO)<sub>4</sub>TES may suggest a concerted crystallization of both diacetylene chains and ethylene oxide together. However, this issue has not been addressed.

## **5.2. Optical waveguide spectroscopy**

The optical waveguide spectroscopic measurements were done by Christoph Hoffmann (AK. Knoll, MPIP).

After measuring the transition temperatures of the pure lipids with DSC, monomolecular layers were investigated with optical waveguide spectroscopy. Monolayers of TD2(EO)<sub>4</sub>TES were transferred by Langmuir-Blodgett film transfer at a surface pressure of 32mN/m (water subphase temperature: 9,5°C) in a liquid condensed state onto a silicon-titanium oxide waveguide. The film was allowed to dry overnight in a desiccator.

The transition temperature of the film was measured in air as described previously (see Chapter Materials & Methods, 2.9).

The graphs in Figure 5.3 show the plots of the refractive index change in the monolayer, in function of the temperature both for the transverse electric (TE) and transverse magnetic (TM) mode of zeroth order.

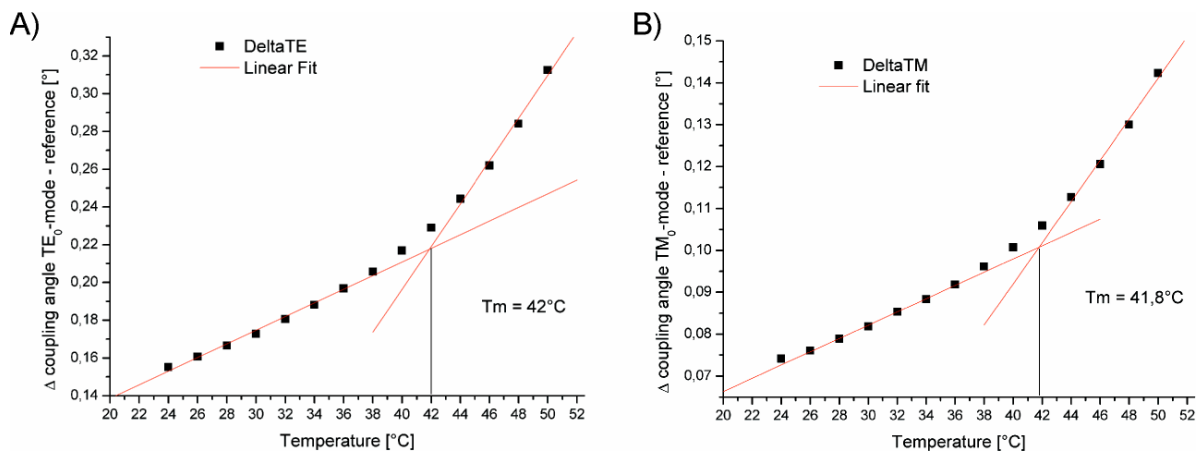


**Figure 5.3: Variation of the coupling angle with changing in the temperature; A) TE mode, B) TM mode.**

The plots of the coupling angle variation of the probe with respect to the reference (same waveguide measured under the same conditions, without monolayer) over the whole temperature range could be fitted with two different linear fits. The kink in the plot indicates the transition temperature in the monolayer. For both TE and TM modes, the transition approximately occurred at  $42^\circ\text{C}$ .

This result contrasts with the one obtained from the DSC method, on the bulk product. On the other hand, they are in perfect agreement with the physical constants determined in previous literature, predicting an acyl chain melt between  $36^\circ\text{C}$  (hydrated) and  $43.1^\circ\text{C}$  (dry) of DC<sub>23</sub>PC. This dramatic shift in the melting temperature can be related to the intermolecular diacetylene organization, which is highly enhanced in a liquid crystalline monolayer.

## 6. Langmuir films

The surface pressure-area isotherm, measured on a Langmuir film balance gives valuable information about the properties of a monolayer. The anchor lipids have been characterized as films formed at the air-water interface. As described before (see Chapter Materials & Methods), the form of the Langmuir isotherm gives information about the interactions between the lipids.

The lipids studied are again depicted in Figure 6.1.

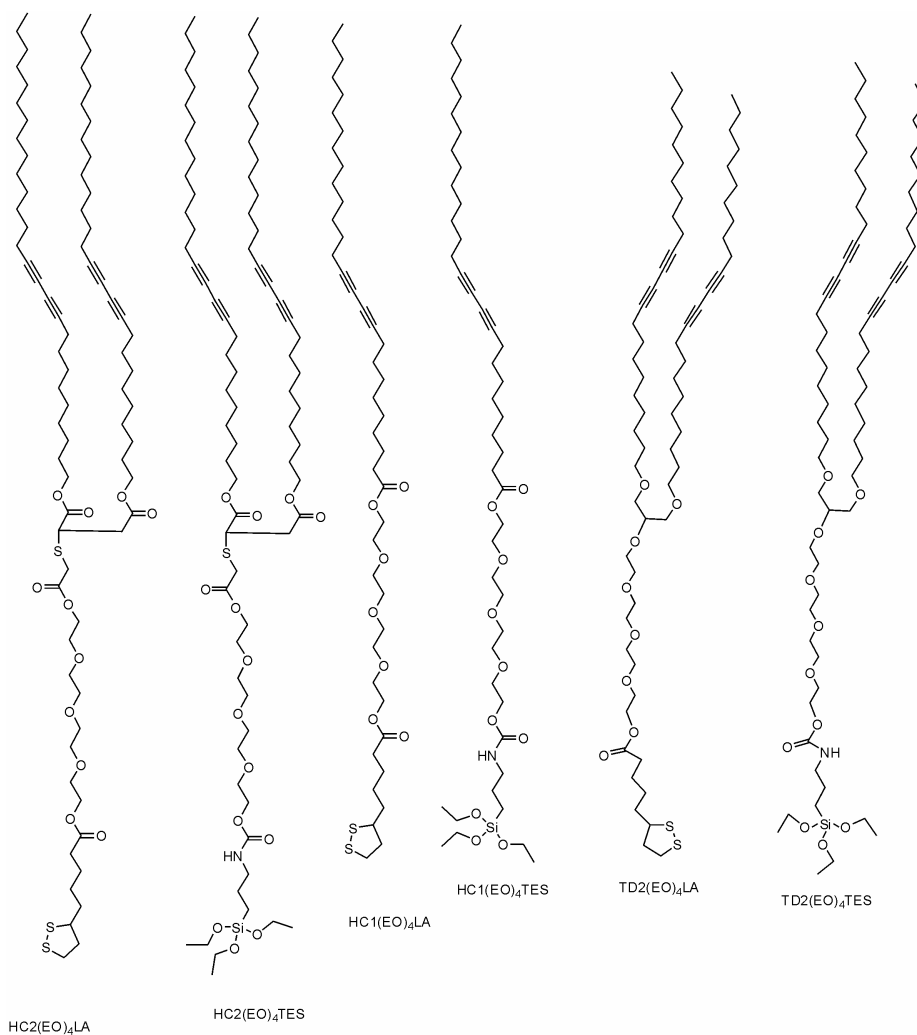


**Figure 6.1: Chemical formula of the anchor lipids studied by Langmuir film technique.**

The isotherms of the molecules were paired, according to their chemical similitude. Hence, three groups are presented, the first one of lipids build with ether linking, then the single stranded ester linked and finally the double stranded ester linked lipids.

## 6.1. TD2(EO)<sub>4</sub>LA and TD2(EO)<sub>4</sub>TES

The Langmuir isotherms of the ether linked molecules TD2(EO)<sub>4</sub>LA and TD2(EO)<sub>4</sub>TES at 20°C, 15°C and 10°C are depicted in Figure 6.2.

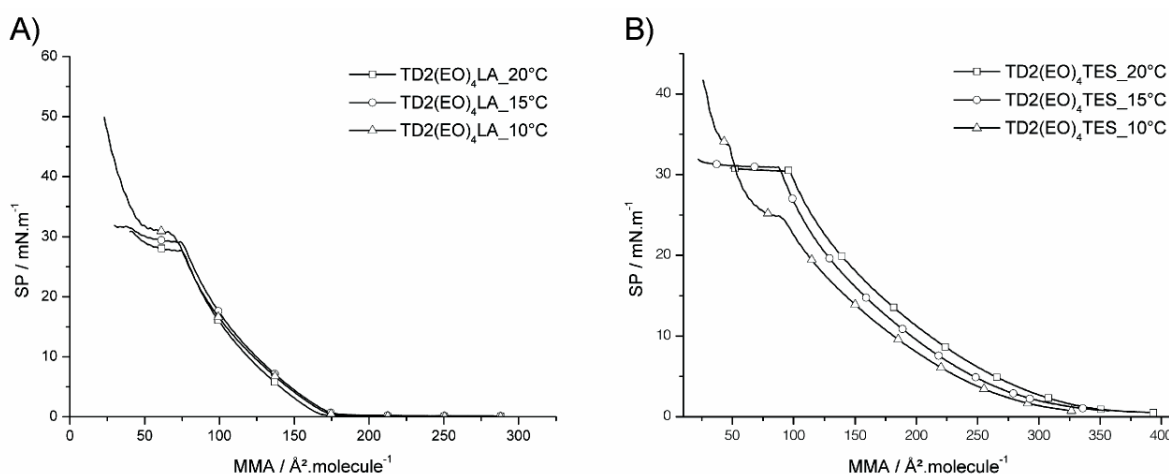


**Figure 6.2: Langmuir isotherms of TD2(EO)<sub>4</sub>LA (A) and TD2(EO)<sub>4</sub>TES (B) at 20°C, 15°C, 10°C (indicated in the legend).**

Upon compression, an important shift of the mean molecular areas (MMA) at the gas to liquid expanded (LE) phase transition was measured for both molecules. The surface pressure in the TD2(EO)<sub>4</sub>LA films started to rise at 175 Å<sup>2</sup>/molecule and at 340 Å<sup>2</sup>/molecule for TD2(EO)<sub>4</sub>TES. This shift is directly correlated with the size of the anchor group. The triethoxysilane group is bulkier as the lipoic acid and induces repulsion between the molecules on the surface at higher MMAs.<sup>[24, 100]</sup> The transition gas-LE is therefore governed by the hydrophilic parts of the lipids. The transition to a liquid condensed (LC) phase is most probably dominated by interactions between the hydrophobic parts. For both lipids, the gas-LE transition showed only little temperature dependence.

The TD2(EO)<sub>4</sub>LA films show an LC/LE transition plateau at MMAs ranging from 70 to 75 Å<sup>2</sup>/molecules ending with a little increase in surface pressure before collapse at 40 Å<sup>2</sup>/molecule and 30 to 31 mN/m. The film at 10°C could be compressed above this limit, creating an LC phase collapsing at 23 Å<sup>2</sup>/molecule and 50 mN/m.

The temperature had a significant effect on the isotherms during the LC/LE transition plateau, inducing an increase of the surface pressure at the same MMAs with decreasing temperature.

**TD2(EO)<sub>4</sub>TES:** the isotherms of the films compressed at 20°C and 15°C show a collapse directly after the LE phase at MMAs of 95 Å<sup>2</sup>/molecule (20°C) and 90 Å<sup>2</sup>/molecule (15°C), at surface pressures of 30-31 mN/m. This is similar to TD2(EO)<sub>4</sub>LA at the same temperatures. But unlike TD2(EO)<sub>4</sub>LA, the LE phase was greatly influenced by the change of temperature, producing the contrary effect as before, i.e. the isotherm are shifted to lower surface pressure for the same MMA at lower temperature.

Finally, the 10°C isotherm fades from the LE in an LC phase with a little transition plateau, collapsing at 26 Å<sup>2</sup>/molecule and 41 mN/m.

It was reported that diacetylene lipids behave like their saturated counterparts but with lower critical transition temperatures.<sup>[100]</sup> Therefore, the expected response of the isotherms to lower temperature would be a lowering of the surface pressure.<sup>[101]</sup> This behavior was displayed by TD2(EO)<sub>4</sub>TES, where the LE part of the isotherms constantly shifted with temperature, to even induce an LC phase at 10°C. On the other hand, the increase in surface pressure during the LC/LE plateau before collapse on the TD2(EO)<sub>4</sub>LA isotherms was related to the enhanced compressibility of the monolayers at lower temperature.<sup>[101]</sup>

With the comparison of the isotherms of both molecules, it is possible to determine which part of the lipid has the greater influence on the film properties at which MMAs. As described previously, the gas/LE phase transition is mainly influenced by the hydrophilic part of the molecule, determining the space each lipid can occupy before interacting with each other. Identically, at the LE/collapse transition, the occupied space of the TD2(EO)<sub>4</sub>TES molecules is almost double than for the lipoic acid terminated one. But on the other hand, the surface pressure at the collapse (for the isotherms at 20°C and 15°C, showing no LC phase) is identical (30-31 mN/m), being therefore related to the packing of the hydrophobic chains. Finally, the collapses of the LC phases occur at the same MMA, demonstrating again the interactions between the diacetylene chains, being the same for both lipids. The difference of surface pressure at the collapse is probably due to the ability of one anchor groups to order and be compressed more than the other.

Nevertheless, the crystalline state of the monolayers, necessary for the topochemical reaction can only be obtained under cooling of the subphase, what makes the stability and therefore the reactivity of the prepared monolayer at room temperature questionable.

## 6.2. HC<sub>1</sub>(EO)<sub>4</sub>LA and HC<sub>1</sub>(EO)<sub>4</sub>TES

The Langmuir isotherms of the single stranded ester linked molecules, HC<sub>1</sub>(EO)<sub>4</sub>LA and HC<sub>1</sub>(EO)<sub>4</sub>TES at 20°C, 15°C and 10°C are depicted in Figure 6.3.

As for the ether linked molecules, a large influence of the anchor group could be seen as a shift in the gas to LE phase transition. The transition starts at 165 Å<sup>2</sup>/molecule for HC<sub>1</sub>(EO)<sub>4</sub>LA and 280 Å<sup>2</sup>/molecule for HC<sub>1</sub>(EO)<sub>4</sub>TES.

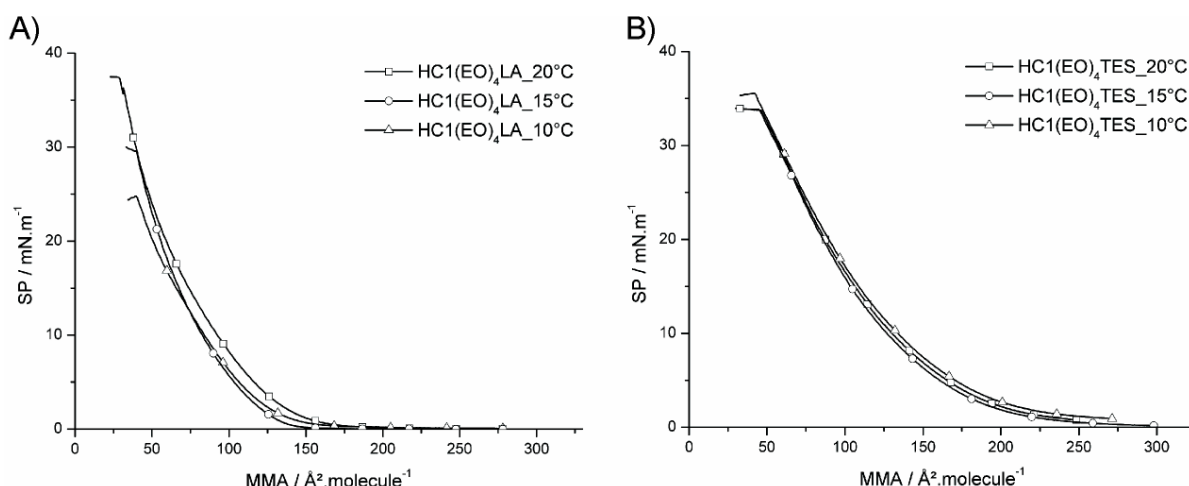


**Figure 6.3: Langmuir isotherms of HC<sub>1</sub>(EO)<sub>4</sub>LA (A) and HC<sub>1</sub>(EO)<sub>4</sub>TES (B)) at 20°C, 15°C, 10°C (indicated in the legend).**

The temperature did not have a large influence on the isotherms during the LE phase as before. The pressure at the collapse for HC<sub>1</sub>(EO)<sub>4</sub>LA monolayer decreased with decreasing temperature, indicating a reduced compressibility, although the contrary was expected<sup>[100]</sup> and also seen for both other double stranded lipids.

The films collapsed at comparable MMAs, i.e. 32–39 Å<sup>2</sup>/molecule for HC<sub>1</sub>(EO)<sub>4</sub>LA and 40–44 Å<sup>2</sup>/molecule, but not at the same surface pressure, maybe related to the anchor groups, as previously discussed.

### 6.3. HC2(EO)<sub>4</sub>LA and HC2(EO)<sub>4</sub>TES

The Langmuir isotherms of the single stranded ester linked molecules, HC2(EO)<sub>4</sub>LA and HC2(EO)<sub>4</sub>TES at 20°C, 15°C and 10°C are depicted in Figure 6.4.

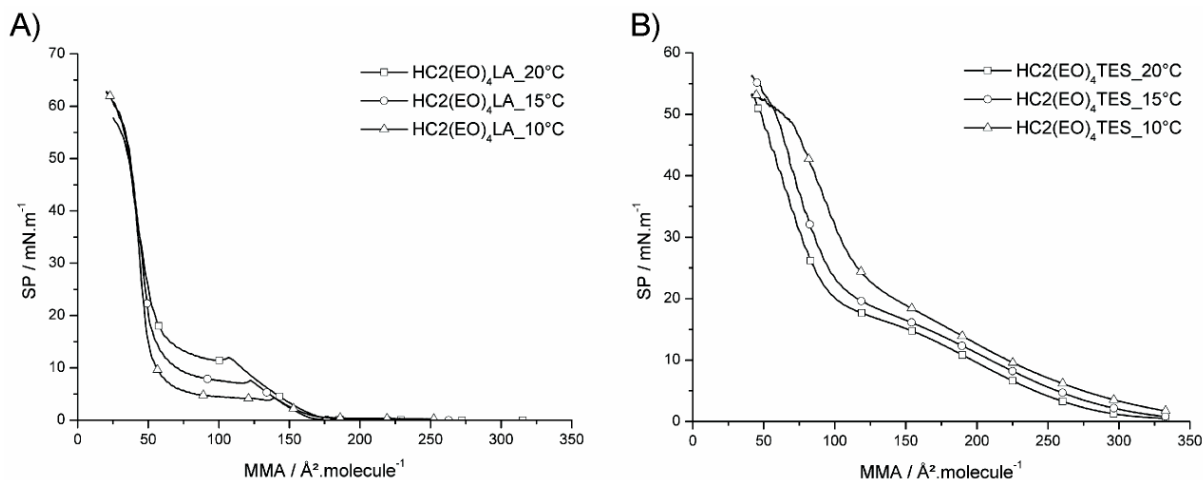


**Figure 6.4: Langmuir isotherms of HC2(EO)<sub>4</sub>LA (A) and HC2(EO)<sub>4</sub>TES (B) at 20°C, 15°C, 10°C (indicated in the legend).**

As for all the other isotherms, the effect of the silane end group could be clearly noticed. The first phase transition occurs at 175Å<sup>2</sup>/molecule for HC2(EO)<sub>4</sub>LA and at roughly 340Å<sup>2</sup>/molecule for HC2(EO)<sub>4</sub>TES. A correlation can be seen between the TD2-lipid and HC2-lipid series: although having different hydrophobic chain length, the gas/LE phase transition remains at the same area per molecule, confirming the assumption that it results from the interactions between the hydrophilic chains.

**HC2(EO)<sub>4</sub>LA:** the transition from the LE phase to the LC/LE plateau occurs at relatively low surface pressures, ranging from 4 to 10mN/m, indicating a rapid organization of the hydrophobic chains in crystalline domains over the whole temperature range. At the onset of the LC/LE transition plateau, an “overshoot transition”, very characteristic for very stiff films is observed.<sup>[31, 102]</sup> The collapse pressure of 57 to 63mN/m was considerably higher than in the case of TD2(EO)<sub>4</sub>LA, but the MMA remained the same with 22Å<sup>2</sup>/molecule. The increase in the surface pressure at collapse is related to the 4 additional methylene groups in the hydrophobic chains and the hydrogen bonds due to the presence of ester bonds at the central glycol linker of the HC2-lipids. The effect of the temperature was as

expected, with a reduction of the surface pressure during the plateau with decreasing temperature.

**HC2(EO)<sub>4</sub>TES:** from a very pronounced LE phase a direct transition towards the LC phase is induced at approximately 15mN/m without any LC/LE transition plateau. The collapse with an MMA of 41 $\text{\AA}^2/\text{molecule}$  is again the double as for the lipoic acid analogue, but with a comparable surface pressure of 53 to 57mN/m. The isotherms show an opposite temperature dependence, compared to the HC2(EO)<sub>4</sub>LA, i.e. a decrease of the surface pressure with increasing temperature. The reason is yet to be clarified.

Both HC2(EO)<sub>4</sub>LA and HC2(EO)<sub>4</sub>TES undergo a crystallization at the air-water interface upon reduction of the available area per molecule, even at room temperature. Hence, it is possible to prepare ordered, liquid crystalline films on the Langmuir trough and transfer them afterwards on a solid substrate, ensuring the creation of a polymerizable monolayer even at room temperature. Since both lipids can be covalently bound, either on gold or silicon oxide, selective functionalization of heterogeneous substrates can be achieved.

## 7. UV-Visible spectroscopy

The topochemical polymerization of diacetylenes, resulting in a conjugated backbone made from alternating double and triple bonds, exhibit strong absorption bands in the visible spectra of light. This results typically in a deep blue or deep red coloration of the films. Hence, the study of the UV-Vis absorption spectra upon polymerization is a very reliable and easy-to-apply method for the determination of the reaction kinetic.

Diacetylene monomers are known to absorb in the near UV range of light ( $\lambda < 300\text{nm}$ ), making them sensitive to photolithographic polymerization. The molar absorption coefficient of 1,2-bis(tricosa-10,12-diynoyl)-*sn*-glycero-3-phosphatidylcholine is as high as  $5,1 \cdot 10^2 \text{M}^{-1} \cdot \text{cm}^{-1}$ .<sup>[26]</sup> However, the monomers do not absorb in the visible part of the light spectra ( $\lambda > 300\text{nm}$ ).

The evolution of the absorbance spectra with advancing polymerization of the diacetylenes was intensively studied.<sup>[26, 30, 31, 43, 64]</sup> With low conversion, the polymer initially absorbs in the range of 620-630nm, producing a blue film, which converts slowly to the more stable red form (490-550nm) with increasing polymerization degree. More specific studies on diacetylene phospholipids identified the absorption maxima at 490 and 529nm.<sup>[26]</sup>

In order to determine the polymerization kinetic of the synthesized anchor lipids, UV-Vis spectra were recorded in transmission from 820nm to 220nm between two UV irradiation of the film. The monomolecular films were transferred onto substrates as ordered films from the surface of an LB trough. The polymerization was achieved by UV illumination at 254nm at room temperature under N<sub>2</sub> atmosphere, using a 6W laboratory hand lamp at a distance of 5cm, delivering  $5,8 \text{mW} \cdot \text{cm}^{-2}$ .

### 7.1. HC2(EO)<sub>4</sub>TES on quartz

The polymerization kinetic of the silane based lipid HC2(EO)<sub>4</sub>TES was followed on quartz substrates. The monolayers were transferred at surface pressures of 50mN/m from the water subphase via LB transfer with a deposition speed of 1mm/min.

Figure 7.1 shows the evolution of the UV-Vis spectra with increasing UV illumination time.

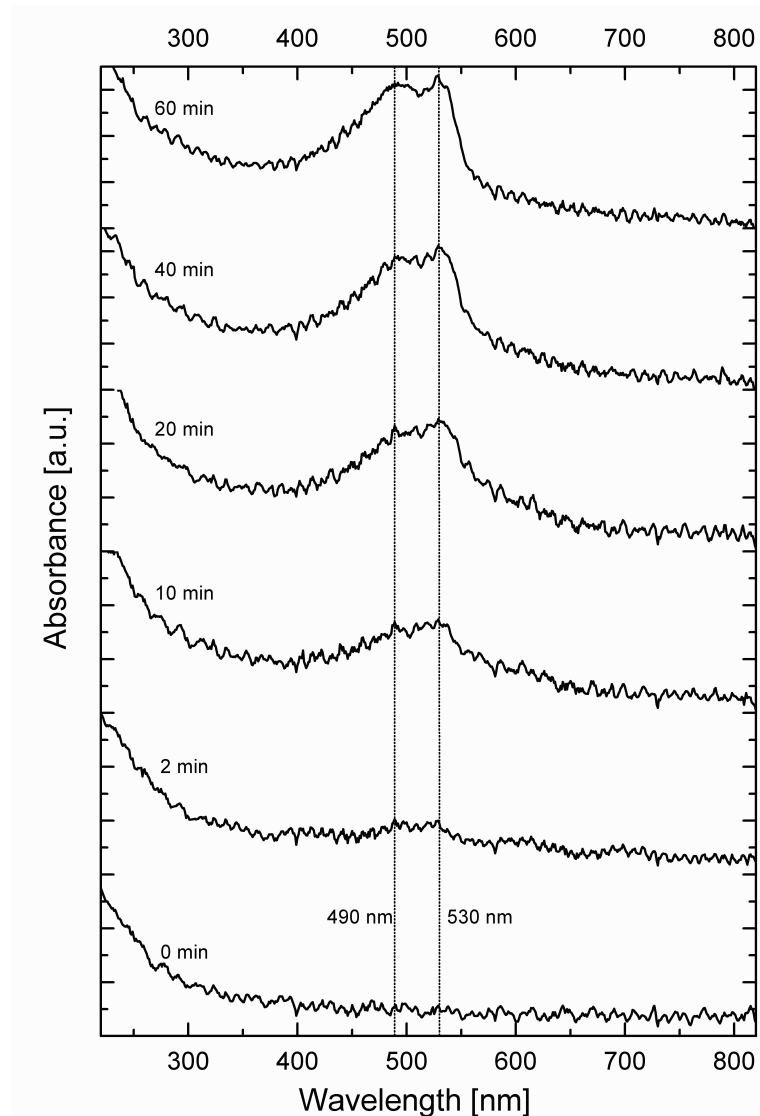


**Figure 7.1: Evolution of the UV-Vis spectra of HC2(EO)<sub>4</sub>TES on quartz with UV irradiation time.**

The absorption spectrum of the diacetylene lipid monolayer before illumination can be separated in two parts. Under 350nm, the diacetylene groups absorb light, allowing the use of high energy UV irradiation as a source of initiation for the polymerization. From 350nm to 820nm, no other absorption band was recorded, confirming the monomeric state of the film. Upon polymerization, the film increasingly absorbed in the blue region of the visible spectra, but not enough to be seen by eyes. After 60min UV irradiation, the photoproduct absorbed at 490nm and 530nm as expected.<sup>[26, 30]</sup> This so-called “red form” of the polymer is associated with a backbone of alternating double and triple bonds. The formation of the intermediate blue form could not be observed in our case.

The increase of the polymer film absorbance at 530nm, with respect to the non polymerized monolayer is plotted in Figure 7.2 as function of the irradiation time.

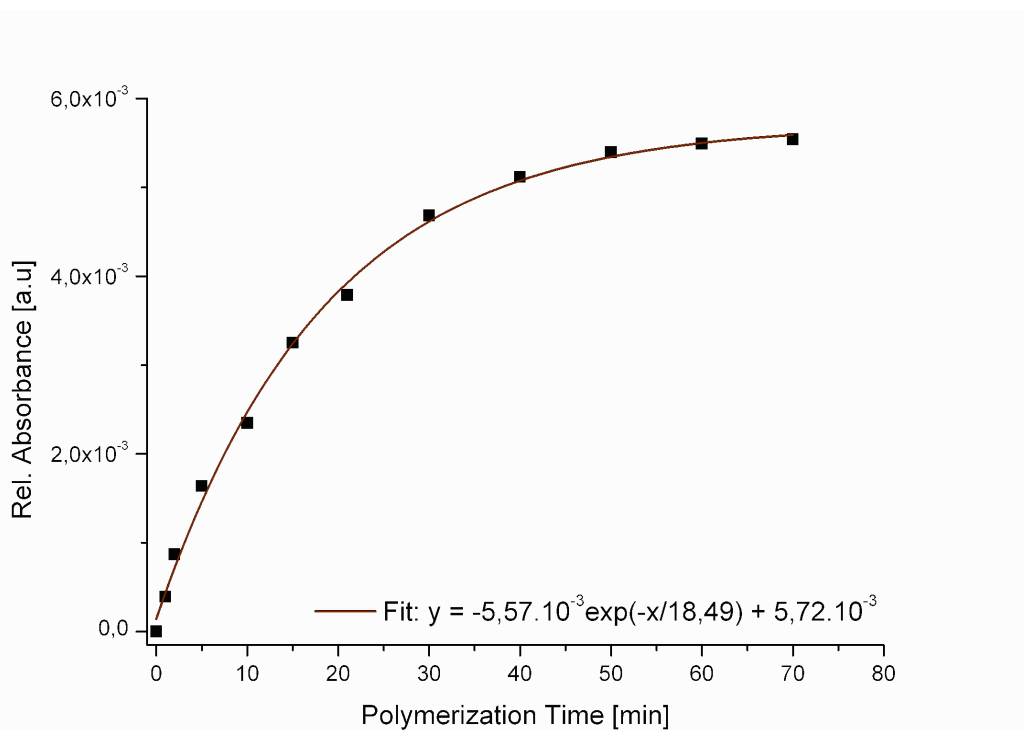


**Figure 7.2: Relative absorbance of the HC2(EO)<sub>4</sub>TES diacetylene film in function of the irradiation time at 530nm.**

The kinetic of polymerization was followed by the increase in absorption at the maxima of 530nm. The plot shows an exponential rise of the absorption with time. The sample was completely cross-linked after 60 to 70min UV treatment, with a fitted relative absorbance at  $t_{\infty}$  of  $5,72 \cdot 10^{-3}$  a.u. As stated before, the absorbance was quite low due to the little thickness of the film.

## 7.2. HC2(EO)<sub>4</sub>LA on quartz

Monomeric films of HC2(EO)<sub>4</sub>LA molecules were also transferred in the LC phase (at a surface pressure of 52mN/m) on a quartz substrate with a constant deposition speed of 1mm/min.

The following plot in Figure 7.3 shows as previously the evolution of the absorption bands in the region from 220 to 820nm upon UV irradiation of the sample.

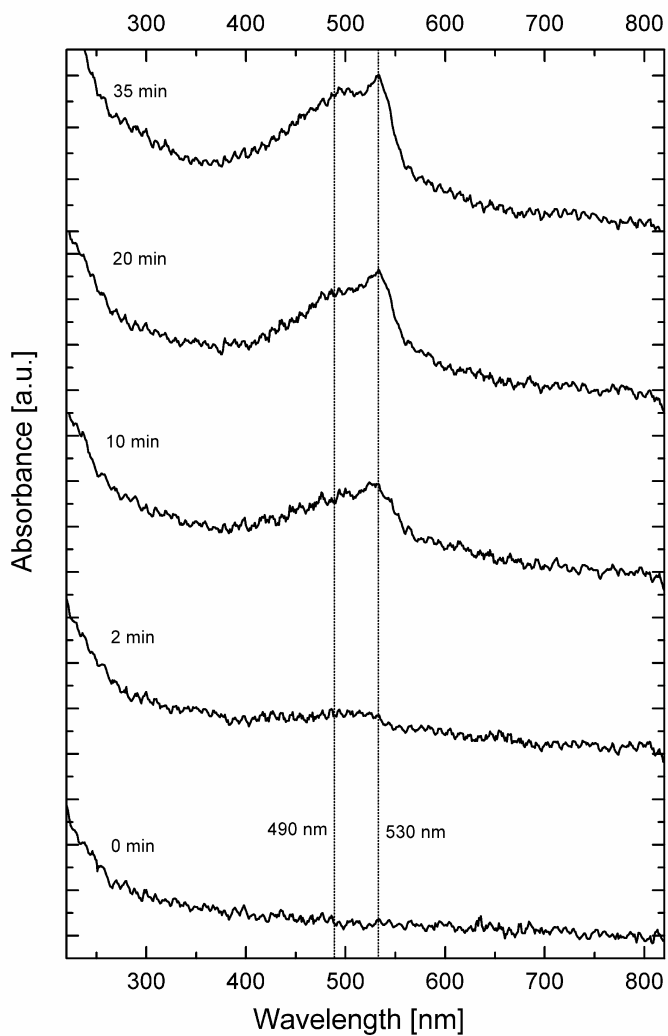


**Figure 7.3: Evolution of the UV-Vis spectra of HC<sub>2</sub>(EO)<sub>4</sub>LA on quartz with UV irradiation time.**

As in the case of HC<sub>2</sub>(EO)<sub>4</sub>TES, the characteristic peaks for the conjugated backbone of polymerized diacetylenes appeared on the UV-Vis spectra. Also, the intermediate blue form of the polymer was not formed in the early stages of the polymerization process. The kinetic of polymerization was followed as the increase of the absorbance at 530nm with increasing irradiation time. The results are plotted in Figure 7.4.

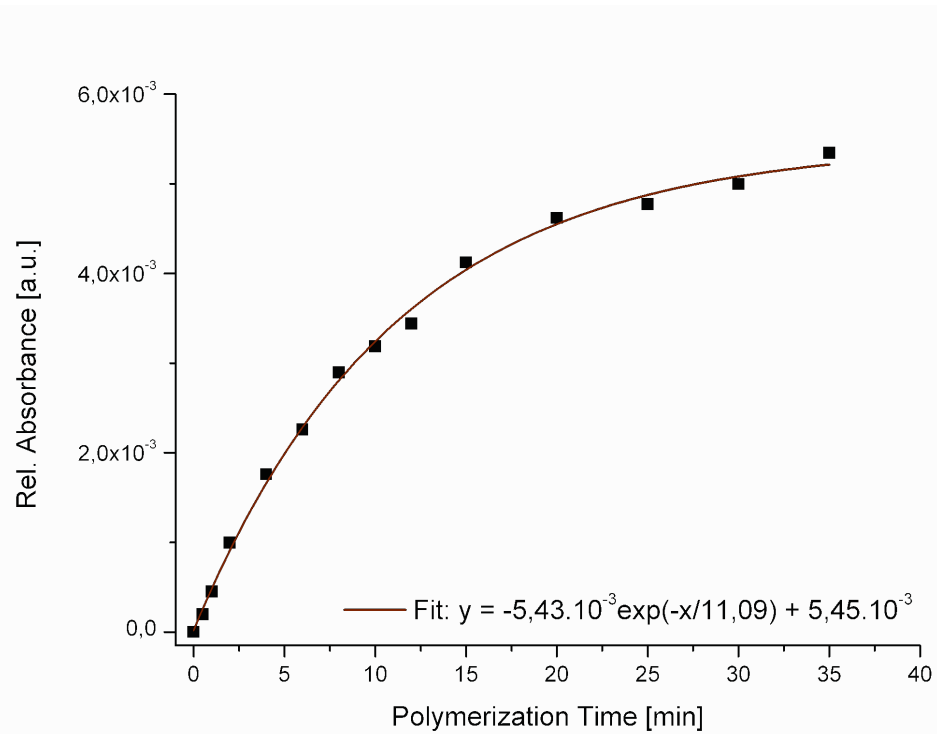


**Figure 7.4: : Relative absorbance of the HC2(EO)<sub>4</sub>LA diacetylene film in function of the irradiation time at 530nm.**

With a time constant  $\tau$  of 11,09min, the polymerization rate of HC2(EO)<sub>4</sub>LA seems to be a little higher than for HC2(EO)<sub>4</sub>TES having a  $\tau$  of 18,48min. This difference in kinetics is probably due to the better packing of the lipoic acid derivative in the film, producing bigger crystalline grains, according to the Langmuir isotherm studies (see Chapter Langmuir films) and the following fluorescence micrographs (see Figure 8.2 and Figure 8.5).

Nevertheless, the fitted absorbance at  $t_\infty$  are in both films comparable, with  $5,43 \cdot 10^{-3}$ a.u. for HC2(EO)<sub>4</sub>LA and  $5,72 \cdot 10^{-3}$ a.u. for HC2(EO)<sub>4</sub>TES. The amount of cross-linked lipids on each sample is therefore of the same order of magnitude, even if the obtained grain size of the polymerized crystallite differs (see Figure 8.2 and Figure 8.5).

## 8. Photolithographic patterning

As demonstrated before, the polymerization of the lipid monolayer can be initiated by ultraviolet light. This offers the possibility to selectively shine light on defined spots by means of a photolithographic mask, creating a pattern of polymerized and non polymerized membrane. The scheme of the process is presented in Figure 8.1. The ability to topographically structure the monolayer was a very important requirement in order to accommodate the membrane with respect to the substrate.<sup>[33, 103, 104]</sup>

After cross-linking of the lipids, the monolayers absorb light and emit fluorescence in the visible spectra due to the conjugated backbone. This allows the observation of the created patterns with fluorescence microscopy.

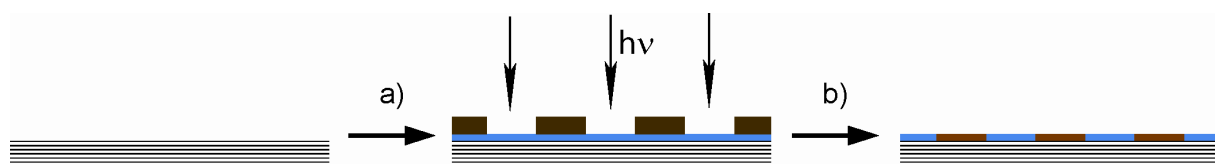


**Figure 8.1: Photopatterning of the light sensitive monolayer; a) deposition of a lipid monolayer on a substrate and application of the mask on top, b) after UV irradiation, removal of the mask, revealing the structured surface.**

The microscope used was equipped with a 490nm excitation filter and a 560nm long pass emission filter.

### 8.1. HC<sub>2</sub>(EO)<sub>4</sub>TES on quartz

The silane anchored molecules HC<sub>2</sub>(EO)<sub>4</sub>TES were transferred as monomolecular films at 50mN/m on quartz substrates (deposition speed: 1mm/min) via LB deposition and subsequently UV irradiated for 60min. The fluorescence micrograph reveals fir cone like aggregation structures after polymerization (Figure 8.2). The aggregates did most likely grow as isolated domains gathering together upon compression of the film at the air/water interface.<sup>[26, 105]</sup> At higher compression these isolated crystalline islands, forced to form a solid film (seen Chapter Langmuir isotherms, in 6.3) did not fuse to a homogeneous crystalline monolayer.

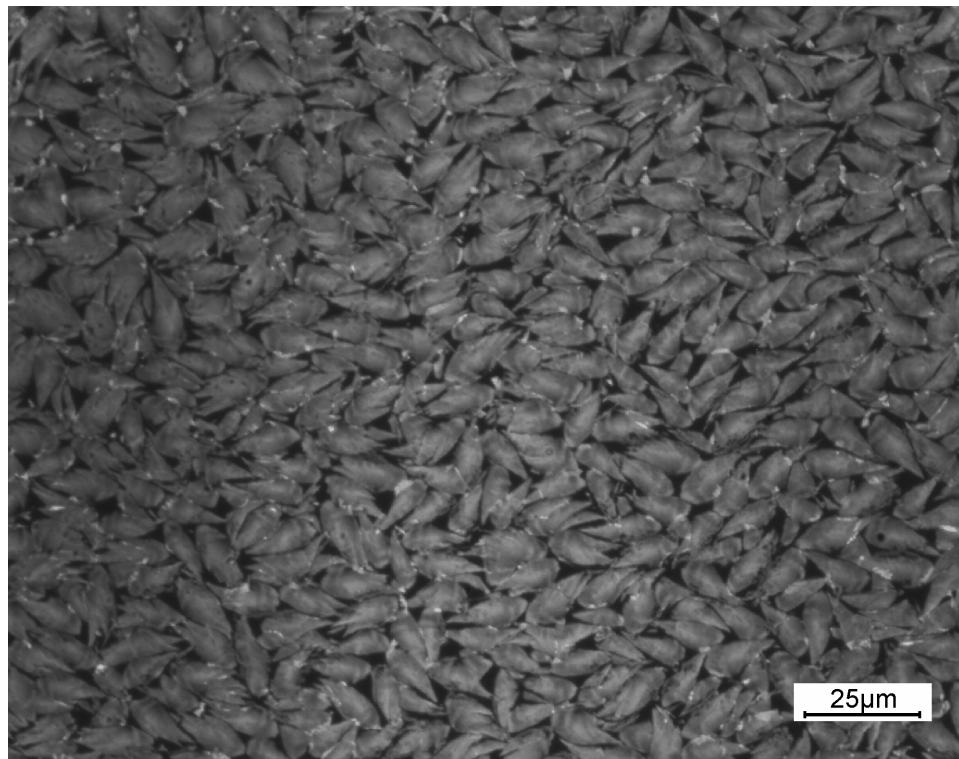


**Figure 8.2: Fluorescence micrographs of an  $\text{HC}_2(\text{EO})_4\text{TES}$  monolayer on quartz prepared at a constant compression rate.**

In order to diminish the defects in the film and force the islands to fuse to a homogeneous crystalline monolayer, a multi-step creep method of compression was applied.<sup>[106]</sup> Figure 8.3A shows the preparation process of the  $\text{HC}_2(\text{EO})_4\text{TES}$  monolayer by the multi-step creep method. Briefly, after spreading of the lipids and evaporation of the chloroform, the monolayer was compressed and held to a surface pressure of 10mN/m. The variation of the monolayer area was measured, while maintaining the surface pressure at 10mN/m, allowing the molecules to rearrange. This rearrangement was accompanied by a reduction of the area. After equilibration (30min to 1 hour) the film was compressed further to 20mN/m, and the procedure was repeated. After the last step, the monolayer was transferred on the quartz substrate with the usual procedure.

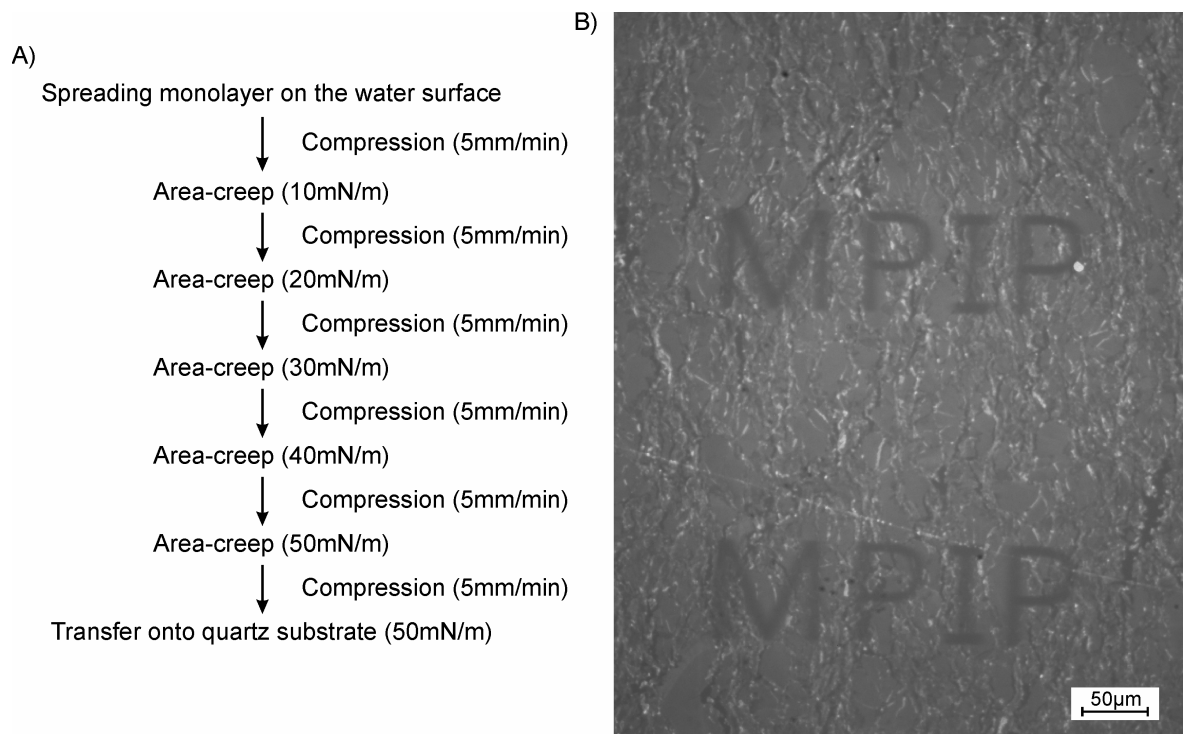


**Figure 8.3: A) Flow sheet describing the multi-step creep method, B) fluorescence micrograph of HC2(EO)<sub>4</sub>TES monolayer on quartz after a multi-step creep compression (with MPIP patterning).**

A significant enhancement of the quality of the prepared monolayer could be achieved with this method as can be seen on the fluorescence micrograph in Figure 8.2B. The crystalline grains were fused together, improving dramatically the quality of the polymerized film. Some defects and grain boundaries could still be seen, presumably due to the presence of amorphous material between the grains. In literature the contraction of the monomeric film during polymerization has also been reported,<sup>[31, 63]</sup> probably inducing in turn the distortion of the crystal lattice at the grain boundaries.

After the optimization of the monolayer quality, a photolithographic mask was applied on top of a new sample to imprint patterns. Figure 8.4 shows fluorescence micrographs of structured lipid monolayers.

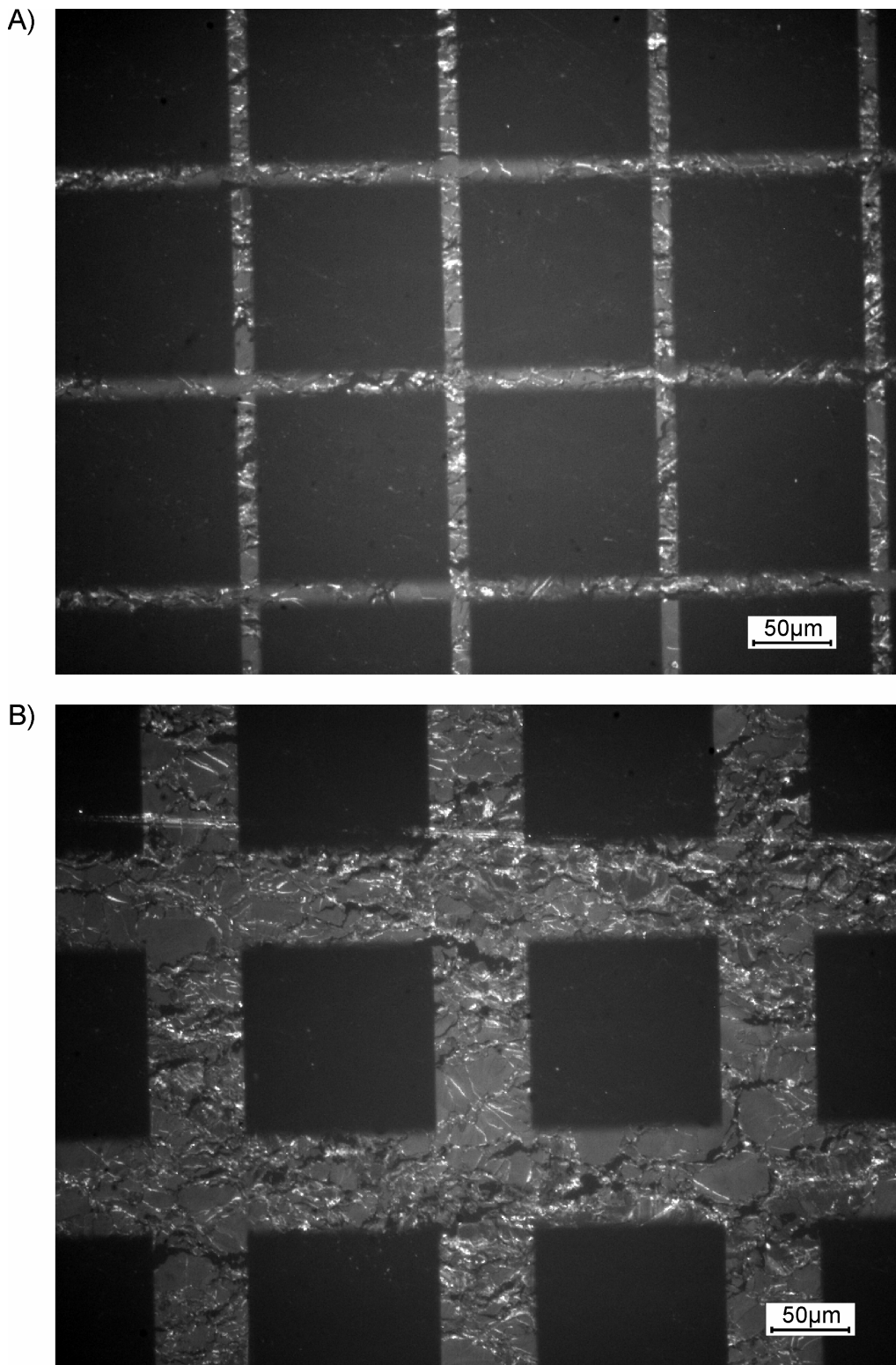


**Figure 8.4: Fluorescence micrographs of patterned HC2(EO)<sub>4</sub>TES monolayers prepared with multi-step creep compression.**

The black squares on the pictures are made of non polymerized lipids. The edges of the squares are well defined meaning that the polymerization, once initiated, did not expand in the areas covered by the mask. This would enable the patterning with micrometer precision.

Polymerized structures with submicrometer size could also be considered, but only with optical setups delivering highly parallel and focused UV light.

On Figure 8.4B the cracks or defects between grains can be clearly seen. The quality of the prepared film seems to be not as good as the one presented on Figure 8.2B. Further possibilities to improve the fusion of the lipid grains formed during compression on the water surface could be reached by implementing the multi-step creep process. Defect diminished monolayer were reported by spreading the lipids on water surface at temperature above the transition temperature, compress and then progressively cool down the subphase to induce crystallization.<sup>[106]</sup>

## 8.2. HC<sub>2</sub>(EO)<sub>4</sub>LA on quartz

Films of the disulfide ending lipid HC<sub>2</sub>(EO)<sub>4</sub>LA were also transferred via LB deposition (deposition speed: 1mm/min) at 52mN/m on quartz substrates. The anchor lipids were therefore only adsorbed on the surface and not covalently bonded.

The microscope picture in Figure 8.5 shows a polymerized monolayer of HC<sub>2</sub>(EO)<sub>4</sub>LA on quartz.

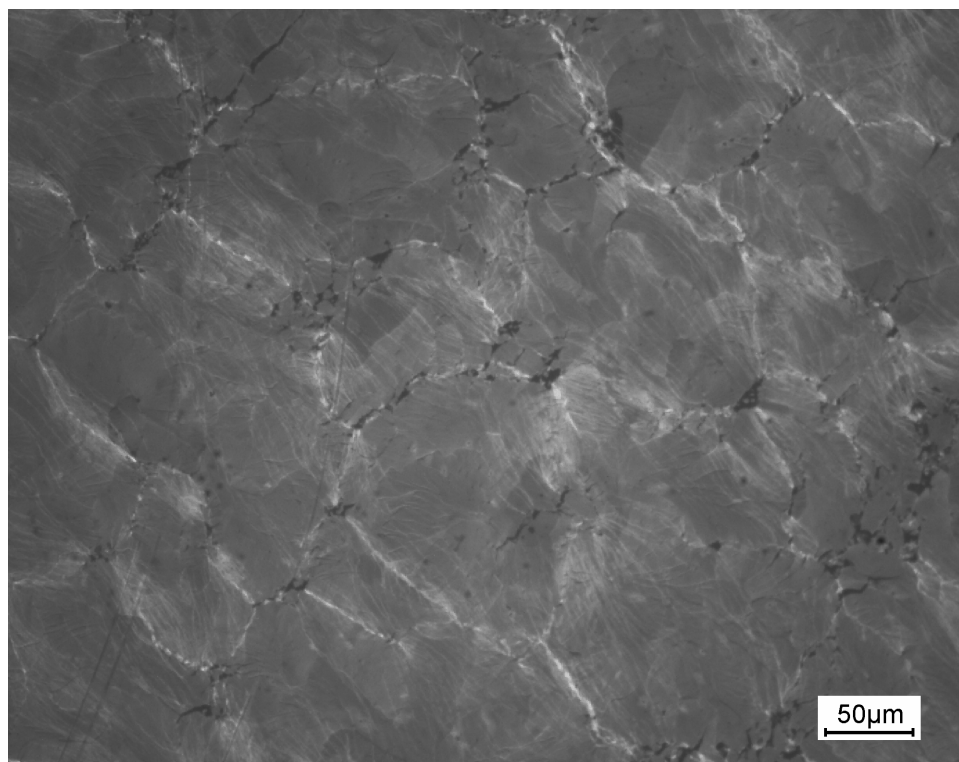


**Figure 8.5:** Fluorescence micrograph of polymerized HC<sub>2</sub>(EO)<sub>4</sub>LA on quartz.

In comparison to the monolayers of HC<sub>2</sub>(EO)<sub>4</sub>TES in Figure 8.2B, the crystal grains are much larger, ranging from 50µm to 250µm. The grain boundaries can be clearly distinguished as white lines. Within each grain even smaller domains can be identified from the difference in the gray scale, resulting from the sintering of single crystalline domains at their interfaces forming larger two dimensional crystals.

The previous study of the Langmuir isotherms of both anchor lipids already indicated the ability of HC<sub>2</sub>(EO)<sub>4</sub>LA to form very pronounced solid phases upon compression (see Chapter Langmuir isotherms). The resulting small dimension of the crystals in the case of HC<sub>2</sub>(EO)<sub>4</sub>TES can be therefore attributed to the steric hindrance between the silane anchor groups.

Patterning of the surface was also undertaken, using the same photomask as before. Figure 8.6 shows fluorescence micrographs of the polymerized structures. The non polymerized squares of the membrane array presented in Figure 8.6A have a side length of 100µm and are separated by 25µm barriers. The defects in the diffusion barriers between two possible neighboring “sensing areas” are quite few and usually do not span from one to the other. In further developments, such arrays could be polymerized over millimeter sized electrodes, reducing on one hand the sensing area and on the other hand impeding the inserted proteins to laterally diffuse over the membrane.

As presented for HC<sub>2</sub>(EO)<sub>4</sub>TES, if the defects are too numerous for the considerate application, an improvement of the quality of the transferred monolayer can be reached by applying the multi-step creep method.

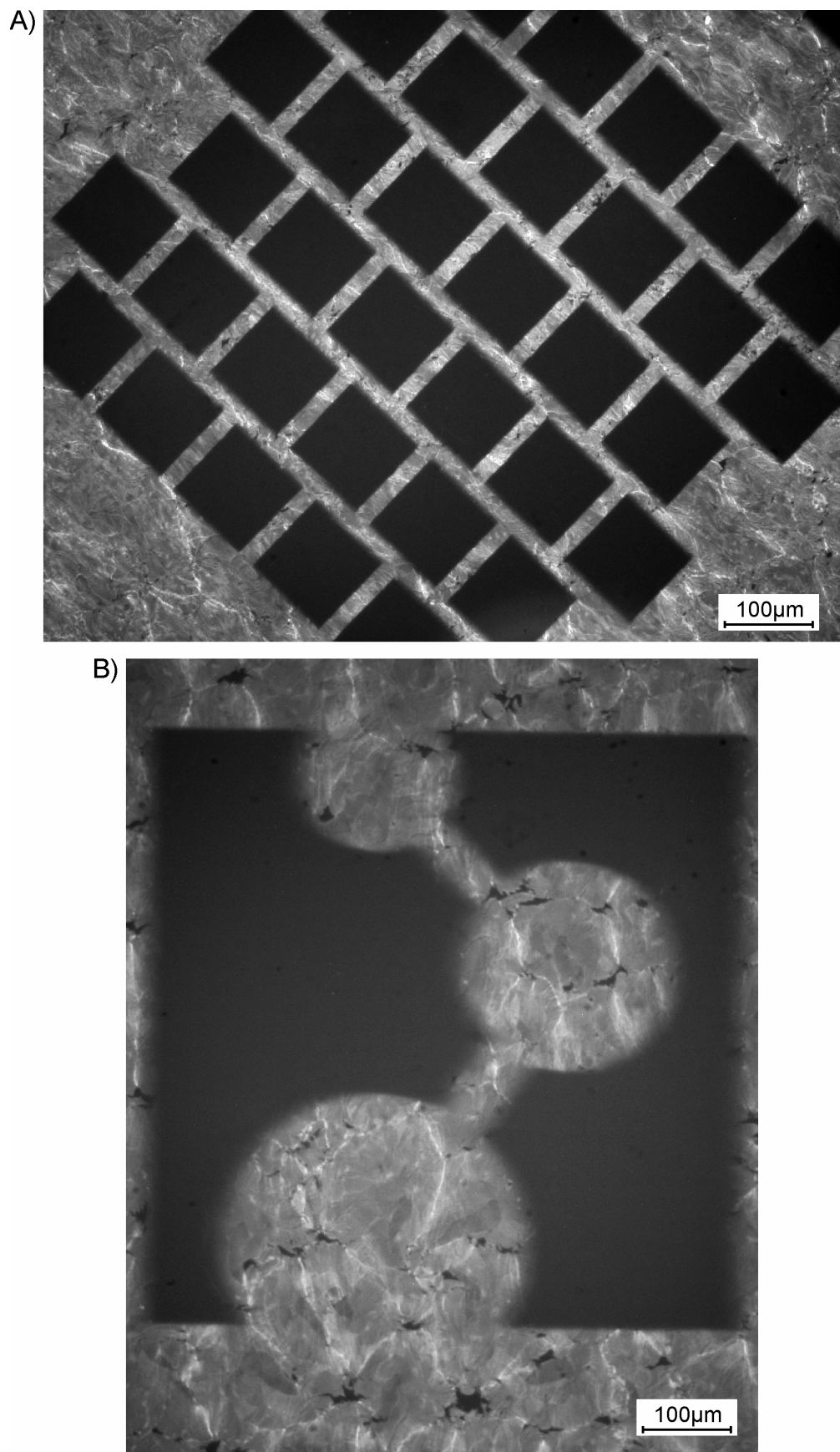


**Figure 8.6:** Fluorescence micrographs of patterned  $\text{HC}_2(\text{EO})_4\text{LA}$  monolayers on quartz.

## 9. Electrical impedance spectroscopy

Biosensors rely on biological recognition mechanisms to detect and quantify an analyte in the studied sample. This biological recognition system has to be coupled with a read-out system that transforms the molecular signal in quantifiable dimensions. In this study, tBLMs were used as model environment to accommodate ion channels, switching their conductance by the recognition event.<sup>[8, 13, 18, 20, 21, 23, 45, 107]</sup> Conductance changes in the system can be easily measured with electrical impedance spectroscopy (EIS).

To prove the potential applicability of membranes formed by the new anchor lipids, EIS measurements were performed. Monolayers were formed by self-assembly on freshly stripped TSG substrates. The bilayer formation was afterwards completed via vesicle fusion.

### 9.1. Valinomycin

Valinomycin is a polypeptide macrocycle of twelve units obtained from bacteria of the Streptomyces strains. This ionophore has a hydrophilic cavity, binding highly selectively potassium ions and a hydrophobic shell, due to the special arrangement of the enantiomers constituting the ring. As can be seen from the structural representation in Figure 9.1, the alternate coupling of optically active peptides, i.e. D- and L-valine, D-hydroxyvaleric acid and L-lactic acid over amide and ester bonds, force six carboxyl groups to point inwards the ring. Whereas the six remaining are oriented in the plane of the ring, building hydrogen bonds with the neighboring amides groups, stabilizing the structure.

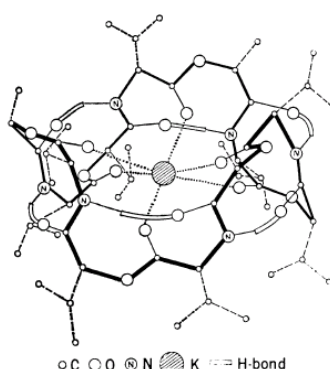


**Figure 9.1: Structure of the valinomycin-K<sup>+</sup> complex.**<sup>[108]</sup>

The coupling constant of potassium ions in the cage is  $10^4$  higher than for sodium ions. The transport of the ion occurs in four distinct steps. In the first step, the mobile carrier forms a complex with the metal ion at the membrane-aqueous solution interface. Then the formed complex migrates to the opposite surface of the membrane, overcoming a high energy activation barrier, releases the metal ion and diffuses back to the initial membrane side.<sup>[108]</sup>

Due to its high selectivity, this polypeptide ion carrier is very frequently used for the testing of model membrane systems (innumerable publications).

In the following experiment, this ionophore was employed to prove the viability of the presented system as a sensing platform.

## 9.2. Building the bilayer

As described in the introductory part, the anchor lipids were tethered overnight via a self-assembly process of HC2(EO)<sub>4</sub>LA. The created monolayer was rinsed thoroughly with ethanol. The water contact angle of the samples ranged between 100° and 110°. The vesicle fusion process can be followed by EIS (see Figure 9.2). The fitted values from the plots are presented in table 9.1.

	Resistance [ $M\Omega \cdot cm^2$ ]	Capacitance [ $\mu F \cdot cm^{-2}$ ]
Monolayer	0,020	2,77
Vesicle fusion; 0h	0,059	2,35
Vesicle fusion; 0,5h	0,36	1,35
Vesicle fusion; 6h	1,25	0,92
Bilayer	1,44	0,92

**Table 9.1:** Fitted membrane resistances and capacitances form the EIS measurement during bilayer growth.

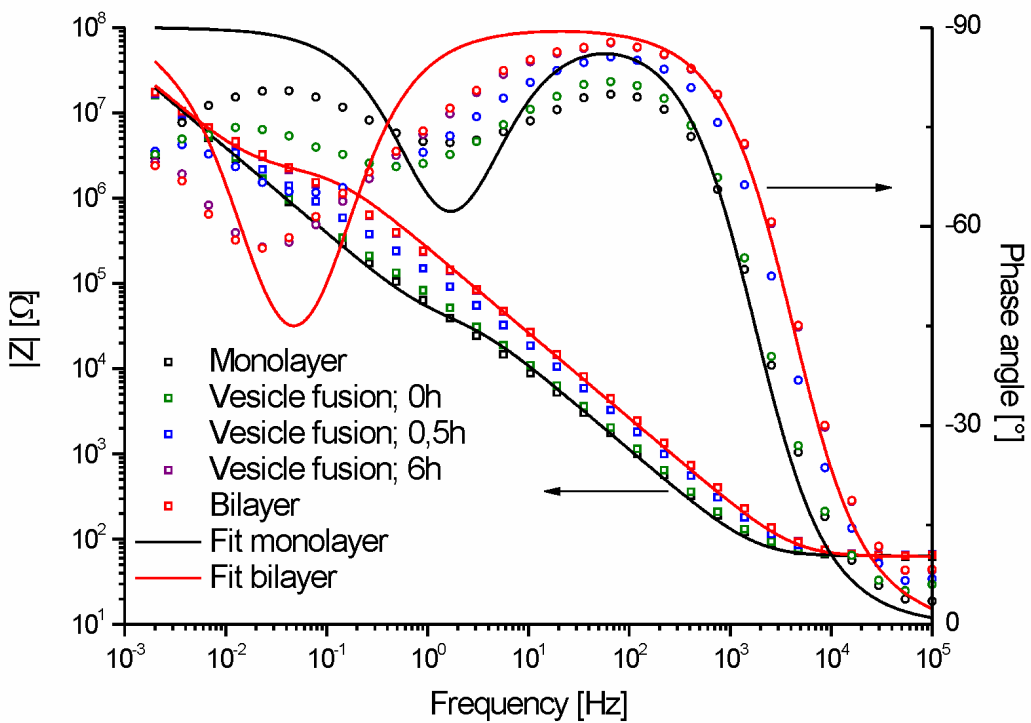


**Figure 9.2: Bode plot following a vesicle fusion on a HC<sub>2</sub>(EO)<sub>4</sub>LA monolayer.**

The resistance of the membrane to the diffusion of ions across it increased with the time. This increase is especially pronounced in the first six hours of the vesicle fusion process. In parallel, the capacitance of the membrane decreased, indicating a better charge separation, in turn denoting the reduction of defects. The impedance spectra were fitted with a simple model (see Figure 2.14), only taking in account the resistance and capacitance of the bilayer, the resistance of the electrolyte and the capacitance due to the ions in the water reservoir beneath the membrane. It is possible to examine tBLMs systems much more in details by introducing other parameters in the fit, but this goes well beyond the scope of this work.<sup>[109, 110]</sup>

### 9.3. Introduction of Valinomycin in the tBLM

To the 1ml of 0,1mM KCl buffer solution in the measurement cell, 20 $\mu$ l of a valinomycin solution (1mg/ml in trifluoroethanol) were added. After two hours incubation time, the measurement cell was rinsed with 5ml 0,1mM KCl buffer and an impedance spectrum was measured (see Figure 9.3). The fitted values from the plots are presented in table 9.2.

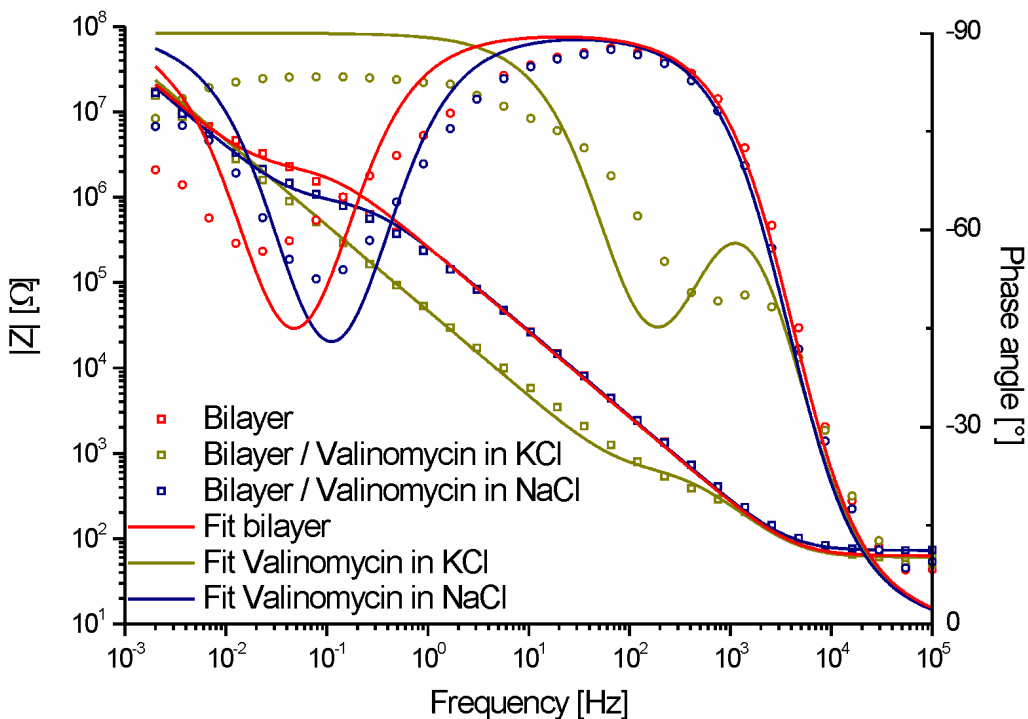


**Figure 9.3:** Bode plot of a  $\text{HC2}(\text{EO})_4\text{LA}$  bilayer functionalized with valinomycin.

	Resistance [ $\text{M}\Omega \cdot \text{cm}^2$ ]	Capacitance [ $\mu\text{F} \cdot \text{cm}^{-2}$ ]
Bilayer	1,44	0,92
Valinomycin / KCl	$0,4 \cdot 10^{-3}$	1,06
Valinomycin / NaCl	0,62	0,87

**Table 9.2:** Fitted membrane resistances and capacitances from the EIS measurement after valinomycin incorporation.

After valinomycin incorporation, a 3800 fold decrease in the membrane resistance is observed. The capacitance stayed almost constant, showing that the integrity of the membrane remained. The KCl solution was then exchanged with a 0,1mM NaCl buffer solution to impede the ion transfer across the membrane by the ionophore. The resistance increased, ranging back in the region of the initial bilayer, also the capacitance decreased again a little. The recovery of the resistance was not complete, since the removing of all  $\text{K}^+$  ions in the measurement cell is only possible to a certain extend.

This shows the possibility to employ the newly synthesized anchor lipids as platform environment for the functional incorporation of proteins.

#### 9.4. Polymerization of the bilayer

The effect of the polymerization of the tBLM on the electrical properties was also investigated. In Figure 9.4, bode plots of a bilayer are displayed, showing the evolution of the electrical properties directly after polymerization, 24h and 48h after polymerization. The fitted values from the plots are presented in table 9.3.

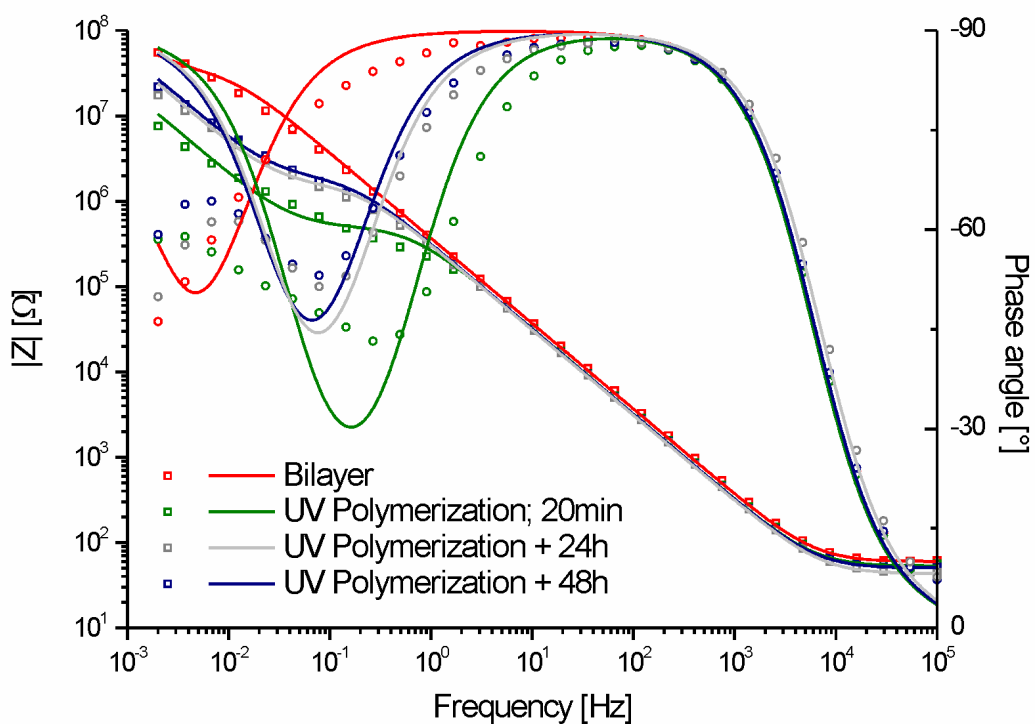


**Figure 9.4:** Bode plot of a HC2(EO)<sub>4</sub>LA bilayer after polymerization.

	Resistance [ $M\Omega \cdot cm^2$ ]	Capacitance [ $\mu F \cdot cm^{-2}$ ]
Bilayer	21,92	0,70
After 20min UV polymerization	0,37	0,68
24h after polymerization	1,27	0,77
48h after polymerization	1,04	0,78

**Table 9.3: Fitted membrane resistances and capacitances form the EIS measurement of a bilayer after polymerization.**

As described in the previous chapter, diacetylene films are reported to shrink upon polymerization.<sup>[31, 63]</sup> The effect of this shrinkage could be seen under fluorescence microscopy, by non-polymerized areas between two crystalline grains. Under impedance spectroscopy, the disturbance of the film induced by the UV polymerization results in a large decrease in the membrane resistance. However, the capacitance remained constant, attesting in turn that the membrane remained tethered to the substrate.

The partially cross-linked films were measured again 24h and 48h after UV irradiation. The membrane partially recovered its resistance as a result of the “self-healing” ability of a fluid tBLM. The distal leaflet was composed of DPhyPC, which are free to diffuse. The free lipids were then integrated in the defects, reducing the free energy of the system, resulting from the exposition of hydrophobic chains to aqueous media, thus completing the bilayer.<sup>[111]</sup>

## 10. Fluorescence recovery after photobleaching

The aim of this study was the development of a patterning method for tBLMs. Two approaches have been successfully followed, first the synthesis of polymerizable anchor lipids, which can be selectively cross-linked on a surface, second the conception of laterally structured substrates. Both approaches can be combined, taking advantage of the conductor/insulator patterning of the substrate and the selective deposition of a monolayer via self-assembly.

In order to show the efficacy of the anchor lipids as diffusion barriers, substrates were prepared having a gold matrix with embedded  $\text{SiO}_x$  discs and selectively coated with  $\text{HC}_2(\text{EO})_4\text{LA}$ . After polymerization of the diacetylene lipids on the gold parts, a fluorescent bilayer (1 mol% DOPE-NBD in DPhyPC) was deposited over the tethered lipids covering the gold matrix and over the hydrophilic  $\text{SiO}_x$  discs. The objective was to create a bilayer so that on the gold surfaces a tBLM was formed, using the polymerized  $\text{HC}_2(\text{EO})_4\text{LA}$  as monolayer and on the  $\text{SiO}_x$  parts a type of SSM, suspended within a tBLM structure (see Figure 10.1). It was shown previously that lipids preferentially form a monomolecular layer when they spread on a hydrophobic surface and bilayers on a hydrophilic surface.<sup>[112]</sup>

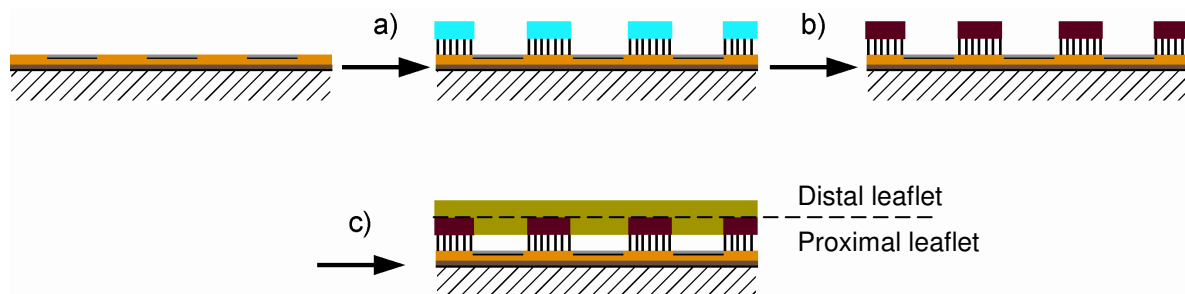


**Figure 10.1: Preparation of the polymerized tBLM on top of the structured substrate; a) self-assembly of  $\text{HC}_2(\text{EO})_4\text{LA}$ , b) UV polymerization of the monolayer, c) deposition of the bilayer via rapid solvent exchange.**

To prove the possibility to create an archipelago of fluid membrane bilayers corralled in a solid matrix, the diffusion of the free lipids over the  $\text{SiO}_x$  discs was studied. FRAP measurements were performed over the discs, having a size inferior to the laser spot, allowing the bleaching of a complete island at once. The mixed architecture was expected

to have a fluid distal leaflet, connecting the monomolecular layer over the tBLMs structures to the upper layer of the bilayer on the oxide discs and a confined proximal leaflet in the SSM bilayer.

Additionally, a selective chemical bleaching of the fluorophores in the distal leaflet was achieved. Following an experimental procedure introduced by McIntyre<sup>[113]</sup> to determine the phospholipid membrane asymmetry by fluorescence assay, the NBD fluorescent groups were reduced as depicted in Figure 10.2. The reducing agent, sodium dithionite, can only access the fluorophores in the outer leaflet, due to the sealing properties of the bilayer. This enables the separate measurement of both leaflets.

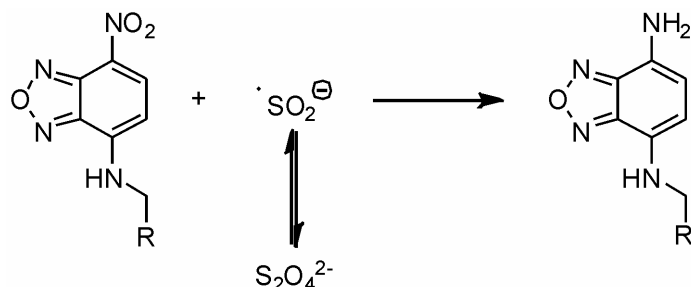


**Figure 10.2: Reduction of 7-nitro-2,1,3-benzoxadiazol-4-yl-labeled lipids to 7-amino-2,1,3-benzoxadiazol-4-yl-labeled lipids with dithionite.**

## 10.1. Sample preparation

In Figure 10.3 the flow sheet of the substrate production process is presented. On a clean silicon wafer, covered with a protective layer of OTE, silica beads of 2µm in diameter (Duke Scientific Corp., CA, USA) were spin coated from a low concentrated ethanolic solution at 1500rpm for 60sec. Once the beads were spread over the surface, layers of 50nm Au and 5nm Cr were evaporated. The glass microspheres were removed from the substrate by intensive rinsing with THF. Subsequently, 110nm of SiO<sub>x</sub>, 5nm Cr and 100nm Au were consecutively deposited before gluing of the microscope backslide, similar to the other procedures (see Chapter Ultra flat heterogeneously structured substrates). The additional layers of Cr and Au after evaporation of the SiO<sub>x</sub> discs serve as shield against back-fluorescence. Samples were first prepared without this supplementary layers and fluorescence raising form the epoxy glue through the transparent SiO<sub>x</sub> layer was impeding the FRAP measurement.

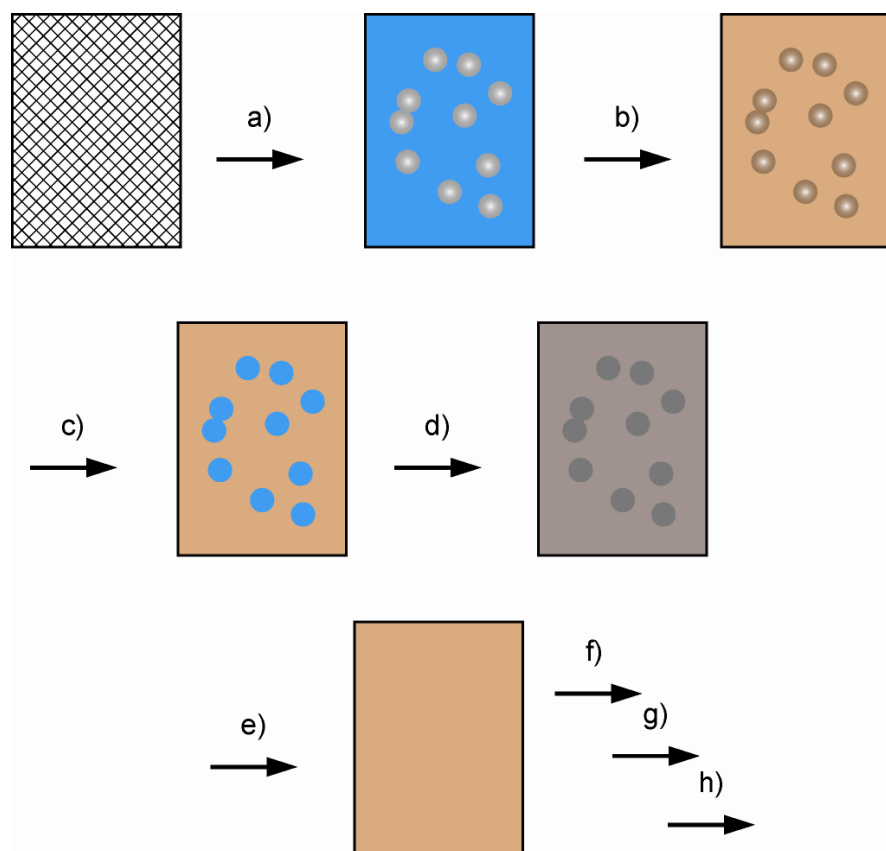


**Figure 10.3: Preparation of the FRAP substrates;** a) surface modification of a silicon wafer with OTE and spin coating of the silica beads, b) successive evaporation of Au (50nm) and Cr (5nm), c) removal of the beads with THF, d) evaporation of  $\text{SiO}_x$  (110nm), e) successive evaporation of Cr (5nm) and Au (100nm), f) gluing of a microscope slide, g) curing of the epoxy glue, h) stripping of the substrate.

After fabrication, the substrates were functionalized with the dithiolane lipids via self-assembly according to a procedure described before (see Chapter Materials & Methods). The lipids were subsequently polymerized with UV irradiation, producing diffusion barriers for the proximal leaflet. Finally, a bilayer was formed using the rapid solvent exchange technique allowing the production of mixed fluid mono- and bilayer as can be seen on Figure 10.1.

## 10.2.Bilayer formation

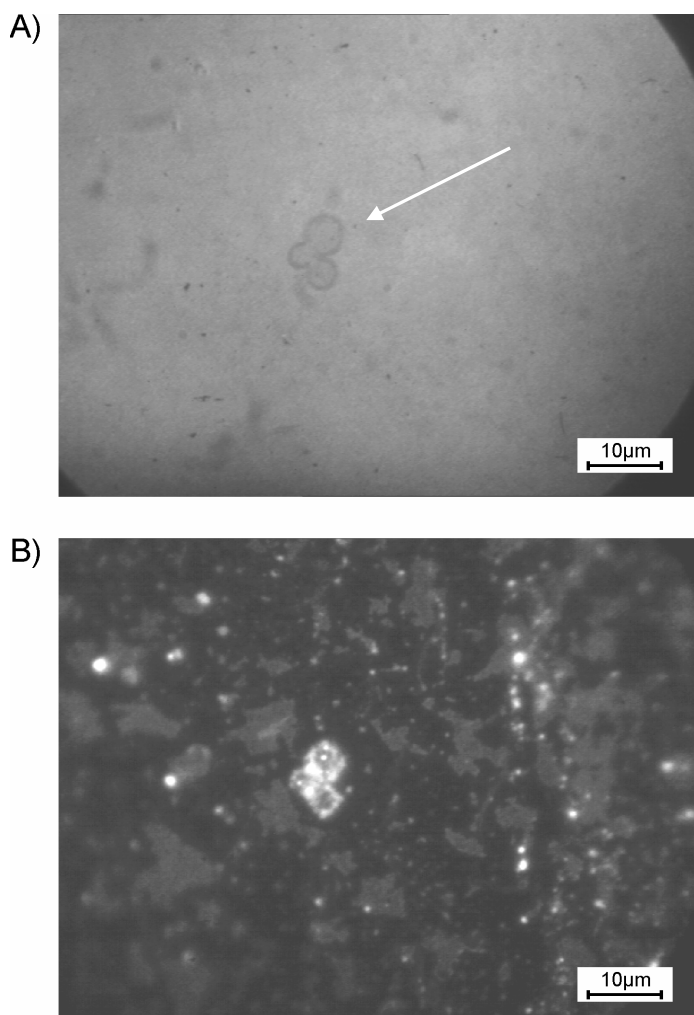


**Figure 10.4: Micrographs of a FRAP substrate on the same spot; A) DIC image, B) fluorescence image.**

On the micrograph in Figure 10.4A an assembly of three  $\text{SiO}_x$  discs can be recognized in the center (white arrow). This structure, resulting from the agglomeration of three silica beads during the spin-coating process can be also distinguished on the fluorescence picture (Figure 10.4B), resulting from the bilayer formation. Some lighter fluorescent patches were also found on the surface of the tBLM, where no fluorescence was expected due to the quenching properties of the underlying gold surface. These structures were assumed to be multilayers or vesicles formed spontaneously during the rapid solvent exchange process, even though the cell was extensively rinsed after the lipid deposition.

Anyhow, these supplementary lipid structures were directly bleached by the chemical treatment, whereas the membranes remained half fluorescent. No picture of the half-bleached membrane can be shown due to the too weak intensity of the fluorescent light emitted.

### **10.3.FRAP measurements**

The introduction of the free lipids in the membrane using the rapid solvent exchange technique was performed in a 5ml flow cell allowing the vigorous rinsing after deposition. The substrates were kept underwater when transferred to the measurement cell on top of the microscope. The buffer solution in the measurement cell was containing 10mM HEPES and 0,9% NaCl (pH 7,4). The SiO<sub>x</sub> discs were first located on the sample with the differential interference contrast (DIC) mirror unit of the microscope and afterwards observed with the fluorescence mirror unit, having an excitation range between 470 and 495nm and a 510nm long pass filter for the emission. The samples were focused according to the fluorescence image.

FRAP measurement were performed as described in 2.10.

#### *10.3.1. Lipid diffusion in both leaflets*

The fluorescence recovery was first measured on both leaflets of the labeled SSM. As mentioned before, the bilayer spot was bleached at once by the high intensity laser pulse. A typical recovery curve is shown in Figure 10.5.

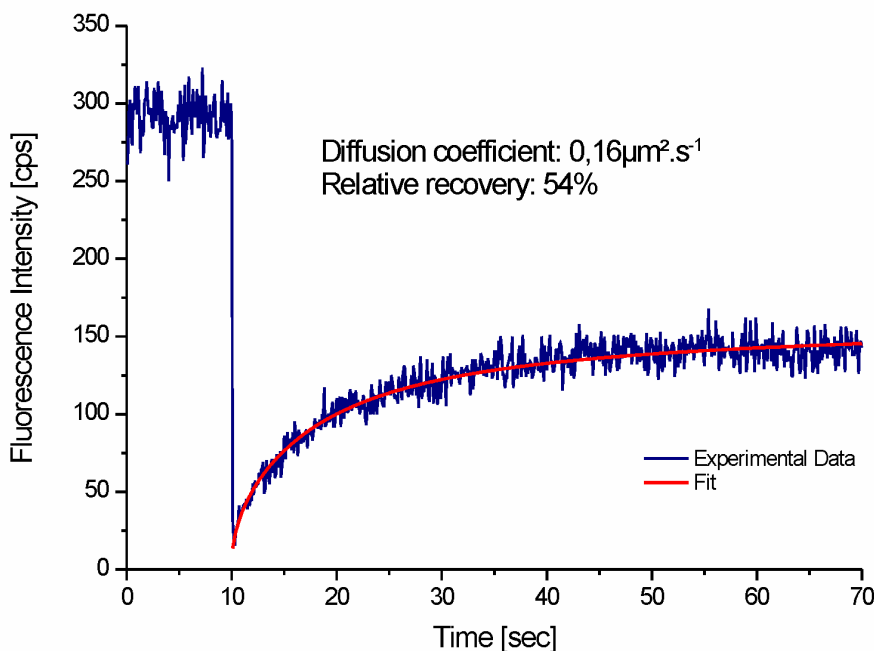


**Figure 10.5: Fluorescence recovery curve of a SSM over a  $\text{SiO}_x$  disc.**

An average over 20 bleached spots on two different samples gave a relative recovery of  $54\% \pm 10\%$ . This result agrees well with the assumptions made, that the fluorophores would distribute equally on both side of the membrane and that only the upper leaflet of the membrane would experience recovery.

Anyhow, the diffusion coefficient over the same 20 measurements is ranging between  $0,5$  and  $7 \cdot 10^{-1} \mu\text{m}^2 \cdot \text{s}^{-1}$  with an average value of  $1,7 \cdot 10^{-1} \mu\text{m}^2 \cdot \text{s}^{-1}$ . The dispersion of this value is too high to make meaningful appreciations about the membrane itself.

But even if a quantitative conclusion cannot be drawn, the diffusion coefficients are still very low with respect to pure SSMs which exhibit mobility of  $3,5$  to  $4 \mu\text{m}^2 \cdot \text{s}^{-1}$  on clean hydrophilic glass.<sup>[56, 114]</sup> Other previous studies already underlined the strong influence of immobile phases in the form of a tethered monolayer on the diffusion of free-moving lipids.<sup>[14, 15]</sup> They showed that the mobility of the lipids was greatly reduced ( $D < 1 \mu\text{m}^2 \cdot \text{s}^{-1}$ ) if not suppressed when the ratio of the anchored lipids to the free lipids increase over a certain threshold. In our case, the assumption can be made that frictions between the hydrophobic chains of DPhyPC and of the polymerized lipids barriers surrounding the measuring spot affected the diffusivity.

### 10.3.2. Lipid diffusion in the bottom leaflet

The distal leaflet of the membranes were bleached according to the method of McIntyre.<sup>[113]</sup>

Briefly, 1ml of a 1,0M Na<sub>2</sub>S<sub>2</sub>O<sub>4</sub> solution in 1,0M Tris (pH 10,0) was added to the 60ml of 10mM HEPES and 0,9% NaCl buffer present in the measuring cell. The mixture was homogenized by a gentle agitation and a pause of 5min for the reduction of the fluorophores to occur was observed before further FRAP measurements.

A typical recovery curve of a bleached system is shown in Figure 10.6.

As expected, the proximal leaflet recovery did not show any recovery. The same result was obtained on all the spot measured. This demonstrated the possibility to create membrane corrals; the lipids in the inner leaflet being confined within the polymerized regions.

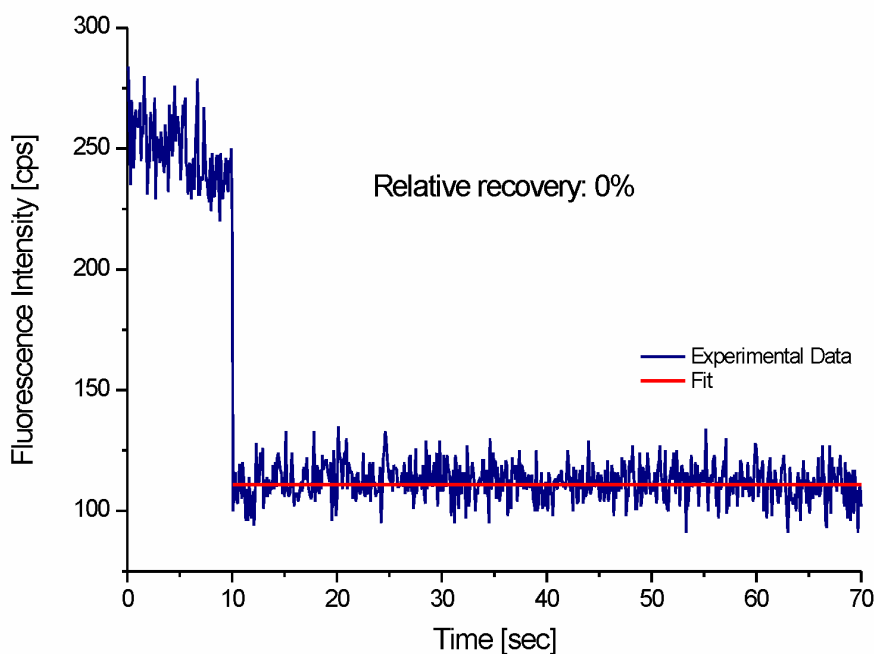


**Figure 10.6: Fluorescence recovery curve of the proximal leaflet after chemical bleaching.**

## 11. Conclusions and outlook

Solid supported membranes have been established as a valuable model membrane system to investigate phenomena occurring at the cell interface.<sup>[8, 11]</sup> Due to their outstanding stability and electrical sealing properties, tethered bilayer lipid membranes (tBLMs) are especially suited for the study of ion channel proteins embedded in the membranes.<sup>[21, 22, 115]</sup> In principle, a tBLM consists of a lipid bilayer, with the inner leaflet covalently attached to a solid support via a spacer group. Such architectures have decisive advantages that can make them useful for biosensing applications, where membrane proteins are used as actual sensing units.<sup>[13, 65]</sup> For such applications, structured membranes, obtained by polymerization of the leaflets, could be very effective in confining incorporated proteins in defined domains or corrals.

So far, polymerizable phospholipids have mainly been used to stabilize liposomes, for example in the pioneering work performed by Ringsdorf et al.,<sup>[116]</sup> Regen et al.,<sup>[27]</sup> Chapman et al.<sup>[26]</sup> and O'Brien et al.<sup>[30]</sup> More recently, the selective lithographic patterning of phospholipids containing diacetylene groups in solid supported membranes has been demonstrated.<sup>[33, 117]</sup> This approach allows the creation of membrane arrays without introducing external barriers on the substrate.<sup>[35, 38]</sup> We combined the functionality and stability of a tBLM with the possibility of patterning the lipid layer using diacetylene lipids, thus opening new possibilities for the creation of biosensing architectures.

Typical biosensor platforms use noble metal electrodes in combination with insulating silicon oxide or silicon nitride matrices. The real challenge for the structuring of substrates addressed to support tBLMs is the requirement of an extreme smoothness to prevent defects. Therefore, the usual way of manufacturing integrated circuits, known from the semiconductor industries could not be used, since the process is creating higher surface roughness and steps, due to the selective evaporation of materials in a bottom-up process. In this study, a reversed approach was developed, depositing first the materials for the patterns of the exposed surface on a ultra smooth substrate, producing a clean, flat and structured support for the tBLMs once the template was removed. This versatile process flow is applicable to a broad range of materials or shape and size of the patterns.

We were aiming at a sensor chip, where a membrane would span structured device surfaces regardless of their chemical nature. Therefore different anchor lipids were synthesized. Two different surface binding groups, a dithiolane group for gold surfaces and a triethoxysilane group for oxide or nitride substrates, allow the selective functionalization of the respective surfaces. The elongated *all-trans* configuration of the ethylene oxide chains provide a maximum decoupling from the substrate, while still permitting the formation of highly ordered monolayers.<sup>[118]</sup> A prerequisite for the solid state polymerization of diacetylenes on a solid substrate is the highly ordered packing of the monomers.<sup>[43]</sup> Anchor lipids with different hydrophobic chains were synthesized and the effect of the alkyl chain length on the ability of the films to form a liquid crystalline (LC) phase was studied.

Monomolecular layers were investigated using Langmuir film techniques by spreading the lipid monomers at the air-water interface and compressing the resulting film to the point of collapse. The measured isotherms showed a clear solid state phase upon compression for two of the lipids, namely HC<sub>2</sub>(EO)<sub>4</sub>LA and HC<sub>2</sub>(EO)<sub>4</sub>TES, indicating the packing of the diacetylenic chains in a LC state. Long fatty acid chains with diacetylenes groups were forming a light sensitive crystal lattice, allowing polymerization at room temperature. Shorter chains resulted in a shift of the phase transition temperature of the monolayer below room temperature and thus made the film insensitive to UV light. Furthermore, compared with the dithiolane group of the lipoic acid, the bulky triethoxysilane group led to a shift towards higher areas at the same surface pressure and did not allow the creation of films as well packed as for the lipoic acid analog.

Diacetylenes can be polymerized in a topochemical 1,4-addition within the crystal lattice by UV-light irradiation in a nitrogen atmosphere.<sup>[43]</sup> The exclusion of oxygen is necessary to prevent the formation of ozone under UV leading to the destruction of the backbone of the polymer. The formation of a highly conjugated polymeric backbone between the anchored lipids induces strong absorptions in the visible spectrum and can be followed by UV-Vis spectroscopy. The resulting fluorescence also occurs in the visible spectrum and can be used by fluorescence microscopy to visualize the polymerized areas. Since the monomers do not absorb in the visible range, the polymerization reaction was directly followed as an increase in the absorbance. Monolayers of the lipids were transferred onto a quartz slide and UV-Vis spectra were recorded as a function of the polymerization time. The characteristic peaks of polydiacetylene films at 490 nm and 529 nm appeared with

increasing UV irradiation time.<sup>[26]</sup> The absorption at 529 nm increased until saturation was reached after 60-70 min of irradiation showing the end of the reaction. Further, the monolayers were selectively polymerized using a mask, hence creating different structures in the films, and these structures were observed by fluorescence microscopy.

The newly synthesized tBLM system was then evaluated on its ability to functionally incorporate proteins. This was done through EIS measurement with the test protein valinomycin. The creation of bilayers was followed by the resistance increase over the membrane, parallel to the decrease in capacitance. The introduction of the ionophore in the system produced the expected drop in resistance, due to the transfer of potassium ions from one side of the membrane to the other, inducing an electrical shortcut. The inhibition of this transport was achieved by replacing the potassium to sodium ions, directly reflected by the recovery of the membrane resistance.

Finally, the engineered substrates were functionalized with a hybrid membrane of anchored and free diffusing lipids. To demonstrate the possibility to use polymerized monolayer as diffusion barriers, FRAP measurements were performed on fluorescently labeled phospholipid SSMs, corralled by a polymerized tBLM structure. As expected, the SSM exhibited only 50% of fluorescence recovery, indicating that only the distal leaflet was mobile. Further measurements on the proximal leaflet only, confirmed this assumption by showing no recovery at all, the fluorescent membrane being of the same size as the laser spot.

The photolithographic polymerization of tBLMs presented here makes it possible to create patterns with resolutions theoretically only limited by the diffraction of light and the propagation of the polymerization within the crystal domain. This design of hybrid membrane arrays, which suppresses the undefined edge effects arising from the contact of a membrane with a solid barrier, offers the unique chance to enclose proteins over sensing fields without resorting to foreign material.

Future studies based on this approach could be developed and characterize the applicability of the hybrid system further. First, the mobility of the lipids within the corral could be probed in size dependence of the SSMs. Intuition tells us that with increasing size, the mobility of the phospholipids within the membrane should increase until it reaches the one

observed in pure SSMs on hydrophilic substrates. The modification of the SiO<sub>x</sub> pads on the substrates with small hydrophilic silane could be probed in order to bring a sort of cushion beneath the free diffusing membrane. Furthermore, development of the substrates could also be envisioned, by using ordered colloidal monolayers, leading to the construction of nanometer scale honeycomb structures and therefore nanometer scale membranes.

Finally, through the incorporation of fluorescence proteins, the study of single molecules diffusing in a hindered environment, simulating a biological membrane, can be achieved and probe the existing diffusion theories.<sup>[82, 119-122]</sup>

## 12. Appendix

### 12.1. $^1\text{H}$ -NMR and FD-Mass spectra of the synthesized anchor lipids:

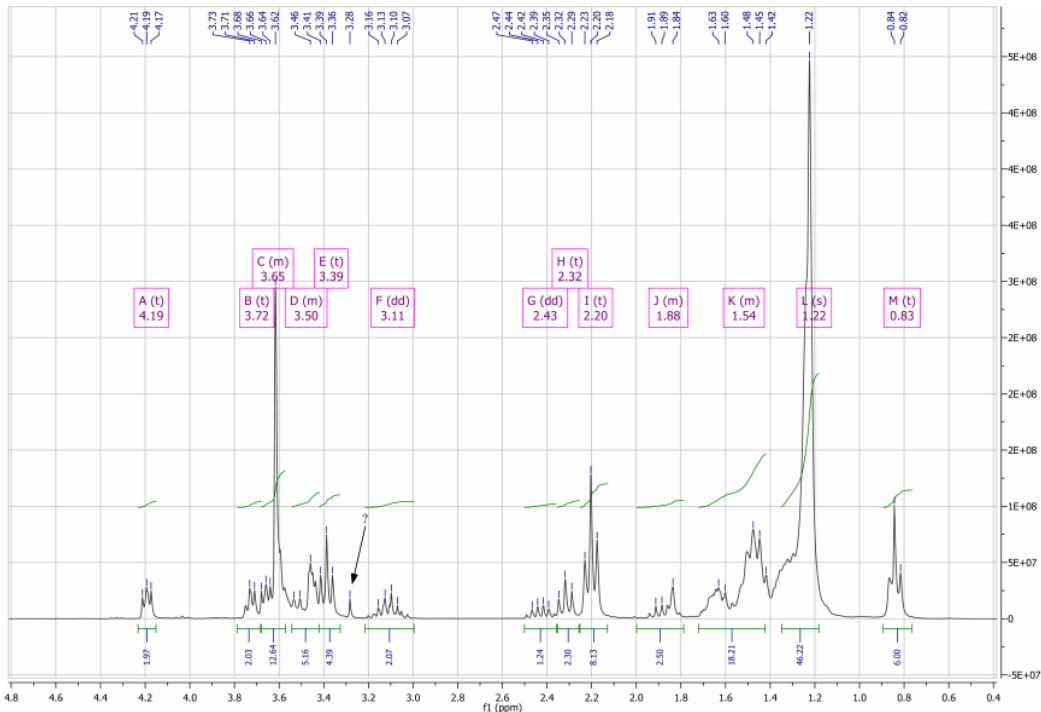


Figure 12.1:  $^1\text{H}$ -NMR spectra of TD2(EO)<sub>4</sub>LA (8)

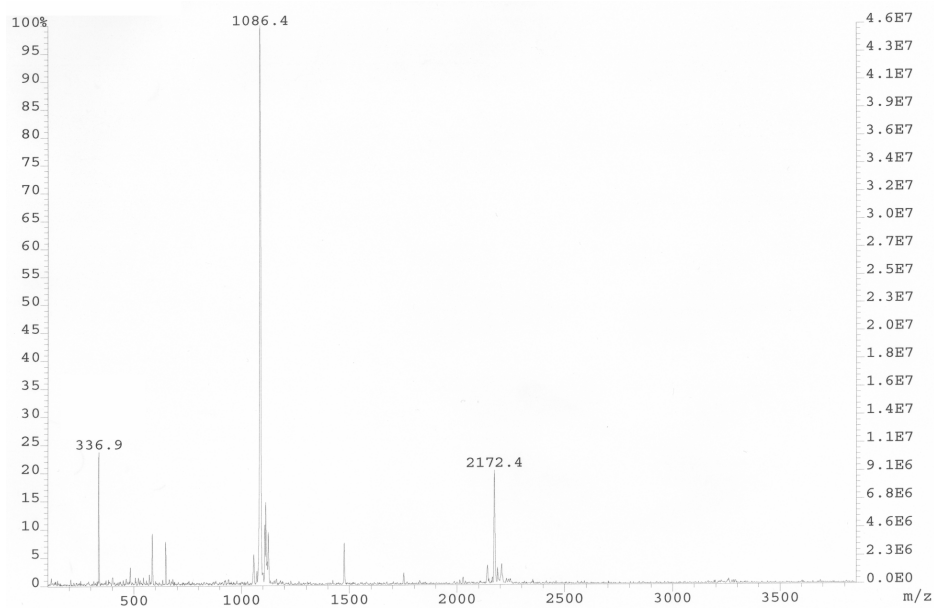
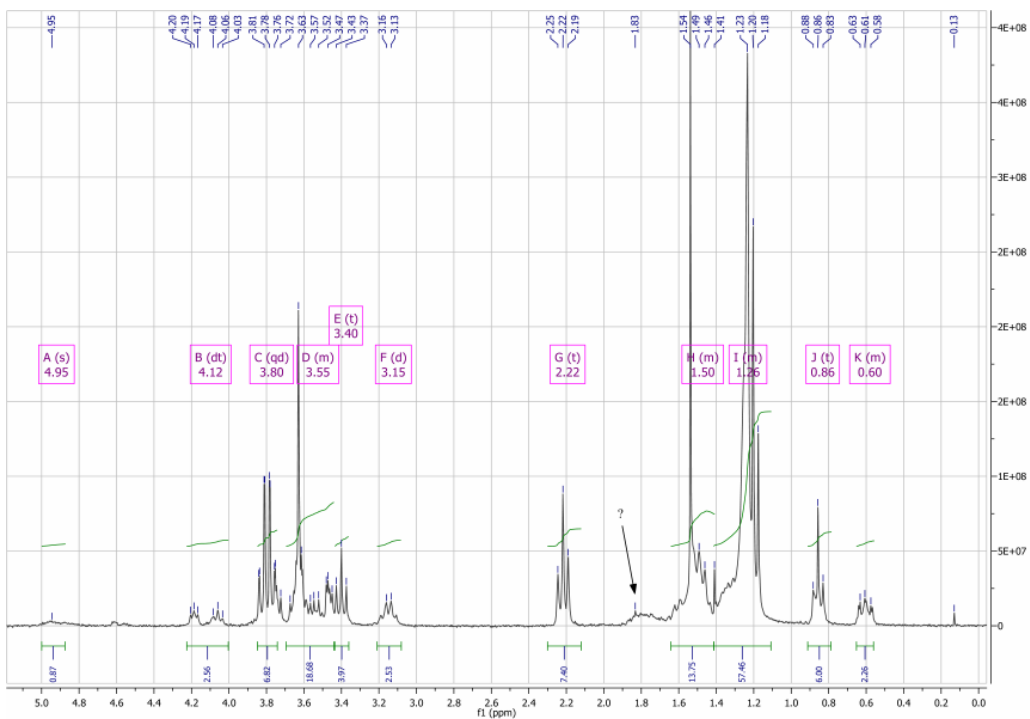
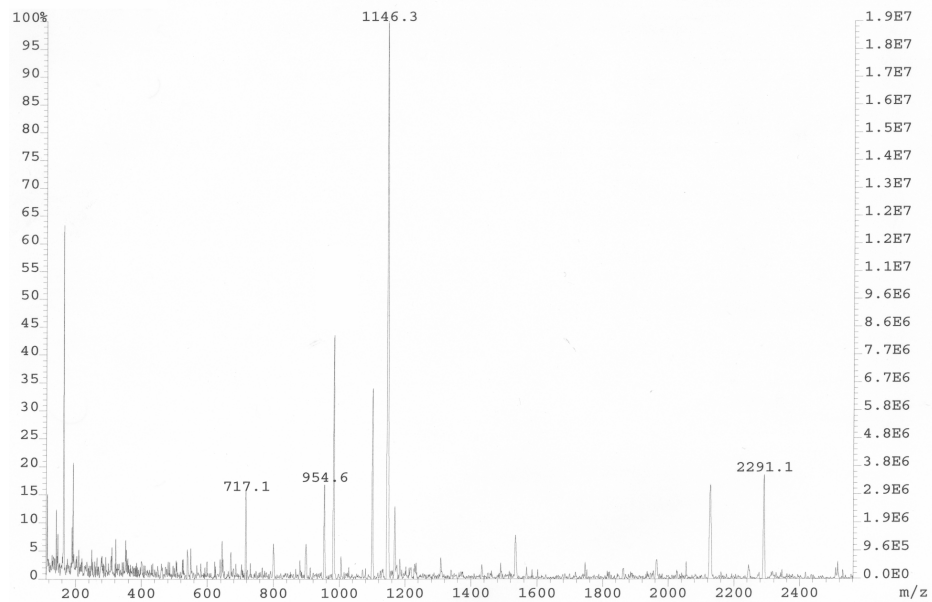


Figure 12.2: FD-mass spectra of TD2(EO)<sub>4</sub>LA (8)



**Figure 12.3:**  $^1\text{H}$ -NMR spectra of TD2(EO)<sub>4</sub>TES (9)



**Figure 12.4:** FD-mass spectra of TD2(EO)<sub>4</sub>TES (9)

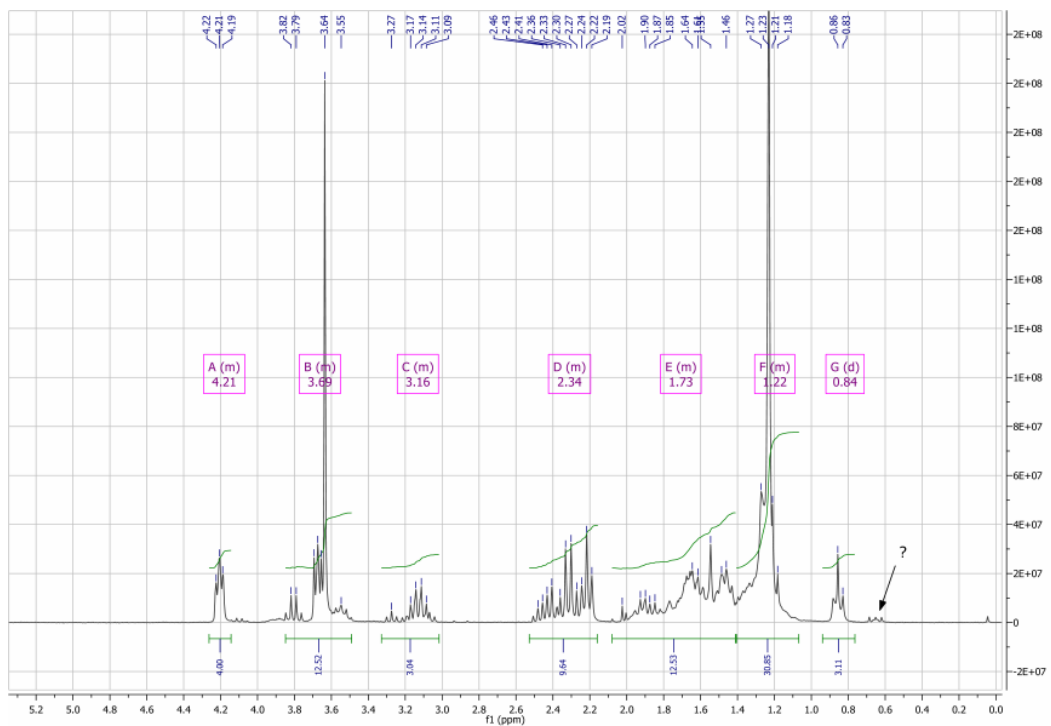


**Figure 12.5:**  $^1\text{H}$ -NMR spectra of  $\text{HC1}(\text{EO})_4\text{LA}$  (21)

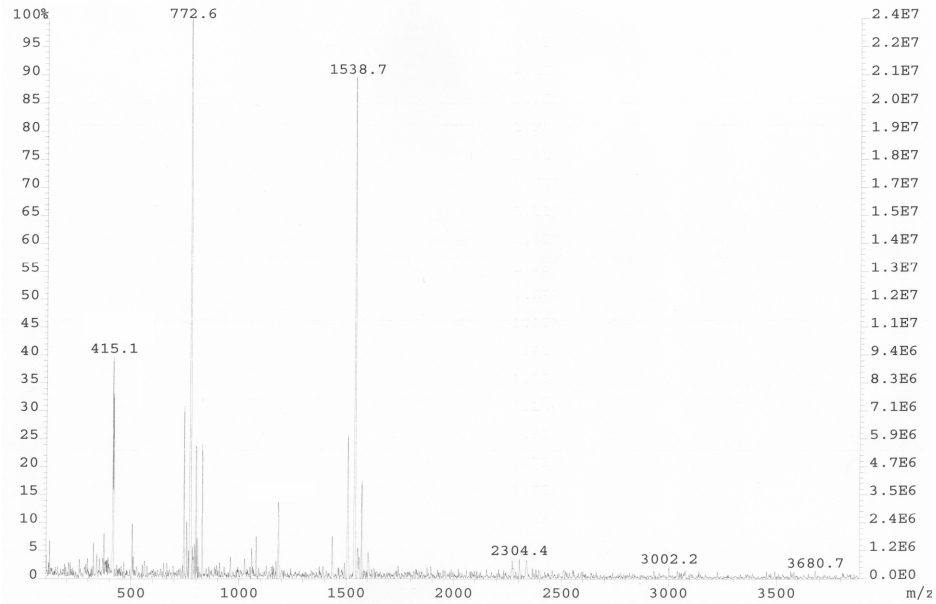


**Figure 12.6:** FD-mass spectra of  $\text{HC1}(\text{EO})_4\text{LA}$  (21)

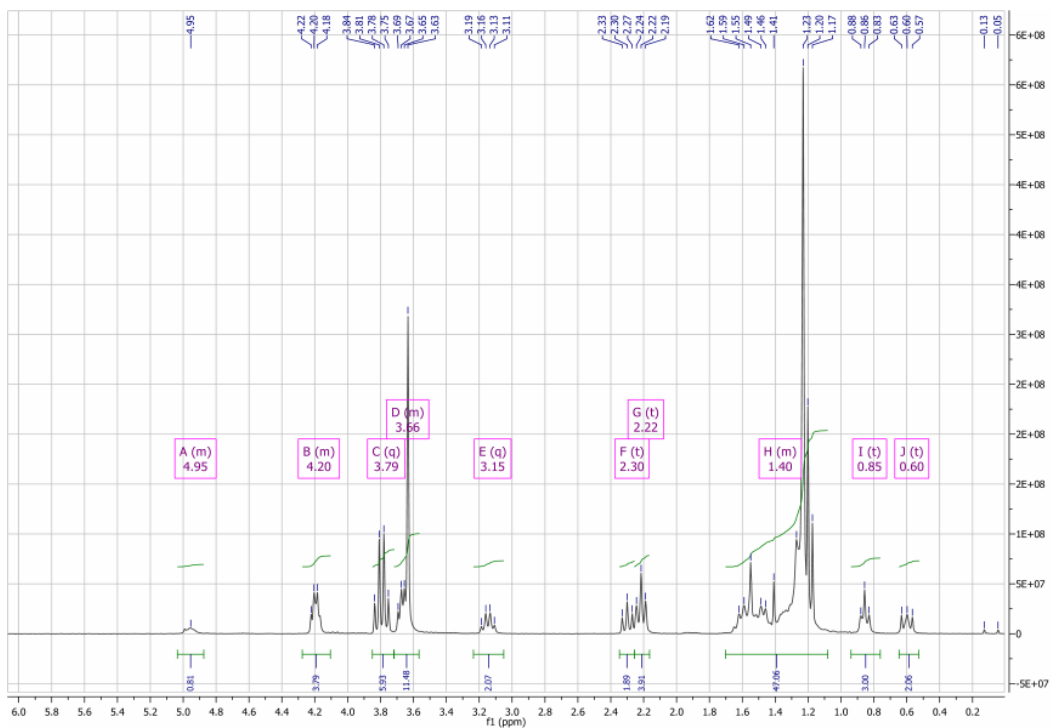


**Figure 12.7:**  $^1\text{H}$ -NMR spectra of  $\text{HC}_1(\text{EO})_4\text{TES}$  (22)

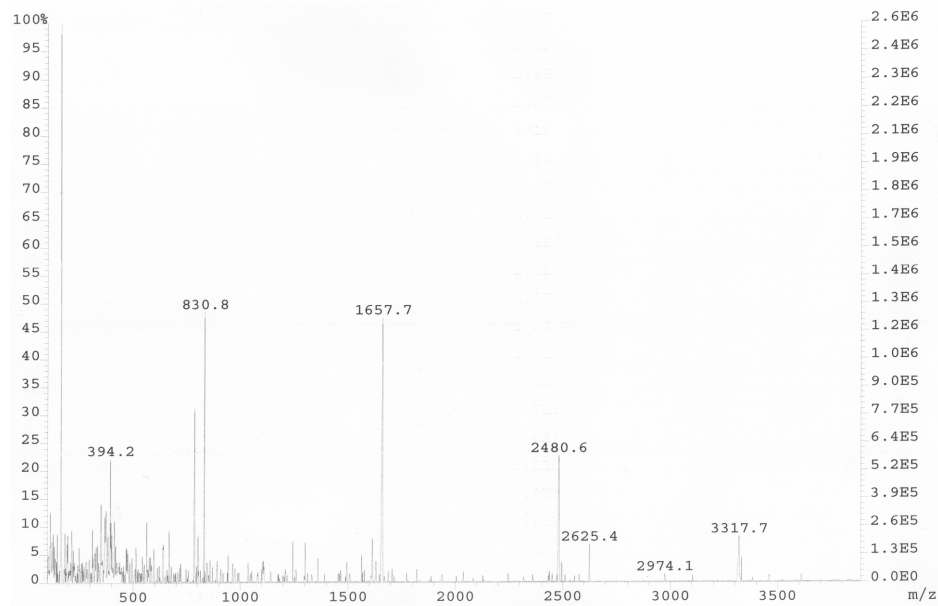


**Figure 12.8:** FD-mass spectra of  $\text{HC}_1(\text{EO})_4\text{TES}$  (22)

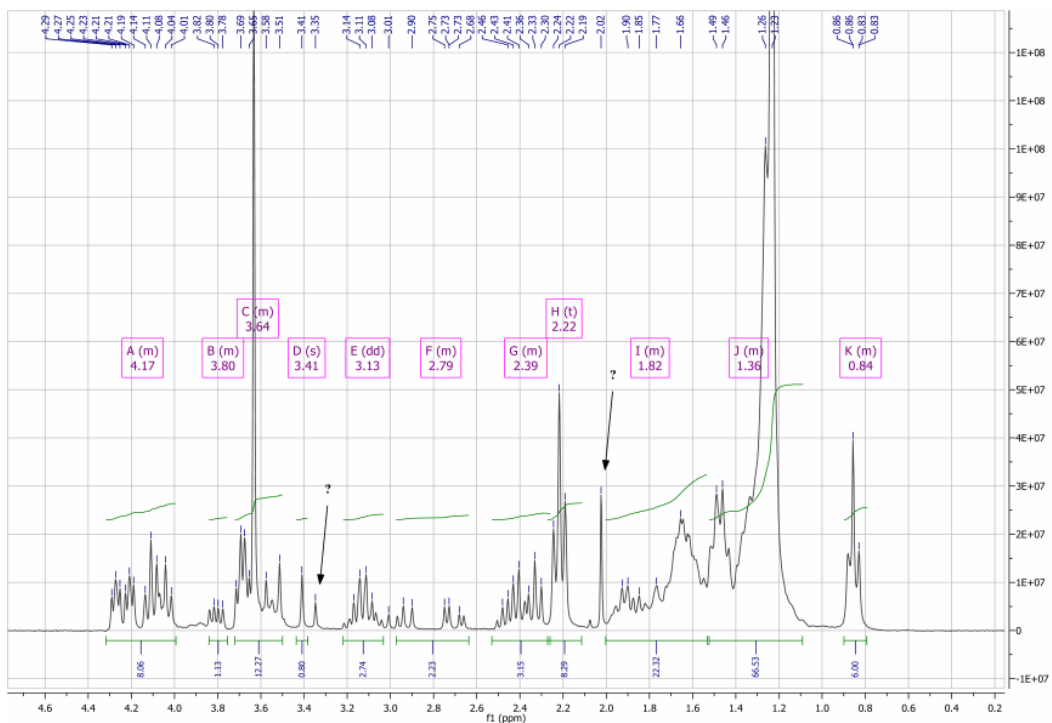


**Figure 12.9:**  $^1\text{H}$ -NMR spectra of  $\text{HC}_2(\text{EO})_4\text{LA}$  (17)

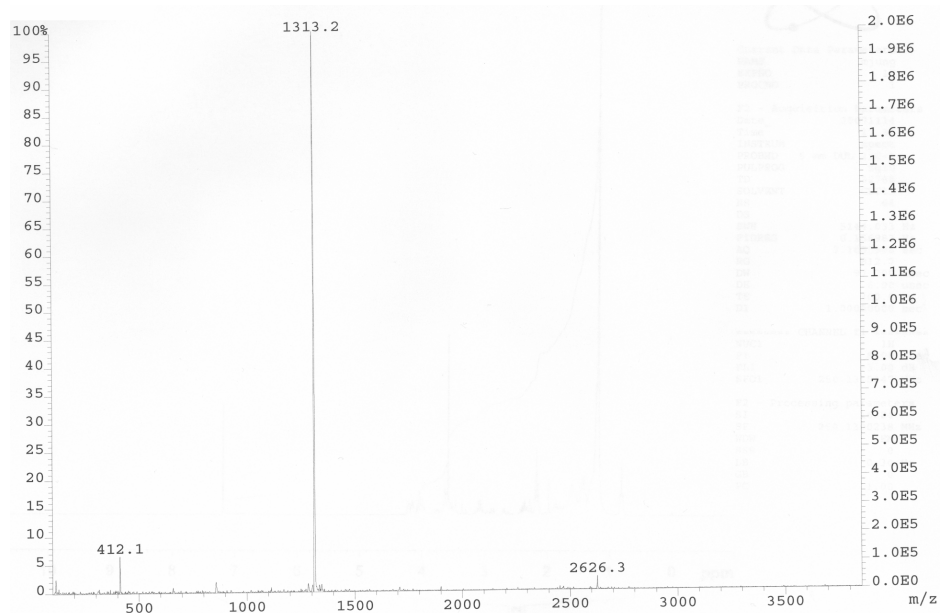


**Figure 12.10:** FD-mass spectra of  $\text{HC}_2(\text{EO})_4\text{LA}$  (17)

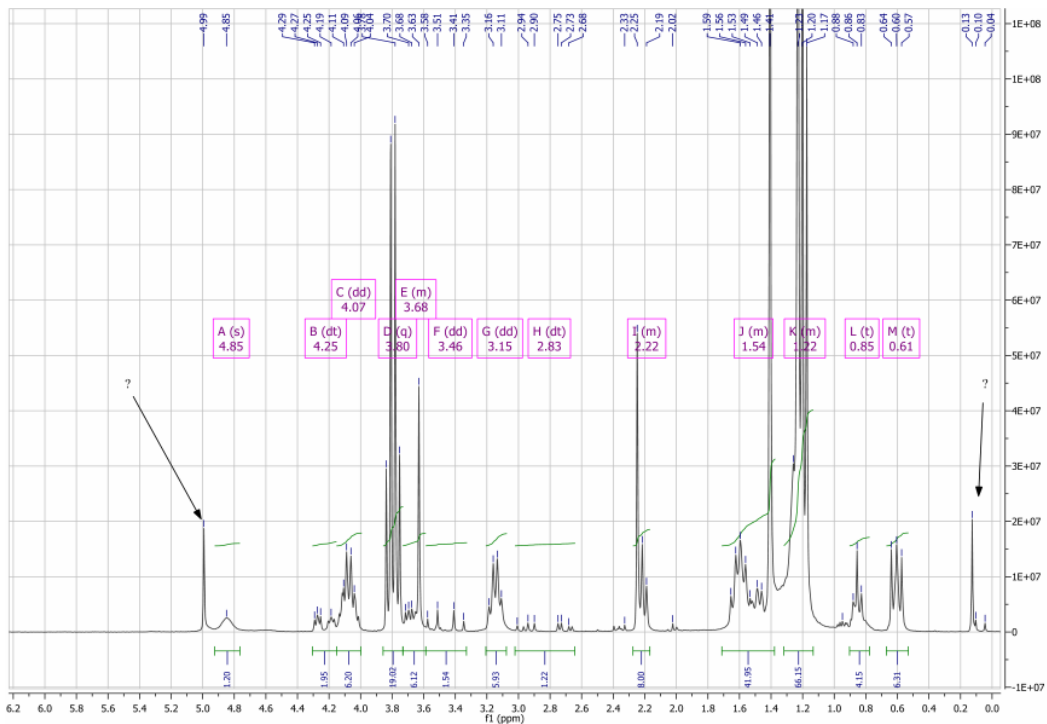


**Figure 12.11:**  $^1\text{H}$ -NMR spectra of  $\text{HC}_2(\text{EO})_4\text{TES}$  (18)

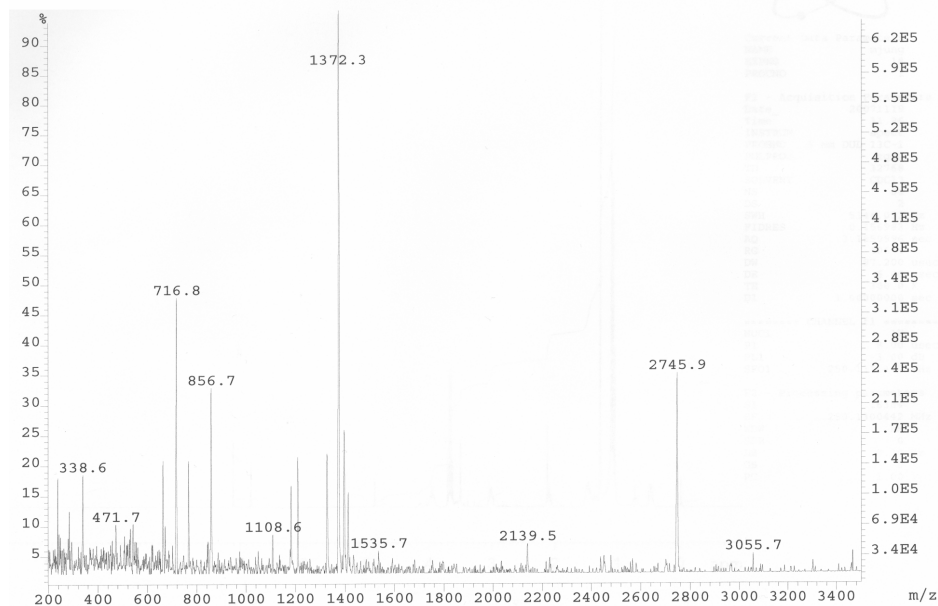


**Figure 12.12:** FD-mass spectra of  $\text{HC}_2(\text{EO})_4\text{TES}$  (18)

## 13. Literature

- [1] S. J. Singer, G. L. Nicolson, *Science* **1972**, *175*, 720.
- [2] L. D. Frye, M. Edidin, *Journal of Cell Science* **1970**, *7*, 319.
- [3] B. Alberts, A. Johnson, J. Lewis, M. Raff, K. Roberts, P. Walter, *Molecular biology of the cell*, Garland Science, **2002**.
- [4] C. Bieri, O. P. Ernst, S. Heyse, K. P. Hofmann, H. Vogel, *Nature Biotechnology* **1999**, *17*, 1105.
- [5] C. Danelon, J. B. Perez, C. Santschi, J. Brugger, H. Vogel, *Langmuir* **2006**, *22*, 22.
- [6] D. F. Evans, *Langmuir* **1988**, *4*, 3.
- [7] C. Tanford, *Science* **1978**, *200*, 1012.
- [8] E. Sackmann, *Science* **1996**, *271*, 43.
- [9] E. Reimhult, F. Hook, B. Kasemo, *Physical Review E* **2002**, *66*.
- [10] E. Reimhult, F. Hook, B. Kasemo, *Langmuir* **2003**, *19*, 1681.
- [11] L. K. Tamm, H. M. McConnell, *Biophysical Journal* **1985**, *47*, 105.
- [12] J. Majewski, J. Y. Wong, C. K. Park, M. Seitz, J. N. Israelachvili, G. S. Smith, *Biophysical Journal* **1998**, *75*, 2363.
- [13] M. Tanaka, E. Sackmann, *Nature* **2005**, *437*, 656.
- [14] M. A. Deverall, E. Gindl, E. K. Sinner, H. Besir, J. Ruehe, M. J. Saxton, C. A. Naumann, *Biophysical Journal* **2005**, *88*, 1875.
- [15] M. L. Wagner, L. K. Tamm, *Biophysical Journal* **2000**, *79*, 1400.
- [16] J. Drexler, C. Steinem, *Journal of Physical Chemistry B* **2003**, *107*, 11245.
- [17] C. Hennesthal, J. Drexler, C. Steinem, *Chemphyschem* **2002**, *3*, 885.
- [18] R. Naumann, S. M. Schiller, F. Giess, B. Grohe, K. B. Hartman, I. Karcher, I. Koper, J. Lubben, K. Vasilev, W. Knoll, *Langmuir* **2003**, *19*, 5435.
- [19] O. Purrucker, S. Gonnenwein, A. Fortig, R. Jordan, M. Rusp, M. Barmann, L. Moroder, E. Sackmann, M. Tanaka, *Soft Matter* **2007**, *3*, 333.
- [20] S. M. Schiller, R. Naumann, K. Lovejoy, H. Kunz, W. Knoll, *Angewandte Chemie-International Edition* **2003**, *42*, 208.
- [21] I. Köper, *Molecular Biosystems* **2007**, *3*, 651.
- [22] I. Vockenroth, C. Ohm, J. W. F. Robertson, D. J. M. Gillary, M. Lösche, I. Köper, *Biointerfaces* **2008**, Accepted.
- [23] I. K. Vockenroth, P. P. Atanasova, A. T. A. Jenkins, I. Koper, *Langmuir* **2008**, *24*, 496.
- [24] R. Elbert, A. Laschewsky, H. Ringsdorf, *Abstracts of Papers of the American Chemical Society* **1985**, *189*, 139.
- [25] H. H. Hub, B. Hupfer, H. Koch, H. Ringsdorf, *Angewandte Chemie-International Edition in English* **1980**, *19*, 938.
- [26] L. F. Chi, M. Anders, H. Fuchs, R. R. Johnston, H. Ringsdorf, *Science* **1993**, *259*, 213.
- [27] S. L. Regen, B. Czech, A. Singh, *Journal of the American Chemical Society* **1980**, *102*, 6638.
- [28] H. Ringsdorf, B. Schlarb, J. Venzmer, *Angewandte Chemie-International Edition in English* **1988**, *27*, 113.
- [29] S. M. Daly, L. A. Heffernan, W. R. Barger, D. K. Shenoy, *Langmuir* **2006**, *22*, 1215.
- [30] D. F. Obrien, T. H. Whitesides, R. T. Klingbiel, *Journal of Polymer Science Part C-Polymer Letters* **1981**, *19*, 95.

- [31] D. Day, H. Ringsdorf, *Journal of Polymer Science Part C-Polymer Letters* **1978**, *16*, 205.
- [32] C. M. Gupta, C. E. Costello, H. G. Khorana, *Proceedings of the National Academy of Sciences of the United States of America* **1979**, *76*, 3139.
- [33] K. Morigaki, T. Baumgart, A. Offenhausser, W. Knoll, *Angewandte Chemie-International Edition* **2001**, *40*, 172.
- [34] K. Morigaki, T. Baumgart, U. Jonas, A. Offenhausser, W. Knoll, *Langmuir* **2002**, *18*, 4082.
- [35] J. T. Groves, L. K. Mahal, C. R. Bertozzi, *Langmuir* **2001**, *17*, 5129.
- [36] J. T. Groves, N. Ulman, S. G. Boxer, *Science* **1997**, *275*, 651.
- [37] J. S. Hovis, S. G. Boxer, *Langmuir* **2000**, *16*, 894.
- [38] J. S. Hovis, S. G. Boxer, *Langmuir* **2001**, *17*, 3400.
- [39] M. H. Cohen, D. Turnbull, *Journal of Chemical Physics* **1959**, *31*, 1164.
- [40] V. Ramamurthy, *Tetrahedron* **1986**, *42*, 5753.
- [41] V. Ramamurthy, K. Venkatesan, *Chemical Reviews* **1987**, *87*, 433.
- [42] C. N. Riiber, *Berichte Der Deutschen Chemischen Gesellschaft* **1902**, *35*, 2908.
- [43] G. Wegner, *Chimia* **1974**, *28*, 475.
- [44] A. Baeyer, *Berichte Der Deutschen Chemischen Gesellschaft* **1885**, *18*, 674.
- [45] W. Knoll, F. Yu, T. Neumann, S. Schiller, R. Naumann, *Physical Chemistry Chemical Physics* **2003**, *5*, 5169.
- [46] G. L. Gaines, *Insoluble monolayers at the liquid-gas interfaces*, Interscience, New York, **1966**.
- [47] H. Möhwald, *Phospholipid Monolayers*, Vol. 1, **1995**.
- [48] H. E. Ries, H. Swift, *Langmuir* **1987**, *3*, 853.
- [49] K. B. Blodgett, *Journal of the American Chemical Society* **1935**, *57*, 1007.
- [50] K. B. Blodgett, I. Langmuir, *Physical Review* **1937**, *51*, 0964.
- [51] M. Hegner, P. Wagner, G. Semenza, *Surface Science* **1993**, *291*, 39.
- [52] C. D. Bain, E. B. Troughton, Y. T. Tao, J. Evall, G. M. Whitesides, R. G. Nuzzo, *Journal of the American Chemical Society* **1989**, *111*, 321.
- [53] R. G. Nuzzo, D. L. Allara, *Journal of the American Chemical Society* **1983**, *105*, 4481.
- [54] J. Sagiv, *Journal of the American Chemical Society* **1980**, *102*, 92.
- [55] D. L. Allara, R. G. Nuzzo, *Langmuir* **1985**, *1*, 45.
- [56] E. Kalb, S. Frey, L. K. Tamm, *Biochimica Et Biophysica Acta* **1992**, *1103*, 307.
- [57] C. Miller, P. Cuendet, M. Gratzel, *Journal of Electroanalytical Chemistry* **1990**, *278*, 175.
- [58] B. Raguse, V. Braach-Maksvytis, B. A. Cornell, L. G. King, P. D. J. Osman, R. J. Pace, L. Wieczorek, *Langmuir* **1998**, *14*, 648.
- [59] T. Young, *Miscellaneous works*, Vol. 1, G. Peacock Ed., Murray, London, **1855**.
- [60] F. E. Bartell, L. S. Bartell, *J. Am. Chem. Soc.* **1934**, *56*, 2205.
- [61] T. Smith, *Journal of Colloid and Interface Science* **1980**, *75*, 51.
- [62] A. Beer, *Annalen der Physik und Chemie* **1852**, *86*, 78.
- [63] D. Day, H. H. Hub, H. Ringsdorf, *Israel Journal of Chemistry* **1979**, *18*, 325.
- [64] S. Okada, S. Peng, W. Spevak, D. Charych, *Accounts of Chemical Research* **1998**, *31*, 229.
- [65] B. A. Cornell, V. L. B. BraachMaksvytis, L. G. King, P. D. J. Osman, B. Raguse, L. Wieczorek, R. J. Pace, *Nature* **1997**, *387*, 580.
- [66] M. Stelzle, G. Weissmuller, E. Sackmann, *Journal of Physical Chemistry* **1993**, *97*, 2974.
- [67] J. R. Macdonald, *Impedance Spectroscopy*, John Wiley & Sons, New York, **1987**.

- [68] B. Menges, S. Mittler, in *Frontiers in Nanophotonics*, Springer Science, New York, **2007**, pp. 19.
- [69] O. Prucker, S. Christian, H. Bock, J. Ruhe, C. W. Frank, W. Knoll, *Macromolecular Chemistry and Physics* **1998**, *199*, 1435.
- [70] D. Axelrod, D. E. Koppel, J. Schlessinger, E. Elson, W. W. Webb, *Biophysical Journal* **1976**, *16*, 1055.
- [71] T. M. Jovin, W. L. C. Vaz, *Methods in Enzymology* **1989**, *172*, 471.
- [72] A. Nayeem, S. B. Ranavare, V. S. S. Sastry, J. H. Freed, *Journal of Chemical Physics* **1989**, *91*, 6887.
- [73] H. J. Galla, W. Hartmann, U. Theilen, E. Sackmann, *Journal of Membrane Biology* **1979**, *48*, 215.
- [74] W. Pfeiffer, G. Schlossbauer, W. Knoll, B. Farago, A. Steyer, E. Sackmann, *Journal De Physique* **1988**, *49*, 1077.
- [75] H. Geerts, M. Debrabander, R. Nuydens, S. Geuens, M. Moeremans, J. Demey, P. Hollenbeck, *Biophysical Journal* **1987**, *52*, 775.
- [76] M. P. Sheetz, S. Turney, H. Qian, E. L. Elson, *Nature* **1989**, *340*, 284.
- [77] A. L. Kuo, C. G. Wade, *Biochemistry* **1979**, *18*, 2300.
- [78] G. Lindblom, L. B. A. Johansson, G. Arvidson, *Biochemistry* **1981**, *20*, 2204.
- [79] P. Devaux, Mcconnel.Hm, *Journal of the American Chemical Society* **1972**, *94*, 4475.
- [80] E. Evans, E. Sackmann, *Journal of Fluid Mechanics* **1988**, *194*, 553.
- [81] B. D. Hughes, B. A. Pailthorpe, L. R. White, *Journal of Fluid Mechanics* **1981**, *110*, 349.
- [82] P. F. F. Almeida, W. L. C. Vaz, T. E. Thompson, *Biochemistry* **1992**, *31*, 6739.
- [83] I. K. Vockenroth, D. Fine, A. Dodobalapur, A. T. A. Jenkins, I. Koper, *Electrochemistry Communications* **2008**, *10*, 323.
- [84] U. Jonas, C. Krüger, *Journal of Supramolecular Chemistry* **2002**, *2*, 255.
- [85] Y. S. Lee, D. F. Obrien, *Chemistry and Physics of Lipids* **1992**, *61*, 209.
- [86] W. F. Berkowitz, D. Pan, R. Bittman, *Tetrahedron Letters* **1993**, *34*, 4297.
- [87] B. Neises, W. Steglich, *Angewandte Chemie-International Edition in English* **1978**, *17*, 522.
- [88] Y. J. Cui, L. J. Chen, G. D. Qian, M. Q. Wang, *Dyes and Pigments* **2006**, *70*, 232.
- [89] T. W. Baughman, J. C. Sworen, K. B. Wagener, *Tetrahedron* **2004**, *60*, 10943.
- [90] K. F. Bernady, M. B. Floyd, J. F. Poletto, M. J. Weiss, *J. Org. Chem.* **1979**, *44*, 1438.
- [91] J. M. Klunder, S. Y. Ko, K. B. Sharpless, *Journal of Organic Chemistry* **1986**, *51*, 3710.
- [92] K. B. Sharpless, S. S. Woodard, M. G. Finn, *Pure and Applied Chemistry* **1983**, *55*, 1823.
- [93] I. D. Williams, S. F. Pedersen, K. B. Sharpless, S. J. Lippard, *J. Am. Chem. Soc.* **1984**, *106*, 6430.
- [94] W. Müller, Johannes Gutenberg Universität (Mainz), **1993**.
- [95] H. Bader, Johannes Gutenberg University (Mainz), **1985**.
- [96] T. G. Burke, A. S. Rudolph, R. R. Price, J. P. Sheridan, A. W. Dalziel, A. Singh, P. E. Schoen, *Chemistry and Physics of Lipids* **1988**, *48*, 215.
- [97] A. Singh, T. G. Burke, J. M. Calvert, J. H. Georger, B. Herendeen, R. R. Price, P. E. Schoen, P. Yager, *Chemistry and Physics of Lipids* **1988**, *47*, 135.
- [98] A. Singh, M. Markowitz, L. I. Tsao, *Abstracts of Papers of the American Chemical Society* **1992**, *203*, 197.
- [99] A. R. Gallagher, H. Hibbert, *Journal of the American Chemical Society* **1936**, *58*, 813.

- [100] B. Hupfer, H. Ringsdorf, *Chemistry and Physics of Lipids* **1983**, *33*, 263.
- [101] S. W. Hui, H. Yu, Z. C. Xu, R. Bittman, *Langmuir* **1992**, *8*, 2724.
- [102] F. Gaboriaud, R. Volinsky, A. Berman, R. Jelinek, *Journal of Colloid and Interface Science* **2005**, *287*, 191.
- [103] K. Morigaki, K. Kiyosue, T. Taguchi, *Langmuir* **2004**, *20*, 7729.
- [104] K. Morigaki, H. Schonherr, C. W. Frank, W. Knoll, *Langmuir* **2003**, *19*, 6994.
- [105] T. Kajiyama, Y. Oishi, M. Uchida, Y. Tanimoto, H. Kozuru, *Langmuir* **1992**, *8*, 1563.
- [106] T. Kajiyama, Y. Oishi, in *New developments in construction and functions of organic thin films*, Elsevier Science, **1996**, pp. 1.
- [107] B. A. Cornell, G. Krishna, P. D. Osman, R. D. Pace, L. Wieczorek, *Biochemical Society Transactions* **2001**, *29*, 613.
- [108] P. Lauger, *Science* **1972**, *178*, 24.
- [109] G. Krishna, J. Schulte, B. A. Cornell, R. Pace, L. Wieczorek, P. D. Osman, *Langmuir* **2001**, *17*, 4858.
- [110] G. Krishna, J. Schulte, B. A. Cornell, R. J. Pace, P. D. Osman, *Langmuir* **2003**, *19*, 2294.
- [111] R. D. Kornberg, McConnel.Hm, *Biochemistry* **1971**, *10*, 1111.
- [112] B. Sanii, A. N. Parikh, *Soft Matter* **2007**, *3*, 974.
- [113] J. C. McIntyre, R. G. Sleight, *Biochemistry* **1991**, *30*, 11819.
- [114] L. K. Tamm, *Biochemistry* **1988**, *27*, 1450.
- [115] S. M. Schiller, R. Naumann, K. Lovejoy, H. Kunz, W. Knoll, in *Angewandte Chemie, Vol. 115*, **2003**, pp. 219.
- [116] H.-H. Hub, B. Hupfer, H. Koch, H. Ringsdorf, in *Angewandte Chemie, Vol. 92, 1980*, pp. 962.
- [117] K. Morigaki, T. Baumgart, A. Offenhäusser, W. Knoll, in *Angewandte Chemie, Vol. 113, 2001*, pp. 184.
- [118] D. J. Vanderah, C. P. Pham, S. K. Springer, V. Silin, C. W. Meuse, *Langmuir* **2000**, *16*, 6527.
- [119] R. Peters, R. J. Cherry, *Proceedings of the National Academy of Sciences of the United States of America-Biological Sciences* **1982**, *79*, 4317.
- [120] M. J. Saxton, *Biophysical Journal* **1982**, *39*, 165.
- [121] M. J. Saxton, *Biophysical Journal* **1986**, *49*, A311.
- [122] M. J. Saxton, *Biophysical Journal* **2001**, *81*, 2226.

## **14. Publications**

N. Vogel, M. Jung, M. Retsch, U. Jonas, W. Knoll, I. Köper, Laterally patterned ultra flat surfaces, *in preparation*.

M. Jung, N. Vogel, I. Köper, Creation of a solid supported membrane archipelago with polymerizable anchor lipids, *in preparation*.

## **15. Curriculum Vitae**